Use this as Library Cy

UCRL 16788

cy. 2

University of California
Ernest O. Lawrence Radiation Laboratory

ANALYSIS OF STRANGE-PARTICLE RESONANT STATES FROM $\bar{p}$ INTERACTIONS

TWO-WEEK LOAN COPY

This is a Library Circulating Copy which may be borrowed for two weeks. For a personal retention copy, call Tech. Info. Division, Ext. 5545

Berkeley, California

c.2

DISCLAIMER

This document was prepared as an account of work sponsored by the United States Government. While this document is believed to contain correct information, neither the United States Government nor any agency thereof, nor the Regents of the University of California, nor any of their employees, makes any warranty, express or implied, or assumes any legal responsibility for the accuracy, completeness, or usefulness of any information, apparatus, product, or process disclosed, or represents that its use would not infringe privately owned rights. Reference herein to any specific commercial product, process, or service by its trade name, trademark, manufacturer, or otherwise, does not necessarily constitute or imply its endorsement, recommendation, or favoring by the United States Government or any agency thereof, or the Regents of the University of California. The views and opinions of authors expressed herein do not necessarily state or reflect those of the United States Government or any agency thereof or the Regents of the University of California.

UCRL-16788

UNIVERSITY OF CALIFORNIA
Lawrence Radiation Laboratory
Berkeley, California

AEC Contract No. W-7405-eng-48

ANALYSIS OF STRANGE-PARTICLE RESONANT STATES FROM $\pi^- p$ INTERACTIONS

Lyndon Mauriece Hardy
(Ph. D. Thesis)

July 11, 1966

Printed in USA. Price $1.00. Available from the Clearinghouse for Federal Scientific and Technical Information, National Bureau of Standards, U. S. Department of Commerce, Springfield, Virginia.

ANALYSIS OF STRANGE-PARTICLE RESONANT STATES FROM $\pi^- p$ INTERACTIONS

Contents

Abstract v

I. Introduction 1

II. Experimental Procedure

A. Beam 2

B. Scanning and Measuring 2

C. Fitting of Events 2

D. Separation of Hypotheses 6

1. Four-Constraint Fits 12

2. Two-Constraint Fits 14

3. One-Constraint Fits 16

4. Zero-Constraint Fits 21

E. Primary Data Reduction 21

III. Cross Sections 23

A. The Cross-Section Scan 23

B. Scanning Corrections 26

C. Measuring Corrections 31

D. Detection Corrections 31

E. Results 33

IV. Properties of Resonant-State Production 39

A. Three-Body Final States

1. $Y_0^*(1405)$ 43

2. $Y_0^*(1520)$ 51

3. $Y_1^*(1660)$ 56

4. $Y_1^*(1385)$ 57

5. $Y_0^*(1660)$ 57

6. $K^*(890)$ 58

7. $K^*(1440)$ 68

8. Kappa 69

B. Four-Body Final States

1. $\Sigma K\pi\pi$ 72

2. $\Lambda K\pi\pi$ 72

C. Five-Body Final States 78

V. Summary and Conclusions 82

Acknowledgments 83

Appendices

A. The Density Matrix Formalism 84

B. The Absorption Model 90

References 95

ANALYSIS OF STRANGE-PARTICLE RESONANT STATES FROM $\pi^- p$ INTERACTIONS

Lyndon Mauriece Hardy

Lawrence Radiation Laboratory
University of California
Berkeley, California

July 11, 1966

ABSTRACT

We systematically analyzed $\pi^- p$ interactions producing strange-particle final states with an incident laboratory momentum ranging from 1.6 to 4.2 BeV/c. We find these final states to be dominated by the production of well-established resonant states. No evidence was seen for the existence of new resonant phenomena.

The reactions $\pi^- p \rightarrow Y^0 K^{*0}$ and $\pi^- p \rightarrow Y^{0*} K^0$ proceed peripherally. Simple one-particle exchange does not describe the processes $\pi^- p \rightarrow \Sigma^0 K^{*0}$ and $\pi^- p \rightarrow \Lambda K^{*0}$. The absorption model gives an adequate fit to the data for these reactions and indicates the dominance of K^* exchange over K exchange.

I. INTRODUCTION

Strange-particle resonance states from $\pi^- p$ interactions have been investigated by many authors.[1-10] My report is an analysis in which the laboratory beam momentum ranges from 1.6 to 4.2 BeV/c.

The low BeV range of incident momentum for πp and Kp interactions has proven to be so rich in interesting physical phenomena that it has been rewarding to conduct bubble chamber experiments with no specific and detailed objective in mind. Instead, the data is collected and reduced in a systematic way. If the experimenters are fortunate, and in most cases they are, this first step in the analysis will indicate promising directions that can be pursued in detail fruitfully. The exploratory rather than the specific objective philosophy was the guiding principle for the collection of data that was analyzed and is presented here. As a result, the conclusions that we reach cover a variety of topics rather than specific definitive statements about any particular physical problem.

In Sec. II we outline the general procedures used in the primary analysis of the data and its preparation in useful form. The criteria used to separate the various reactions of interest are discussed. In Sec. III we describe the formulae and techniques used to obtain values for the total cross sections for the final states considered here. We find that all cross sections change with energy in a smooth fashion; resonance formation in the s channel is not indicated. In Sec. IV the properties of the resonant states produced in this experiment are discussed. We find no evidence for the existence of other than well-established states. Particular emphasis is placed upon the analysis of the reactions $\pi^- p \rightarrow \Sigma^0 K^{*0}$ and $\pi^- p \rightarrow \Lambda K^{*0}$, since information about the polarization states of both final-state particles can be inferred from their decays. Density matrix elements appropriate to these final states are found and the absorption model is fit to the data. We find these reactions to be dominated by K^* exchange rather than by K exchange.

II. EXPERIMENTAL PROCEDURE

A. Beam

This experiment was performed at the Lawrence Radiation Laboratory's Bevatron. The 72-inch liquid hydrogen bubble chamber was exposed to a beam of π^- mesons with laboratory momentum between 1.6 and 4.2 BeV/c. As the details of the beam design and operation are discussed elsewhere,[11] they are omitted here. In all, some 600 000 sets of stereo pictures were taken.

B. Scanning and Measuring

Each stereo set was examined by trained scanners for interactions with evidence of strange-particle production, and the indicative data for interesting events was recorded on a master list. The topologies sought are shown in Fig. 1. The numbers of events found as a function of incident momentum are listed in Table I and shown in Fig. 2. Rare interactions of interest--laptonic lambda decays, neutral interactions, and possible Ξ productions--were recorded separately and did not proceed through the normal processing described below. Each event was measured on a Frankenstein or a SMP.[12]

C. Fitting of Events

The data from each measurement were fed into a standard chain of Alvarez group computer programs[12] which reconstructed the topology in three dimensions and tried fitting a preselected set of reaction hypotheses to the event. The interactions we attempted to fit are shown in Table II. Only the reactions in Group I are discussed in detail here. The final states in Group II are treated elsewhere[13-14] and are mentioned only in connection with our obtaining pure samples of events in Group I. For each hypothesis, a four vector of the "missing momentum" was calculated by means of the formula

$$\underset{\sim}{P}_{mm} \equiv \underset{\sim}{P}_{inc} + \underset{\sim}{P}_{targ} - \sum_i \underset{\sim}{P}_i , \qquad (1)$$

where $\underset{\sim}{P}_{inc}$, $\underset{\sim}{P}_{targ}$, and the $\underset{\sim}{P}_i$ are measured (unfitted) values of the

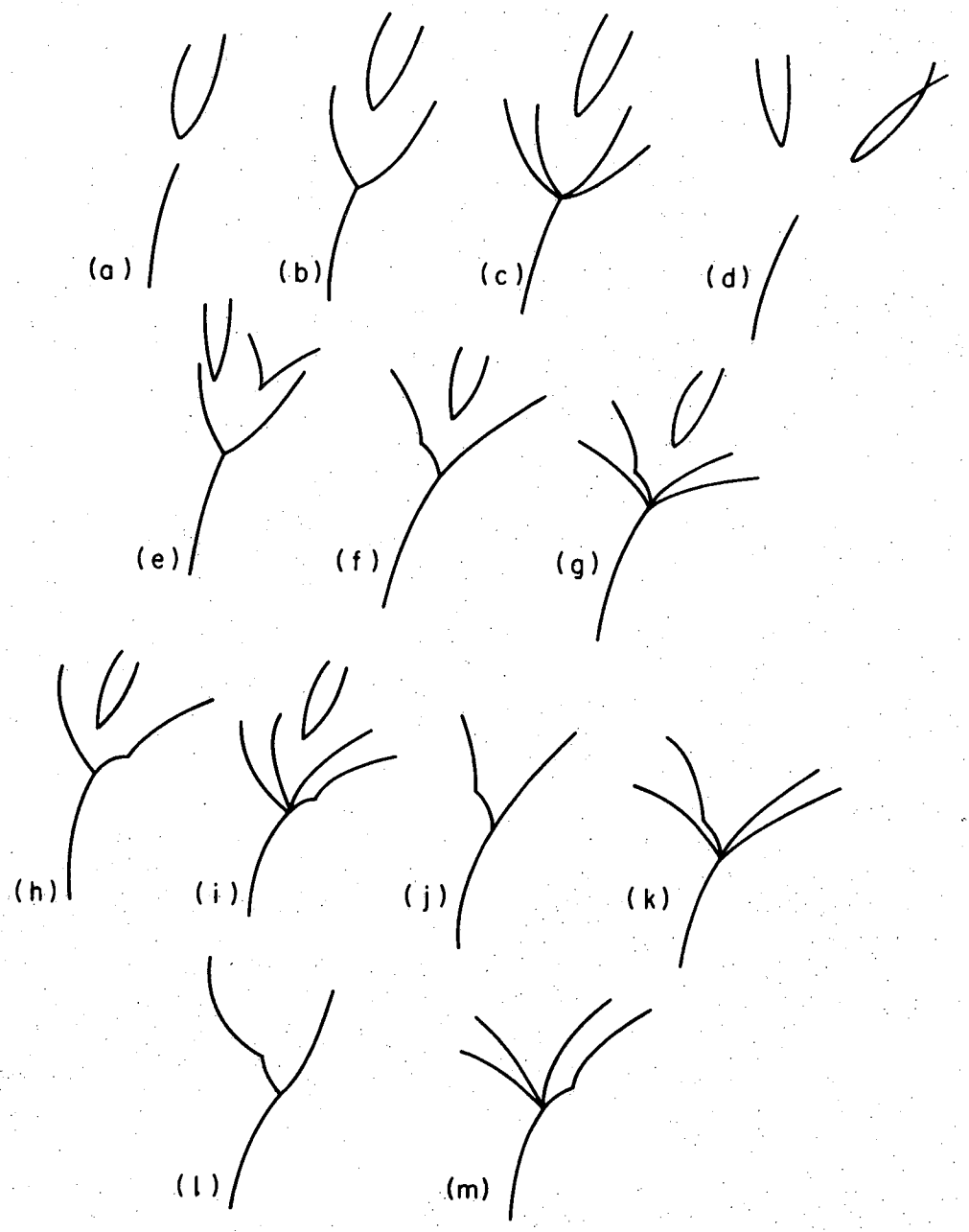

MUB-9839

Fig. 1. Topologies sought in this experiment:

a. Zero prong with a vee
b. Two prong with a vee
c. Four prong with a vee
d. Zero prong with two vees
e. Two prong with two vees
f. Two prong with a vee, positive decay
g. Four prong with a vee, positive decay
h. Two prong with a vee, negative decay
i. Four prong with a vee, negative decay
j. Two prong with a positive decay
k. Four prong with a positive decay
l. Two prong with a negative decay
m. Four prong with a negative decay

Table I. Number of events of each topology found at momentum intervals covered by this experiment.

Topology	Incident pion momentum (BeV/c)		
	1.6-2.3	2.5-3.4	3.7-4.3
a	4 540	4 458	1 264
b	2 101	5 417	2 499
c	0	127	180
d	1 750	1 597	430
e	55	579	312
f	325	458	151
g	0	8	11
h	508	607	179
i	0	11	21
j	591	523	588
k	13	228	189
l	3 193	2 340	657
m	18	452	339
Total	13 094	16 805	6 820

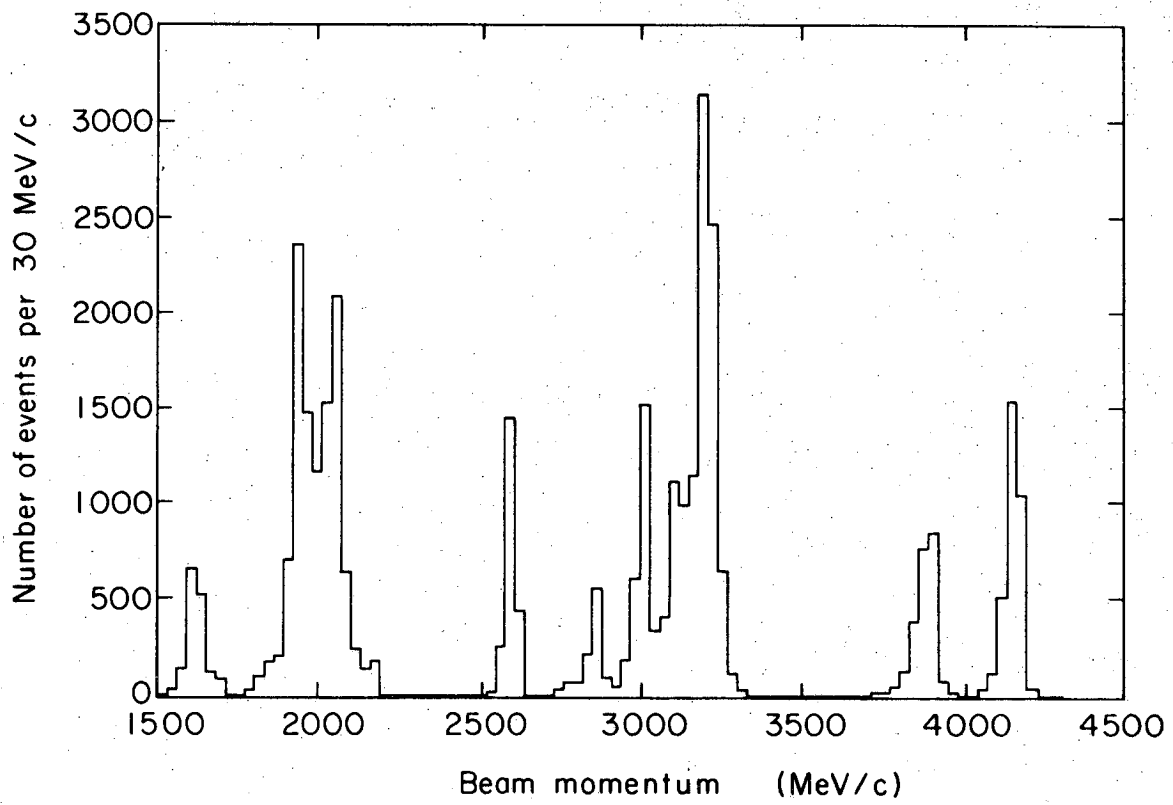

MUB-9840

Fig. 2. The number of strange-particle events found in this experiment as a function of incident pion momentum.

four momenta of the incident pion, target proton, and observed final-state particles (including neutrals with observed decays). The missing mass is defined by

$$(\mathrm{mm})^2 \equiv (\underset{\sim}{P}_{\mathrm{mm}})^2. \tag{2}$$

D. Separation of Hypotheses

For a given event, each hypothesis with nonzero constraints was assigned a confidence level which indicates the extent to which energy and momentum are conserved in the interactions. Presumably, events which do not proceed via the proposed interactions will have a low confidence level and therefore can be eliminated from consideration by imposing a minimum cutoff in this variable. The value chosen must be low enough to include desired interactions, yet high enough to exclude unwanted events, and in practice it is selected with some uncertainty. In this analysis, a hypothesis with nonzero constraints was considered acceptable if it had a confidence level greater than 0.005. Events with no acceptable production hypothesis with constraints but consistent with at least two missing neutrals at the production interaction were accepted as missing-mass hypotheses.

An event for which more than one hypothesis was acceptable was termed ambiguous. All ambiguous events which in principle could be resolved by an examination of the ionization density of one or more tracks were selected by a computer program and examined on a scanning table. Hypotheses inconsistent with the observed densities were eliminated.

After they were scanned on a scanning table, the ambiguities were most conveniently resolved by selecting the hypothesis with the highest confidence level. For many events we attempted to choose between hypotheses of different constraint class, however, and it is not clear that a confidence-level criterion is the selection to use. Instead the problems associated with each constraint class were examined in turn.

Resolution of Λ and K^0 decays was quite good. For events with a neutral decay, nearly all ambiguities occur between production hypotheses involving the same observed neutral. In all cases, therefore,

Table II. Hypotheses we attempted to fit.

Final state	Topology	Production constraint class	Total constraint class
GROUP I			
Three body			
$\Sigma^+K^0\pi^-, \Sigma^+ \to \begin{cases} p\pi^0 \\ n\pi^+ \end{cases}; K^0 \to \pi^+\pi^-$	f	4[a]	7
$\Sigma^+K^0\pi^-, \Sigma^+ \to \begin{cases} p\pi^0 \\ n\pi^+ \end{cases}$	j	1	1
$\Sigma^0K^+\pi^-, \Sigma^0 \to \Lambda+\gamma; \Lambda \to p\pi^-$	b, f	2	5
$\Sigma^0K^+\pi^-$	j	1	1
$\Sigma^-K^+\pi^0, \Sigma^- \to n\pi^-$	l	1	1
$\Sigma^-K^0\pi^+, \Sigma^- \to n\pi^-; K^0 \to \pi^+\pi^-$	h	4	7
$\Sigma^-K^0\pi^+, \Sigma^- \to n\pi^-$	l	1	1
$\Lambda K^+\pi^-; \Lambda \to p\pi^-$	b, f	4	7
$\Lambda K^+\pi^-$	j	1	1
$\Lambda K^0\pi^0; \Lambda \to p\pi^-, K^0 \to \pi^+\pi^-$	d	1	7
Λmm[b]; $\Lambda \to p\pi^-$	a	0	3
Kmm; $K^0 \to \pi^+\pi^-$	a	0	3
Four body			
$\Sigma^+K^+\pi^-\pi^-, \Sigma^+ \to \begin{cases} p\pi^0 \\ n\pi^+ \end{cases}$	k	4	4
$\Sigma^+K^0\pi^0\pi^-, \Sigma^+ \to \begin{cases} p\pi^0 \\ n\pi^+ \end{cases}$ $K^0 \to \pi^+\pi^-$	f	1	4
$\Sigma^0K^0\pi^+\pi^-, \Sigma^0 \to \Lambda\gamma;$ $\Lambda \to p\pi^-, K^0 \to \pi^+\pi^-$	e	2	8

Final state	Topology	Production constraint class	Total constraint class
$\Sigma^0 K^0 \pi^+ \pi^-$; $K^0 \to \pi^+\pi^-$	b	1	4
$\Sigma^- K^+ \pi^+ \pi^-$, $\Sigma^- \to n\pi^-$	m	4	4
$\Sigma^- K^0 \pi^+ \pi^0$, $\Sigma^- \to n\pi^-$; $K^0 \to \pi^+\pi^-$	h	1	4
$\Sigma^+ \pi^- mm$; $\Sigma^+ \to \begin{cases} p\pi^0 \\ n\pi^+ \end{cases}$	j	0	1
$\Sigma^- \pi^+ mm$; $\Sigma^- \to n\pi^-$	l	0	1
$\Sigma^- K^+ mm$; $\Sigma^- \to n\pi^-$	l	0	1
$\Lambda K^+ \pi^0 \pi^-$; $\Lambda \to p\pi^-$	b, f	1	4
$\Lambda K^0 \pi^+ \pi^-$; $\Lambda \to p\pi^-$, $K^0 \to \pi^+\pi^-$	e	4	10
$\Lambda K^0 \pi^+ \pi^-$; $\Lambda \to p\pi^-$	b	1	4
$\Lambda K^0 \pi^+ \pi^-$; $K^0 \to \pi^+\pi^-$	b	1	4
$\Lambda K^0 mm$; $\Lambda \to p\pi^-$, $K^0 \to \pi^+\pi^-$	e	0	6
$K^+ \pi^- mm$	j	0	0
$K^- \pi^+ mm$	l	0	0
<u>Five body</u>			
$\Sigma^+ K^+ \pi^0 \pi^- \pi^-$, $\Sigma^+ \to \begin{cases} p\pi^0 \\ n\pi^+ \end{cases}$	k	1	2
$\Sigma^+ K^0 \pi^+ \pi^- \pi$; $\Sigma^+ \to \begin{cases} p\pi^0 \\ n\pi^+ \end{cases}$, $K^0 \to \pi^+\pi^-$	g	4	8
$\Sigma^+ K^0 \pi^+ \pi^- \pi^-$; $\Sigma^+ \to \begin{cases} p\pi^0 \\ n\pi^+ \end{cases}$	k	1	2
$\Sigma^0 K^+ \pi^+ \pi^- \pi^-$; $\Sigma^0 \to \Lambda\gamma$, $\Lambda \to p\pi^-$	c, g	1	5
$\Sigma^0 K^+ \pi^- \pi^- \pi^-$	k	1	1
$\Sigma^- K^+ \pi^+ \pi^0 \pi^-$; $\Sigma^- \to n\pi^-$	m	1	2
$\Sigma^- K^0 \pi^+ \pi^+ \pi^-$; $K^0 \to \pi^+\pi^-$, $\Sigma^- \to n\pi^-$	i	4	8

Final state	Topology	Production constraint class	Total constraint class
$\Sigma^- K^0 \pi^+ \pi^+ \pi^-$; $\Sigma^- \to n\pi^-$	m	1	2
$\Sigma^+ K^0 \pi^- mm$; $\Sigma^+ \to \begin{cases} p\pi^0 \\ n\pi^+ \end{cases}$, $K^0 \to \pi^+\pi^-$	f	0	4
$\Sigma^- K^0 \pi^+ mm$; $\Sigma^- \to n\pi^-$, $K^0 \to \pi^+\pi^-$	h	0	4
$\Lambda K^+ \pi^+ \pi^- \pi^-$; $\Lambda \to p\pi^-$	c	4	7
$\Lambda K^+ \pi^+ \pi^- \pi^-$	g, k	1	1
$\Lambda K^0 \pi^+ \pi^- \pi^0$; $\Lambda \to p\pi^-$, $K^0 \to \pi^+\pi^-$	e	1	7
$\Lambda K^+ \pi^- mm$; $\Lambda \to p\pi^-$	b, f	0	3
$K^+ K^0 \pi^- mm$; $K^0 \to \pi^+\pi^-$	b, f	0	3
$\Lambda \pi^+ \pi^- mm$; $\Lambda \to p\pi^-$	b	0	3
$K^0 K^- \pi^+ mm$; $K^0 \to \pi^+\pi^-$	b, h	0	3
<u>Six body</u>			
$\Lambda K^0 \pi^+ \pi^- mm$; $\Lambda \to p\pi^+$, $K^0 \to \pi^+\pi^-$	e	0	6
GROUP II			
<u>Two body</u>			
$\Sigma^0 K^0$; $K^0 \to \pi^+\pi^-$	a	1	4
$\Sigma^0 K^0$, $\Sigma^0 \to \Lambda + \gamma$; $K^0 \to \pi^+\pi^-$, $\Lambda \to p\pi^-$	d	2	8
$\Sigma^- K^+$, $\Sigma^- \to n\pi^-$	l	4	4
ΛK^0; $K^0 \to \pi^+\pi^-$, $\Lambda \to p\pi^-$	d	4	10
ΛK^0; $\Lambda \to p\pi^-$	a	1	4
ΛK^0; $K^0 \to \pi^+\pi^-$	a	1	4

Final state	Topology	Production constraint class	Total constraint class
Three body			
pK^0K^-; $K^0 \to \pi^+\pi^-$	b, h	4	7
pK^0K^-	l	1	1
nK^+K^-	j, l	1	1
$nK^0\overline{K^0}$; $K^0 \to \pi^+\pi^-$, $\overline{K^0} \to \pi^+\pi^-$	d	1	7
Four body			
$pK^+K^-\pi^-$	k, m	4	4
$pK^0\overline{K^0}\pi^-$; $K^0 \to \pi^+\pi^-$, $\overline{K^0} \to \pi^+\pi^-$	e	4	10
$pK^0\overline{K^0}\pi^-$; $K^0 \to \pi^+\pi^-$	b	1	4
$pK^0K^-\pi^0$; $K^0 \to \pi^+\pi^-$	b, h	1	4
$nK^+\overline{K^0}\pi^-$; $\overline{K^0} \to \pi^+\pi^-$	b, f	1	4
$nK^0K^-\pi^+$; $K^0 \to \pi^+\pi^-$	b, h	1	4
pK^-mm	l	0	0
K^+K^-mm	j, l	0	0
$K^0\overline{K^0}mm$; $K^0 \to \pi^+\pi^-$, $\overline{K^0} \to \pi^+\pi^-$	d	0	6
Five body			
$pK^+K^0\pi^-\pi^-$; $K^0 \to \pi^+\pi^-$	c, g	4	7
$pK^+K^0\pi^-\pi^-$	k	1	1
$pK^+K^-\pi^0\pi^-$	k, m	1	1
$pK^0K^-\pi^+\pi^-$; $K^0 \to \pi^+\pi^-$	c, i	4	7
$pK^0\overline{K^0}\pi^0\pi^-$; $K^0 \to \pi^+\pi^-$, $\overline{K^0} \to \pi^+\pi^-$	e	1	7

Five body			
$pK^0\pi^-mm;\ K^0 \rightarrow \pi^+\pi^-$	b	0	3
$pK^0K^-mm;\ K^0 \rightarrow \pi^+\pi^-$	b, h	0	3
$nK^+K^-\pi^+\pi^-$	k, m	1	1
$nK^0K^0\pi^+\pi^-;\ K^0 \rightarrow \pi^+\pi^-,\ \overline{K^0} \rightarrow \pi^+\pi^-$	e	1	7

[a]Measured momentum of Σ not used.

[b]mm indicates two or more unobserved neutrals.

we needed to examine only the four types of constraint classes associated with production: no missing neutrals (four constraints), Σ^0 production (two constraints), one missing neutral (one constraint), and two or more missing neutrals (mm) (zero constraints).

1. Four-Constraint Fits

We expect the events which have an acceptable four-constraint fit to constitute a pure sample of four-constraint interactions. It is extremely unlikely that events for other processes can satisfy energy and momentum conservation sufficiently to yield a high confidence level. Possibly, however, measurement errors will be large enough that four-constraint events will give a high confidence level to hypotheses with only one or two constraints. Selection on the basis of confidence level will produce a pure sample of four-constraint events but not necessarily a complete one.

In this experiment the number of events which fit acceptably both four-constraint and one-constraint hypotheses is small, and testing our expectations is difficult because of the statistical limitations. Many events, however, are ambiguous between four and two constraints: Two-prong-vee events with the hypotheses $\pi p \rightarrow \Lambda K^+ \pi$ and $\pi^- p \rightarrow \Sigma^0 K^+ \pi^-$, $\Sigma^0 \rightarrow \Lambda\gamma$ (topology b). Events which truly proceed via the second reaction should show an isotropic decay of the Σ^0 in its rest frame, whereas misidentified events of the first type need not do so. Figure 3(a) shows the decay distribution for the decay gamma ray relative to the normal of the production plane for events which pass only Σ^0 production. We see the expected isotropic distribution. Events which have a best confidence level as Σ^0 production but also an acceptable fit to Λ production are shown in Fig. 3(b); here we see a striking peaking in the production plane. Figure 3(c) shows the same plot for a sample of events which have a best fit as Λ production but also an acceptable Σ^0 fit. We believe events in the third category to be true Λ events because of the stringent requirements of the four-constraint fit. The characteristics of the events in the second category are very similar to those of the third, and we will not have an isotropic Σ^0 decay distribution if many of the events

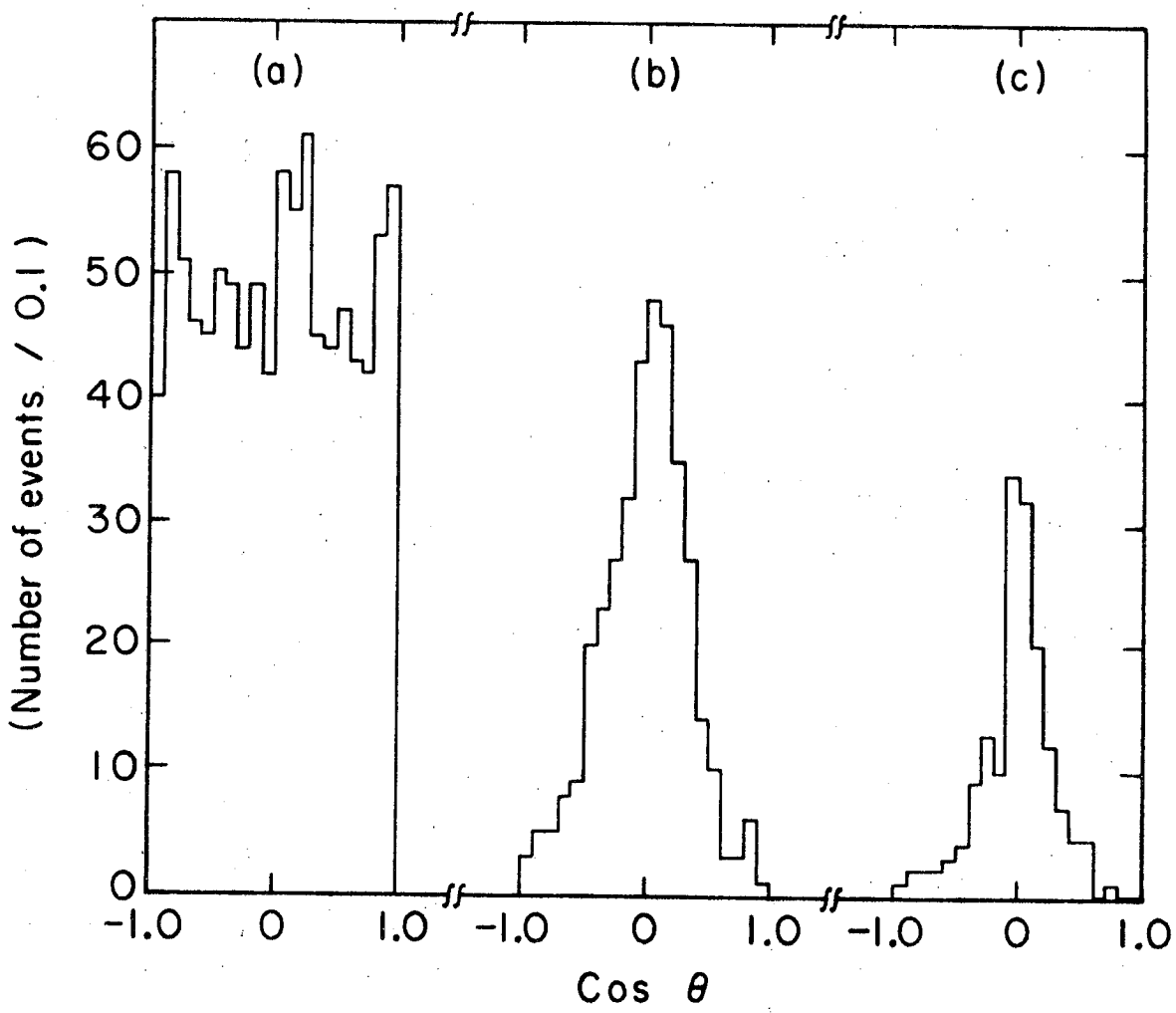

MUB-9841

Fig. 3. Angular distributions for the γ ray from Σ^0 decay with respect to the normal of the production plane of the final-state particles for (a) events with an acceptable hypothesis for only Σ^0 production, (b) events with the highest confidence level for Σ^0 production but also an acceptable Λ production hypothesis, and (c) events with the highest confidence level for Λ production but also an acceptable Σ^0 production hypothesis.

of the second category are accepted as coming from Σ^0 production. We conclude that all of the events in the second category are from Λ production.

If all events which simultaneously fit four and two constraints actually belong to the former hypothesis, then certainly ambiguous four- and one-constraint events should also be assigned to the four-constraint hypothesis. In this experiment, events which had an acceptable four-constraint fit were unambiguously chosen as such regardless of the confidence levels of other hypotheses. (In the few cases for which there was more than one acceptable four-constraint fit, the event was assigned to the hypothesis with the higher confidence level.) We believe that this procedure yields pure and complete samples of four-constraint events.

2. Two-Constraint Fits

Upon examining the two-constraint hypothesis $\pi p \rightarrow \Sigma^0 K^+ \pi^- \Sigma^0 \rightarrow \Lambda\gamma$ after the removal of ambiguous $\Lambda K^+ \pi^-$ events, we find a significant number of ambiguities only with the reaction $\pi p \rightarrow \Lambda K^+ \pi^- \pi^0$. Since the Σ^0 decays rapidly, it does not travel far ($< 10^{-3}$ cm) from the production interaction before decay, and the process could be viewed as $\pi^- p \rightarrow \Lambda K^+ \pi^- \gamma$. The experimental resolution is such that it is hard to distinguish between a γ ray and a π^0 by an examination of the missing mass at the production vertex. We can use the additional fact, however, that for true Σ^0 production events, the effective mass of the Λ and missing mass, $(\underset{\sim}{P}_\Lambda + \underset{\sim}{P}_{mm})^2$ should peak at the mass of the Σ^0, whereas for π^0 production events, this quantity should lie above the kinematic threshold of 1.56 $(\text{BeV})^2$. Figure 4(a) is a scatter plot of the missing mass square versus the effective mass square of the Λ and missing mass for events which fit only Σ^0 production. Figure 4(b) is the same plot for events which pass only π^0 production. In Fig. 4(c) are plotted those events which have acceptable fits as both Σ^0 and π^0 production but for which the Σ^0 hypothesis has a higher confidence level. Figure 4(d) contains ambiguous events with a higher confidence level for π^0 production. In general, a selection in confidence level seems to do well in separating the hypotheses, but the distribution of points suggest that there is some

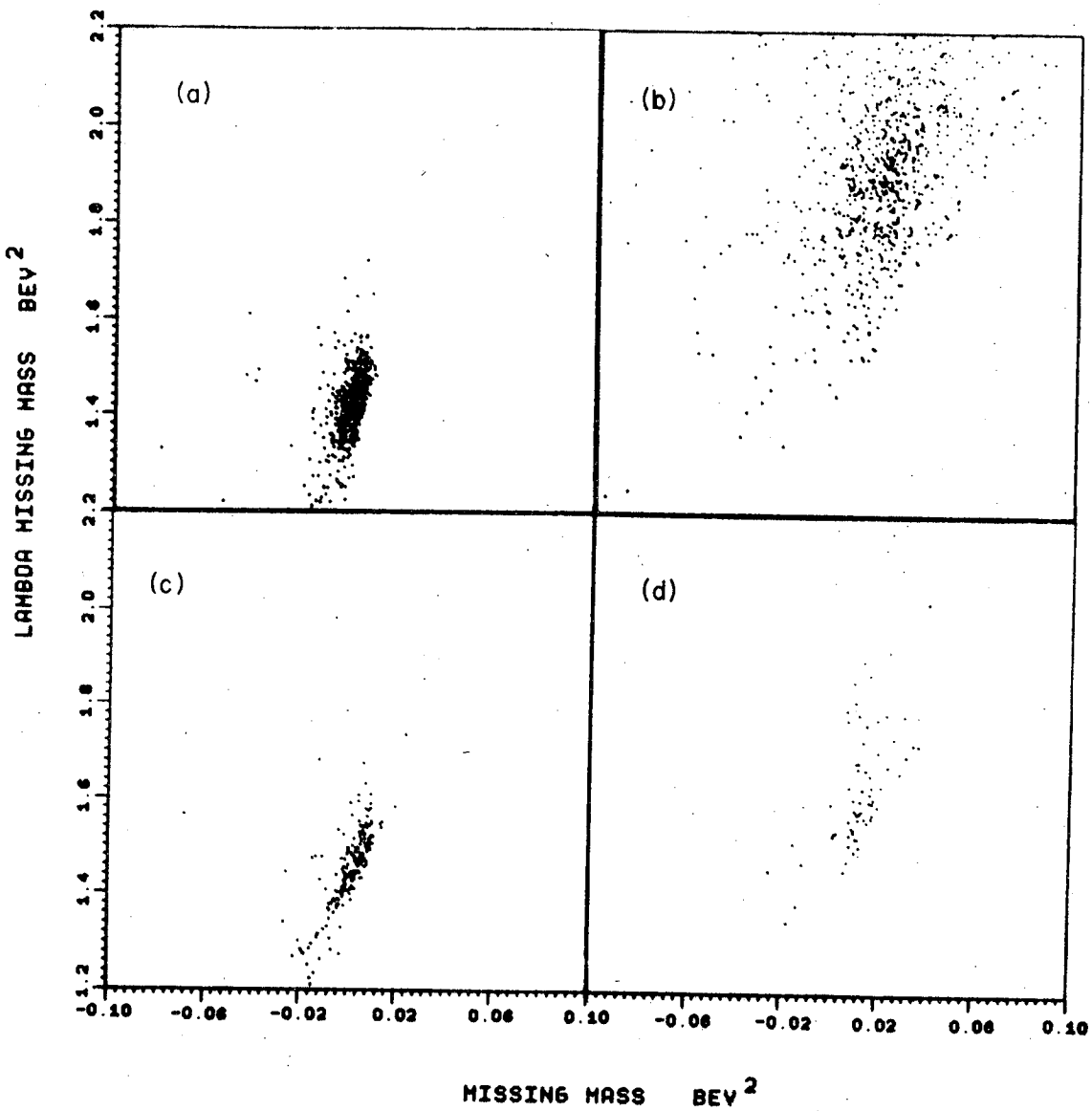

MUB-10734

Fig. 4. Scatter plots of the (missing mass)^2 versus the effective-mass squared of the lambda and missing mass for (a) events with only an acceptable Σ^0 hypothesis, (b) events with only an acceptable $\Lambda\pi^0$ hypothesis, (c) events with both Σ^0 and $\Lambda\pi^0$ production hypotheses and with a higher confidence level for Σ^0 production, and (d) events with both Σ^0 and $\Lambda\pi^0$ production hypotheses and with a higher confidence level for $\Lambda\pi^0$ production.

misassignment. Ambiguous events were assigned, therefore, on the basis of the effective mass of the Λ and missing mass. Events with $(\underset{\sim}{P}_\Lambda + \underset{\sim}{P}_m)^2 \geq 1.56\ (\mathrm{BeV})^2$ were assigned to the π^0 production hypotheses; events with $(\underset{\sim}{P}_\Lambda + \underset{\sim}{P}_m)^2 < 1.56\ (\mathrm{BeV})^2$ were assigned to the Σ^0 production hypothesis. The cross contamination of these two channels should then be quite small. The same criterion was applied to the separation of $\pi^- p \rightarrow \Lambda K^0 \pi^0$ from $\pi^- p \rightarrow \Sigma^0 K^0$ and $\Sigma^0 \rightarrow \Lambda\gamma$.

3. <u>One-Constraint Fits</u>

For each one-constraint hypothesis that involves the production of a single missing neutral, there exists another reaction with the same observed particles but with two or more missing neutrals. In general, the kinematic threshold for the effective mass of two missing neutrals is sufficiently removed from the mass of the single neutral so that the hypotheses can be separated by examining the missing mass at the production interaction. For one-constraint hypotheses involving observed Λ decays, however, we must discriminate between Λ production reactions and corresponding reactions in which a Σ^0 is produced instead of a Λ. In the former case, the missing-mass spectrum will show a peak at the mass of the missing neutral with a width characteristic of the experimental resolution. In the latter case, the missing mass will be the effective mass of the neutral and the gamma ray from Σ^0 decay and will range upward from a threshold very near the mass of the neutral. Hence, there is no clear-cut separation of the two channels and we must accept a contamination in the Λ final state. Examination of missing-mass spectra for this experiment shows that the greatest degree of contamination occurs for the final state $\Lambda K^0 \pi^+ \pi^-$ (events with Λ^0 observed decay, no observed K^0 decay) at the higher incident momenta where the peak at the missing K^0 is broadest. (We, of course, also have four-constraint events for this final state from topology e, in which both the Λ and K^0 decay are seen). This missing-mass square distribution for events accepted as either $\Lambda K^0 \pi^+ \pi^-$ or $\Lambda \pi^+ \pi^-$ mm is shown in Fig. 5. We accept as one-constraint fits events which have a (missing mass)^2 below 0.340 BeV^2, thereby acquiring nearly all of the desired events and

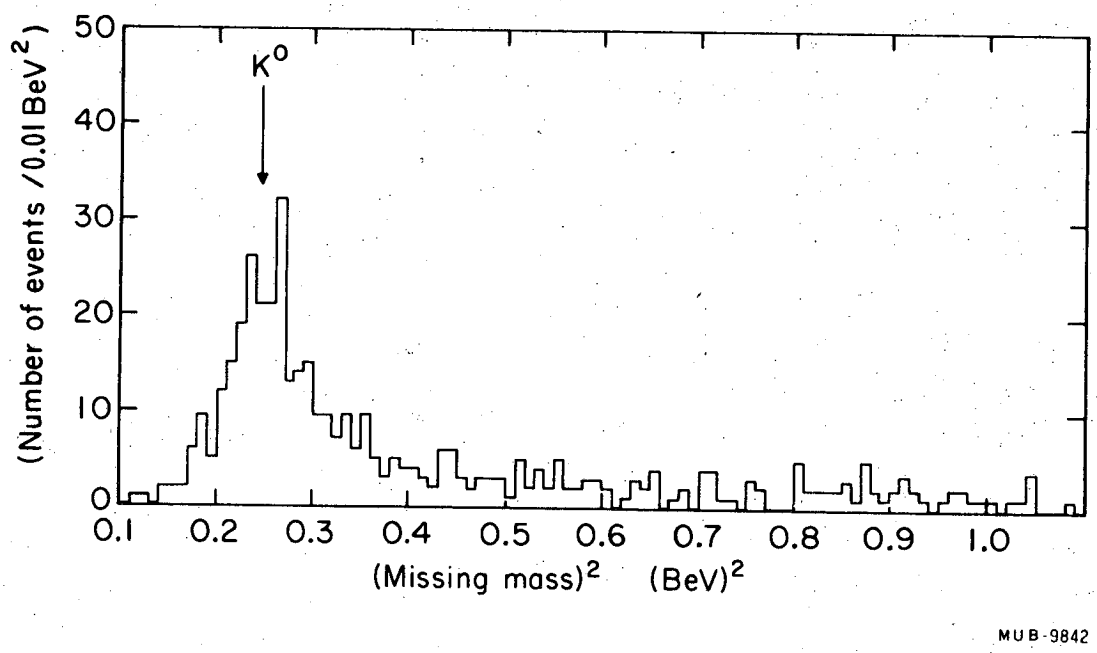

Fig. 5. Histogram of the (missing mass)^2 for events accepted as from either $\Lambda\pi^+\pi^-K^0$ or $\Lambda\pi^+\pi^-$ mm production.

accepting a contamination of less than $\approx 5\%$. At lower incident momenta and in other channels, the resolution is better than this and the contamination is correspondingly less. In this experiment, events were accepted as one-constraint fits if the hypothesis had an acceptable confidence level and the missing mass fell within limits appropriate to the hypothesis. Contamination from zero-constraint events was then quite small.

According to our liberal definition of ambiguity, not all one-constraint events had an unique interpretation. After scanning table examination and resolution of four- and two-constraint events, three categories of ambiguities remained. These were (a) ambiguities between $K^0\pi^+$ and $K^+\pi^0$, (b) events from topology b (two prong and a vee) with observed K^0 decay, and (c) events from topologies j and k (two or four prongs with a positive decay) with no acceptable Σ^+ hypothesis.

The hypotheses in category (a)--$\Lambda\pi^-K^+\pi^0$ and $\Lambda\pi^-K^0\pi^+$, $\Sigma^-K^+\pi^0$ and $\Sigma^-K^0\pi^+$, $\Sigma^+\pi^-\pi^-K^+\pi^0$ and $\Sigma^+\pi^-\pi^-K^0\pi^+$, and $\Sigma^-\pi^+\pi^-K^+\pi^0$ and $\Sigma^-\pi^+\pi^-K^0\pi^+$-- are all approximately 25% ambiguous. A plot of confidence level of one hypothesis versus that of the other for ambiguous $\Lambda\pi^-K^+\pi^0$ and $\Lambda\pi^-K^0\pi^+$ events is shown in Fig. 6. There exists no clear-cut division of the events. The plots for the other ambiguous hypothesis pairs are similar. For the final state $\Lambda\pi^-K^0\pi^+$, we can use the number of four-constraint events that have observed Λ and K^0 decays to calculate how many one-constraint events we should see (all properly weighed as discussed in Sec. III). We find that allocating the ambiguous events by the usual procedure of higher confidence level gives a number of one-constraint $\Lambda\pi^-K^0\pi^+$ events consistent with our expectation. This observation does not test the possibility of cross contamination of events, however.

Events of the final states $\Lambda K^-K^0\pi^+$, $\Lambda\pi^-K^+\pi^0$, $\Sigma^-K^+\pi^0$, and $\Sigma^-K^0\pi^+$ were generated by the program FAKE,[15] and processed through the fitting programs in the same way as the actual events in the experiment. If we assigned events on the basis of higher confidence level, for these samples we obtained a cross contamination of approximately 7%.

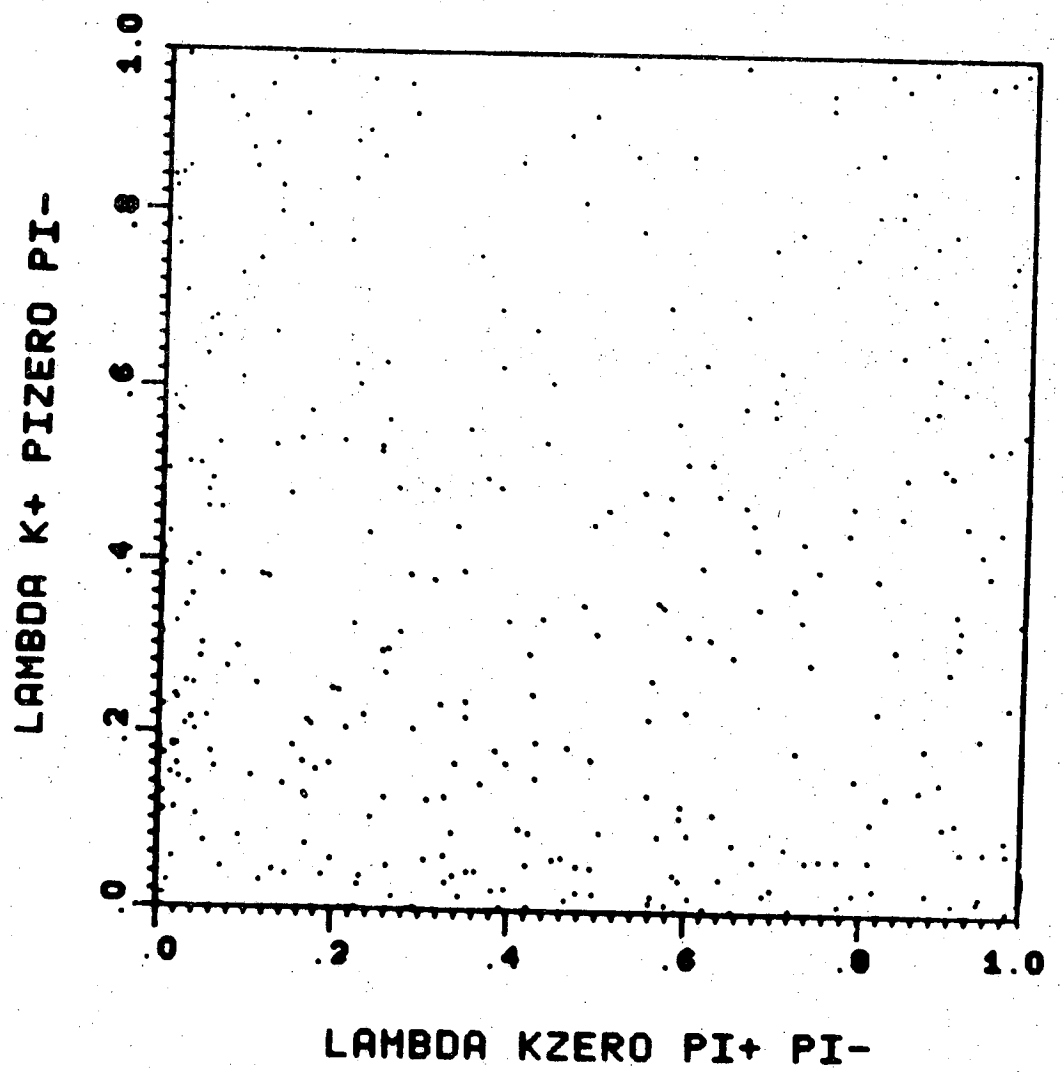

Fig. 6. Scatter plot of the confidence levels for the two production hypotheses $\Lambda K^+\pi^0\pi^-$ and $\Lambda K^0\pi^+\pi^-$.

Effective-mass plots for both unambiguous and ambiguous events for these four final states were examined and no statistically significant differences were observed.

Rather than discard a quarter of the events for the final states in category (a), ambiguous events were assigned on the basis of confidence level and the small background contamination accepted.

Events of category (b) were 60% ambiguous with K pair production hypotheses. Assignment on the basis of confidence level yielded numbers of events in the channels $\Lambda K^0\pi^+\pi^-$ and $\Sigma^0K^0\pi^+\pi^-$ inconsistent with those expected from the numbers of four-constraint events in which the lambda decay was observed. Analysis of events generated by FAKE indicated large cross contaminations with K pair hypotheses when events were assigned on the basis of confidence level only. Since relatively pure samples of events for the final states $\Lambda K^0\pi^+\pi^-$ and $\Sigma^0K^0\pi^+\pi^-$ were obtainable from events in which the Λ decay was seen, events in category (b) were not used in the subsequent analysis.

Events in category (c) also were highly ambiguous with K pair hypotheses. In addition, the K^+ track is in general rather short for topologies j and k, and its decay is not fit. The momentum determination for this track is poor and we expect considerable contamination in these final states from elastic scatters of positive particles in which the recoil proton is not seen. For the final states $\Lambda K^+\pi^-$ and $\Sigma^0K^+\pi^-$, the numbers of events from topology j (two prong, positive decay) are in disagreement with those expected from the numbers from topology f (two prong, positive decay and a vee). Events which fit the hypotheses $\Lambda K^+\pi^-$, $\Sigma^0K^+\pi^-$, $\Lambda K^+\pi^+\pi^-\pi^-$, and $\Sigma^0K^+\pi^+\pi^-\pi^-$ from topologies j and k were not used in the subsequent analysis.

Less than 5% of the one-constraint events not in the three categories discussed above were ambiguous. The contamination in these final states should be quite small.

We conclude that by a judicious selection of events we can acquire unbiased and relatively pure samples of one-constraint events. The contaminations from other final states are sufficiently low that they will have negligible effect on the conclusions that we draw from these data.

4. Zero-Constraint Events

With the exceptions of the final states ΛK^0 mm and $\Lambda K^0 \pi^+ \pi^-$ mm, missing-mass hypotheses for a given topology are ambiguous. An examination of ionization densities eliminated ambiguity in some instances, but the bulk of zero-constraint events have more than one missing-mass interpretation consistent with all of the information at our disposal. The final state ΛK^0 mm is discussed in Sec. IV. A; other missing-mass hypotheses were not examined for this report.

E. Primary Data Reduction

The majority of events found by the scanners was measured and processed by the fitting programs. A small percentage was classified as unmeasurable and for cross-section calculations these were distributed among the various final states in a manner proportional to the events which were fully processed. Certain events were not measured for a variety of reasons. A vertex could have been obscured in one or more views, or a track could have been distorted by turbulence, for example. Into this unmeasured category also went events overlooked because of bookkeeping errors and for which appropriate film was unavailable.

Events that were recorded by mistake (not one of the topologies in Fig. 1) were placed in a reject category when examined on the measuring device by the more experienced scanners. In subsequent states of processing, more interactions were transferred to this category.

Hypothesis failures (events for which no hypothesis had an acceptable fit) were remeasured since many of the failures were the result of operator oversights and poor measuring techniques. Events which failed twice were re-examined by specially trained scanners and physicists to ascertain the cause of failure. Most of these examined events did not involve strange-particle production and were rejected; some were good events that had to be remeasured with special care, and some were left as unexplained failures.

Table III shows the status of the events in the experiment at the conclusion of the present analysis. Almost all of the events were either assigned a good interpretation or were rejected. The residual of failing

events amounts to only 4% of the total sample; because part of this sample is desirable events whose confidence level is below 0.005, a more intensive and sophisticated analysis would probably discover the reason for their failure. Cleaning up this residual would have negligible effect on the results described in this report. Cross-section values were corrected for the good events estimated to have confidence levels below 0.005.

Table III. Final status of strange-particle events.

Number of	Unmeasured	Reject	Failures	Passing
events	2085	8910	1871	36,722
Percentage	0.04	0.18	0.04	0.74

III. CROSS SECTIONS

Much effort must be expended to obtain cross sections of $\pi^- p$ interactions in a bubble chamber experiment. The details of our procedure are presented in sections A through D below. The reader interested only in the results may skip to Sec. III.E where they are presented.

A. The Cross-Section Scan

Any attempt to find cross sections with the formula

$$\sigma = N/\rho\ell \tag{3}$$

where σ is the cross-section, N the number of interactions, ρ the density of the target particles, and ℓ the total path length of the beam, runs into serious difficulty in evaluating the total path length. The beam is contaminated with μ^-, from π^- decays in flight, which create tracks in the chamber that look like noninteracting π^-'s. Path-length estimates based on the number of incident tracks would be biased high by an unknown amount. In experiments with an incident K^- beam, this difficulty is circumvented by an analysis of the number of τ decays in flight of the beam, but the π^- possesses no decay of high probability and high detectability that could be used in this fashion. In some π^- experiments the contamination has been determined either by reading Čerenkov counters placed along the beam or by analyzing the distribution of energy of δ rays from incident tracks. In our case, Čerenkov counter data was not available, and we felt that measuring machines were better utilized when they measure events of interest than when they measured δ rays. Instead, we requested a special cross-section scan that essentially found the ratio of strange-particle interactions to the total number of interactions. This ratio times the total $\pi^- p$ cross section as accurately determined from counter experiments[16-17] then in principle yields the quantities of interest. This approach must be followed with some care, however, as discussed below.

The entire exposure was divided into a series of intervals over which the experimental conditions were relatively constant, rolls of film were randomly selected from each interval, and every fifth frame was

examined by scanners. The scanners recorded both the total number of interactions of all types observed, and the number of incoming beam tracks at the entrance window; they then checked to see that their difference was the number of outgoing tracks at the end of the chamber. This check ensured that no zero-prong interactions were missed. The number of interactions involving strange particles, as well as the numbers of zero-, two-, four-, and six-prong interactions, were also recorded. This data from intervals with the same incident momentum were then grouped.

The total number of interactions observed by the scanners is of course subject to the usual scanning biases associated with a bubble chamber experiment. By far the greatest number of missed events came from very-small-angle elastic scatters that were recorded as noninteracting beam tracks. Fortunately the film for this report was also scanned for two-prong interactions, and these were analyzed similarly to the strange-particle states. The details of this analysis, discussed elsewhere,[18] provide a means of determining the two-prong-interaction scanning efficiency. (Four and six-prong interactions are discussed in Reference 19.) An examination of the differential cross section of elastic-scatter events at each momentum obtained from this general two-prong study showed a characteristic exponential decrease with increasing momentum transfer, except for a rapid falloff of events in the extreme forward direction because of the scanning bias. Fitting the events to an exponential curve and then extrapolating back to zero and integrating gives a value for the total number of events actually in the sample. At all momenta the ratio of total two-prong events to the observed two prong events was 1.10 ± 0.03. The corrections to events in other categories are quite small compared to this and were neglected. The total number of interactions in the film was then computed as

$$N_{tot} = N_{op} + N_{2p} + N_{4p} + N_{6p} + N_{strange}, \qquad (4)$$

and the "observed" cross section for each momentum interval calculated from

$$\sigma_s = \sigma_{tot} N_{strange}/N_{tot}, \qquad (5)$$

where σ_s is the observed strange-particle cross section, and σ_{tot} is the total $\pi^- p$ cross section.

Information on all events scanned in the experiment, whether they eventually proved to be valid or not, was retained on the master list. To find the cross section for some reaction on some momentum interval, we need to know only the total number of events in the film, corrected for all detection and scanning biases, and the corresponding number of scanned events for the same momentum interval on the master list

$$\sigma_i = N_i \sigma_s / N_{ml} = N_i N_{strange} \sigma_{tot} / N_{ml} N_{tot} = \alpha N_i \qquad (6)$$

where N_i is the number of events of interest, N_{ml} is the number of corresponding masterlist events, and σ_i is the desired cross section. Using this method we can cancel out the large biases associated with $N_{strange}$ and $N_{m\ell}$, and we are left only with the problem of determining the corrections to the observed number of good events in the desired channels. These corrections are of three general types--scanning, measuring, and detecting. Each type is discussed below. Values for α as a function of incident momentum are shown in Table IV.

Table IV. Microbarns per event for each momentum interval.

Momentum interval (BeV/c)	μb per event
1.590-1.640	0.411 ± 0.053
1.915-1.960	0.260 ± 0.020
1.960-2.015	0.352 ± 0.055
2.015-2.080	0.200 ± 0.016
2.080-2.190	1.19 ± 0.13
2.580-2.630	0.339 ± 0.029
2.825-2.895	0.959 ± 0.081
2.960-3.065	0.387 ± 0.036
3.065-3.175	0.287 ± 0.020
3.175-3.245	0.148 ± 0.008
3.840-3.930	0.398 ± 0.040
4.130-4.190	0.323 ± 0.028

B. Scanning Corrections

The scanning corrections considered here are of three types--topological, fiducial, and accidental. Topological biases occur because scanners have greater difficulty in finding events of certain configurations than they do others. Charged or neutral particles that decay very near to the production vertex are more readily missed than those that decay some distance away from it. Plots of the number of events versus the proper time of decay show the proper exponential behavior beyond a minimum value. In the cross-section analysis, therefore, only those events, properly weighted, which have decays beyond a length of 0.5 cm were used.

Decaying Σ^+'s and Σ^-'s in which the direction of the charged secondary makes a small angle with the direction of the primary itself were also preferentially missed. Corrections for cross-section biases from this effect were easily made by examining the decay distribution in the sigma rest frame which should be isotropic, but in fact has a depletion of events for the charged secondary decaying along the direction of the sigma. In the case of the Σ^+ decaying via $p\pi^0$, a significant number of events at all decay angles were not recorded by scanners because such events looked very much like proton-proton scatters with nonvisible recoils. The decay mode $n\pi^+$ was not biased in this way because the ionization density of the outgoing π^+ was in general less than that of the sigma; this cannot happen in a proton-proton elastic scatter. The cross sections for final states containing a Σ^+, therefore, were determined by using only the $n\pi^+$ decay mode and by multiplying the number of events by two.

When the scanning instructions were written, only general loose criteria were provided for the elimination of zero-opening-angle vees that were electron pairs. A later analysis of the expected distribution of opening angles revealed that a negligible percentage of all K^0 and Λ events should have zero opening angle in the laboratory system. Events with acceptable fits and zero opening angles were most likely to be from electron pairs with poor momentum determinations. In the subsequent

analysis, events with vees were accepted only if the opening angle in the laboratory system was greater than 1.5 degree; this criterion eliminated all bias from this source.

The three cameras that view the bubble chamber look down from above with a line of sight roughly in the z direction. Thus, vee decays in which the decay-plane normal is perpendicular to this direction might more readily be missed than those whose normals are parallel to this direction. The "perpendicular" vees would appear to have a small opening angle and might be discarded as electron pairs by the scanners, whereas the "parallel" vees are in a optimum orientation for viewing. To investigate the possibility of a bias from this effect, we plotted the quantity $\cos^{-1}[(\widehat{\hat{N}\times P_1})\cdot(\widehat{P_1\times P_2})]$ for all K^0 and Λ decays; here $\underset{\sim}{P}_1$ is the laboratory momentum of the neutral, $\underset{\sim}{P}_2$ is the laboratory momentum of a charged secondary, and $\hat{N}$ is a unit vector along the z (vertical) axis. This quantity, which measures the isotropy of the decay normal about the neutral direction, would not be flat if a bias existed for detecting vee decays of certain orientations. In this experiment the distribution was consistent with isotropy so no corrections were necessary.

The probability of finding events near the boundaries of the chamber is lower than in the chamber center because of poorer illumination near the boundaries. Because interactions near the far end of the chamber are likely to produce tracks that are relatively short, the measurement errors will be greater for these events and the possibility of misidentification is enhanced. Turbulence is greater near the chamber boundaries and measured values of momenta will thus be poor in these regions. For these reasons, only events in a restricted fiducial volume were accepted for analysis. These events were properly weighted for cross-section determinations to take into account the different volumes used in the cross-section scan and the following analysis:

By restricting ourselves to the subsample of events by the criteria above, we have obtained a collection of events for which the scanning efficiency is constant but not necessarily equal to unity. A surprisingly

large fraction of events missed by scanners are in plain sight in the center of the chamber and have good topological features. These "accidental" oversights, presumedly caused by monotony, carelessness, or fatigue, are not expected to bias the data in any significant way except to cause cross-section estimates to be systematically low. To find the magnitude of this effect, the entire exposure of film was scanned a second time and a second scan master list was prepared in the same manner as the first. The two master lists were compared and a list was compiled of all events which were (a) found on scan one but not on scan two, and (c) found on both scans but assigned to different topologies. One might be tempted to take the number of events in categories (a) and (b), and the number of events on the master lists that agree, and from these compute the scanning efficiency for each topology. In a complicated scan such as this one, however, such a technique would be in error. Both scans and hence the data from the "conflict" analysis will contain nonvalid events. In fact, such events will preferentially appear on one scan and not the other because of the varying abilities of the scanners to distinguish between events such as, for example, electron pairs and vees and charged decays and scatters. Also, only part of an event might be missed--one of two vees in a zero-prong-two-vee event, for example. The following procedure was adopted, therefore, to take into account the complications present for this experiment.

A scanner looked at the events on the conflict list a third time, decided between different topology assignments, and rejected obvious nonstrange-particle events found on the second scan but not on the first. All accepted second scan events that were not on the first master list were then processed through the primary data-analysis system used for the first scan. A sample of 5000 conflict events was then selected and the events of this sample for each topology were divided into eight classes:

1. Good event found by scan 1 but not by scan 2.
2. Good event found by scan 2 but not by scan 1.
3. Good event found and wrong topology assigned by scan 1; not found by scan 2.
4. Good events found and wrong topology assigned by scan 2; not found by scan 1.
5. Good event found by scans 1 and 2, but wrong topology assigned on scan 2.
6. Good event found by scans 1 and 2, but wrong topology assigned on scan 1.
7. Reject event found by scan 1 but not by scan 2.
8. Reject event found by scan 2 but not by scan 1.

These eight quantities are related as shown in Table V.

Table V. Assignment of events from conflict analysis.[a]

	Scan 1				
Scan 2	Good event	Good event, wrong topology assigned	Good event, not found	Reject event	Reject event not found
Good event	X	6	2	X	X
Good event, wrong topology assigned	5	X	4	X	X
Good event, not found	1	3	X	X	X
Reject event	X	X	X	X	8
Reject event, not found	X	X	X	7	X

[a]Numbers given for classes are described in text.

We assume that the topological and fiducial errors already discussed are strongly correlated between the two scans but that the accidental errors are entirely uncorrelated and can be characterized by independent probabilities for each scan as follows.

We define the five quantities

p_{1i} = probability of finding a correctly assigned event on scan i.

p_{2i} = probability of finding but incorrectly assigning event on scan i.

p_{3i} = probability of finding a nonvalid event on scan i.

T_g = total number of good events in the film

T_b = total number of nonvalid (bad) events in the film.

The quantities p_{31}, p_{32}, and T_b are not of interest but serve as sort of Lagrange multipliers in the problem. With these definitions we can then write expressions for the number of events observed in each of our eight categories and on the master lists.

$$
\begin{aligned}
N_1 &= P_{11}(1 - P_{12} - P_{22})T_G \\
N_2 &= P_{12}(1 - P_{11} - P_{21})T_G \\
N_3 &= P_{21}(1 - P_{12} - P_{22})T_G \\
N_4 &= P_{22}(1 - P_{11} - P_{21})T_G \\
N_5 &= P_{11}P_{22}T_G \\
N_6 &= P_{12}P_{21}T_G \\
N_7 &= P_{31}(1 - P_{32})T_B \\
N_8 &= P_{32}(1 - P_{31})T_B \\
N_{ML1} &= (P_{11} + P_{21})T_G + P_{31}T_B \\
N_{ML2} &= (P_{12} + P_{22})T_G + P_{32}T_B,
\end{aligned}
\tag{7}
$$

where N_{MLi} = the number of events recorded on master list i. For each topology we now have 10 observed quantities and 8 unknown parameters to fit them. A chi-square was computed for these quantities and minimized. The results are presented in Table VI. The numbers rank

themselves in the expected way with vee-four-prong events having the best chance of being found and two-prong positive decays the least. The percentage of misidentified events in some categories is nonnegligible. These efficiencies were taken into account in cross-section computations.

C. Measuring Corrections

This correction is for the unmeasured and unmeasurable events that were allocated in a manner proportional to the events that did proceed through the system. An average weight was assigned to each event placed in the passing category.

D. Detection Corrections

In addition to corrections for the low scanning efficiency for short decay lengths, the finite size of the bubble chamber must be taken into account also. Accordingly, each observed decaying particle was weighted by a factor

$$1/(e^{-t_{min}/\tau} - e^{-t_{max}/\tau}) \tag{8}$$

where t_{min} is the time corresponding to the minimum length cutoff discussed above and t_{max} is the maximum available proper time for a given event. The distance from the production interaction to the intersection of the particles trajectory with the fiducial volume boundary plane, and the fitted value of the particle momentum were used to obtain t_{max}. No correction was made for the nonlinear path of charged sigmas; the error introduced was very small. Events with unobserved neutrals were weighted by

$$\frac{1}{1 + \frac{1-b}{b} \exp(-t_{max}/\tau)} \tag{9}$$

where b is the branching percentage of such events into neutral decay products.

Since the weights depend upon the lifetimes of weakly decaying particles, we analyzed our events to see if their decay distributions

Table VI. Scanning efficiencies for each topology.

Topology	P_{11}	P_{21}	P_{12}	P_{22}
a	0.918 ± 0.005	0.012 ± 0.002	0.921 ± 0.005	0.016 ± 0.002
b	0.924 ± 0.005	0.010 ± 0.002	0.921 ± 0.005	0.014 ± 0.002
c	0.924 ± 0.025	0.035 ± 0.016	0.944 ± 0.021	0.029 ± 0.015
d	0.936 ± 0.008	0.047 ± 0.007	0.926 ± 0.009	0.055 ± 0.008
e	0.898 ± 0.021	0.089 ± 0.020	0.881 ± 0.023	0.096 ± 0.021
f	0.871 ± 0.027	0.102 ± 0.023	0.817 ± 0.031	0.119 ± 0.025
g[a]	- -	- -	- -	- -
h	0.905 ± 0.016	0.072 ± 0.015	0.868 ± 0.014	0.120 ± 0.013
i[a]	- -	- -	- -	- -
j	0.849 ± 0.016	0.008 ± 0.004	0.875 ± 0.014	0.011 ± 0.004
k	0.932 ± 0.022	0.006 ± 0.008	0.919 ± 0.026	0.011 ± 0.004
l	0.881 ± 0.008	0.005 ± 0.002	0.897 ± 0.008	0.010 ± 0.002
m	0.972 ± 0.010	0.023 ± 0.009	0.937 ± 0.018	0.022 ± 0.014

[a]There were too few events with these topologies to obtain statistically significant value. For cross-section calculations the values fot topologies k and m were used.

were consistent with published values. The distributions and best fits obtained from a maximum-likelihood method are shown in Fig. 7. We find values consistent with world averages for the K^0, Λ^0, and Σ^+. For the Σ^-, however, we obtain a value of $(1.35 \pm 0.04) \times 10^{-10}$ seconds. Our sample of events is large enough that the largest contributor to errors might well be systematic rather than statistical. We are now searching for systematic effects but the results will appear elsewhere. In this report we have used the value obtained here for weighting our events. Had we used the world average value, the primary effect would be to lower by $\approx 3\%$ our total cross-section estimates for channels with Σ^- production.

E. Results

In Table VII and VIII are tabulated the total cross sections and errors for the final states described here. Figures 8 and 9 illustrate the variation of cross section with momentum for the three-body final states and the four-body final states with lambda production, respectively. The three-body final-state values are all characterized by a rather rapid rise from threshold to maximum in the vicinity of a c.m. energy of ≈ 2.3 BeV, and then a gradual fall off at higher energies. No resonant behavior or striking deviations from smooth curves is evident. Although we have no explanation for the abnormally low point in the final state $\Sigma^- K^0 \pi^+$, we believe it represents some unexplained error rather than a legitimate effect.

The values of four-body lambda final states are characterized by a much gentler rise from threshold, and the maximum cross section for these states might not yet be reached at the highest momentum available to this experiment. Four-body sigma final states have relatively small cross sections (one fourth to one third of the four-body lambda cross sections) and are still rising at the highest momentum. Five-body cross sections are presented only at the two momenta for which data have been combined from several adjacent intervals to provide adequate statistics. Five-body final states with lambdas are produced more copiously than five-body sigma final states, and cross-sections are definitely still rising at 4.2 BeV/c.

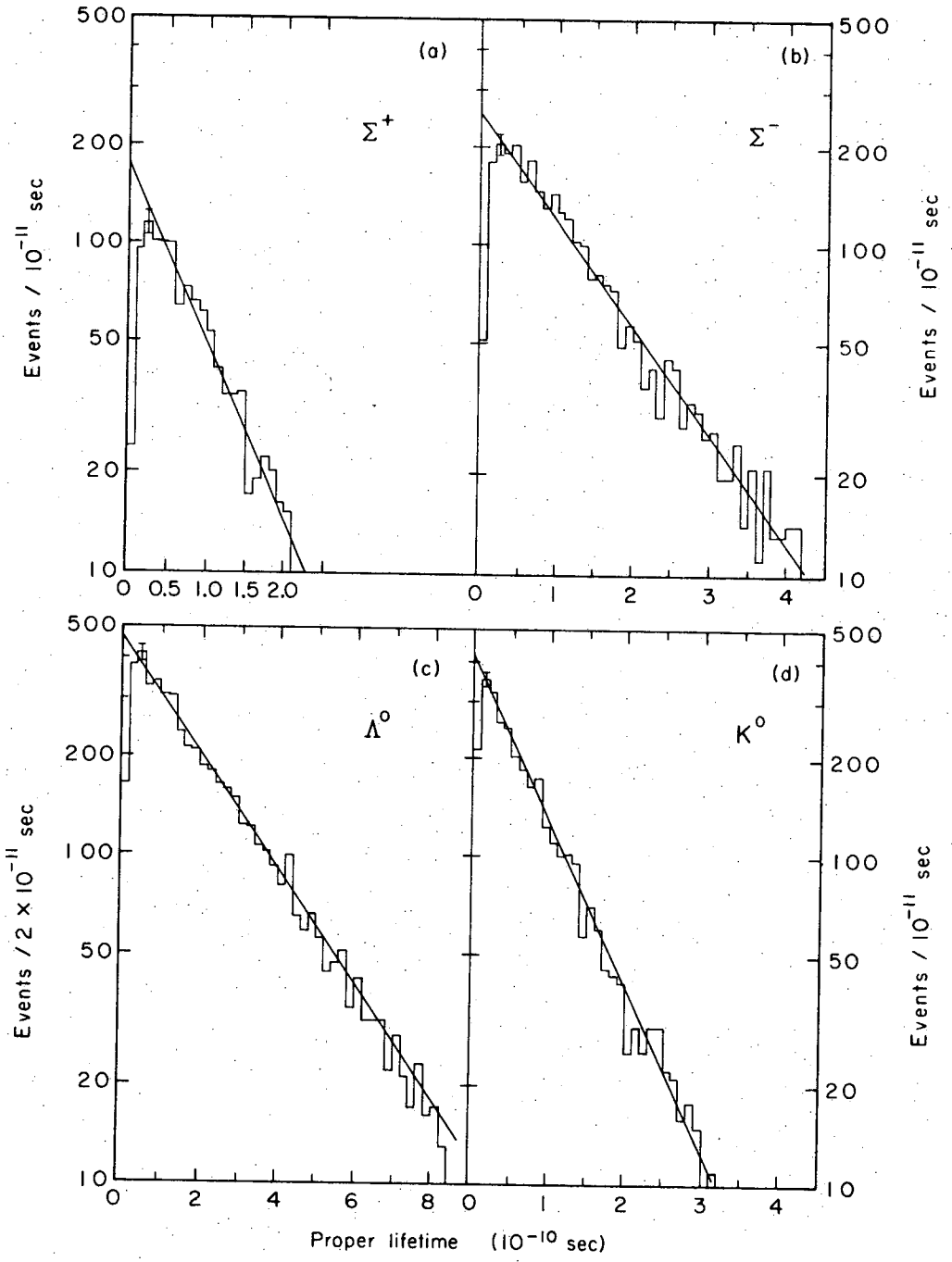

Fig. 7. Distribution of proper lifetime for Σ^+, Σ^-, Λ, and K^0 from this experiment. The fitted curves correspond to the mean lives (a) 0.794×10^{-10} sec, (b) 1.35×10^{-10} sec, (c) 2.61×10^{-10} sec, and (d) 0.881×10^{-10} sec.

Table VII. Three and four body strange-particle cross sections (μb).

Final state	Incident momentum (BeV/c)											
	1.590-1.640	1.915-1.960	1.960-2.015	2.015-2.080	2.080-2.190	2.580-2.630	2.825-2.895	2.960-3.065	3.065-3.175	3.175-3.245	3.840-3.930	4.130-4.190
$\Sigma^+K^0\pi^-$	17.2 ± 5.3	41.0 ± 6.6	44.4 ± 9.0	39.2 ± 5.6	33.2 ± 14.1	38.7 ± 7.0	36.9 ± 10.7	50.3 ± 8.8	47.1 ± 7.1	43.3 ± 5.0	41.7 ± 8.0	39.8 ± 7.1
$\Sigma^0K^+\pi^-$	13.8 ± 3.5	61.6 ± 7.0	56.0 ± 9.7	66.4 ± 6.9	63.3 ± 13.2	52.9 ± 7.8	56.1 ± 11.0	53.6 ± 7.8	46.2 ± 5.9	40.8 ± 4.0	43.0 ± 7.0	31.6 ± 5.2
$\Sigma^-K^+\pi^0$	13.2 ± 3.1	50.8 ± 5.8	49.6 ± 9.1	52.3 ± 5.7	43.5 ± 9.5	34.8 ± 5.0	26.5 ± 6.2	40.4 ± 6.0	28.8 ± 3.9	28.1 ± 2.9	33.8 ± 5.4	27.5 ± 4.1
$\Sigma^-K^0\pi^+$	21.8 ± 4.2	110.1 ± 9.0	100.3 ± 13.3	122.8 ± 9.4	110.3 ± 16.2	64.8 ± 6.9	72.5 ± 10.7	86.3 ± 9.1	68.5 ± 6.3	75.3 ± 5.1	60.1 ± 7.4	43.9 ± 5.2
$\Lambda K^+\pi^-$	86.1 ± 13.0	139.9 ± 13.2	143.2 ± 23.2	151.9 ± 14.1	115.9 ± 19.9	115.1 ± 13.2	138.1 ± 19.9	114.3 ± 13.7	97.0 ± 10.1	94.6 ± 7.7	99.3 ± 13.2	88.4 ± 10.7
$\Lambda K^0\pi^0$	91.4 ± 21.8	155.3 ± 25.9	163.4 ± 35.9	163.7 ± 25.8	88.4 ± 27.9	90.8 ± 18.2	128.1 ± 32.0	121.4 ± 24.0	75.7 ± 14.8	97.0 ± 14.8	97.5 ± 21.0	67.7 ± 14.8
$\Sigma^+K^+\pi^-\pi^-$	0 ± 0.93	0 ± 0.59	0 ± 0.95	3.2 ± 1.4	0 ± 2.7	7.5 ± 2.8	0 ± 2.8	13.8 ± 4.1	8.4 ± 2.6	16.2 ± 2.8	23.7 ± 5.8	24.5 ± 5.2
$\Sigma^+K^0\pi^0\pi^-$	0 ± 1.4	0 ± 1.4	0 ± 1.2	0 ± 1.1	0 ± 4.1	8.2 ± 3.8	17.8 ± 9.1	38.4 ± 10.3	22.7 ± 5.8	26.5 ± 4.7	33.7 ± 8.8	36.2 ± 8.2
$\Sigma^0K^0\pi^+\pi^-$	0 ± 2.0	0 ± 1.3	0 ± 2.2	3.9 ± 2.3	0 ± 5.9	9.9 ± 4.5	0 ± 5.5	40.8 ± 10.8	30.4 ± 7.9	17.3 ± 4.2	37.7 ± 10.6	45.6 ± 10.7
$\Sigma^-K^+\pi^+\pi^-$	0 ± 0.44	0 ± 0.27	0 ± 0.78	2.6 ± 0.82	4.2 ± 2.5	10.3 ± 2.2	18.3 ± 4.8	14.5 ± 2.9	17.1 ± 2.7	17.6 ± 2.0	20.4 ± 3.7	20.4 ± 3.4
$\Sigma^-K^0\pi^+\pi^0$	0 ± 1.4	0 ± 1.1	0 ± 1.2	1.7 ± 1.2	0 ± 3.9	11.5 ± 4.2	24.8 ± 10.4	29.4 ± 7.5	31.7 ± 6.9	29.5 ± 4.8	30.4 ± 7.7	54.6 ± 10.8
$\Lambda K^+\pi^0\pi^-$	1.38 ± 0.99	7.98 ± 2.0	10.1 ± 2.9	12.4 ± 2.4	10.5 ± 4.8	57.4 ± 7.9	65.2 ± 11.3	86.0 ± 11.1	74.2 ± 8.1	93.0 ± 7.5	102.8 ± 13.1	108.4 ± 12.3
$\Lambda K^0\pi^+\pi^-$	1.09 ± 0.89	9.92 ± 2.3	11.6 ± 3.1	21.9 ± 3.2	9.88 ± 5.1	59.2 ± 7.4	92.9 ± 14.5	112.9 ± 12.4	84.3 ± 8.4	104.4 ± 7.6	122.1 ± 13.8	95.8 ± 10.3

Table VIII. Five body strange-particle cross sections (μb).

Final state	Incident momentum (BeV/c) 2.9-3.3	3.8-4.2
$\Sigma^+K^+\pi^0\pi^-\pi^-$	1.69 ± 0.44	5.30 ± 1.2
$\Sigma^0K^+\pi^+\pi^-\pi^-$	2.17 ± 0.56	7.27 ± 1.6
$\Sigma^-K^+\pi^+\pi^0\pi^-$	5.50 ± 0.76	16.2 ± 2.2
$\Sigma^+K^0\pi^+\pi^-\pi^-$	0.84 ± 0.30	3.67 ± 0.99
$\Sigma^-K^0\pi^+\pi^+\pi^-$	2.88 ± 0.35	13.2 ± 2.0
$\Lambda K^+\pi^+\pi^-\pi^-$	10.1 ±1.3	29.5 ± 3.8
$\Lambda K^0\pi^+\pi^-\pi^0$	37.7 ± 5.0	69.9 ± 10.7

Results from both our experiment and other experiments are plotted in Figs. 8 and 9. (See also Ref. 20). In general, the various values agree well except for the channels $\Lambda K^+\pi^-$ and $\Sigma^0K^+\pi^-$. This discrepancy is probably due to the separation of these final states on the basis of confidence level alone in the other experiments; this criterion biases the $\Sigma^0K^+\pi^-$ final state high and the $\Lambda K^+\pi^-$ final state low relative to our values.

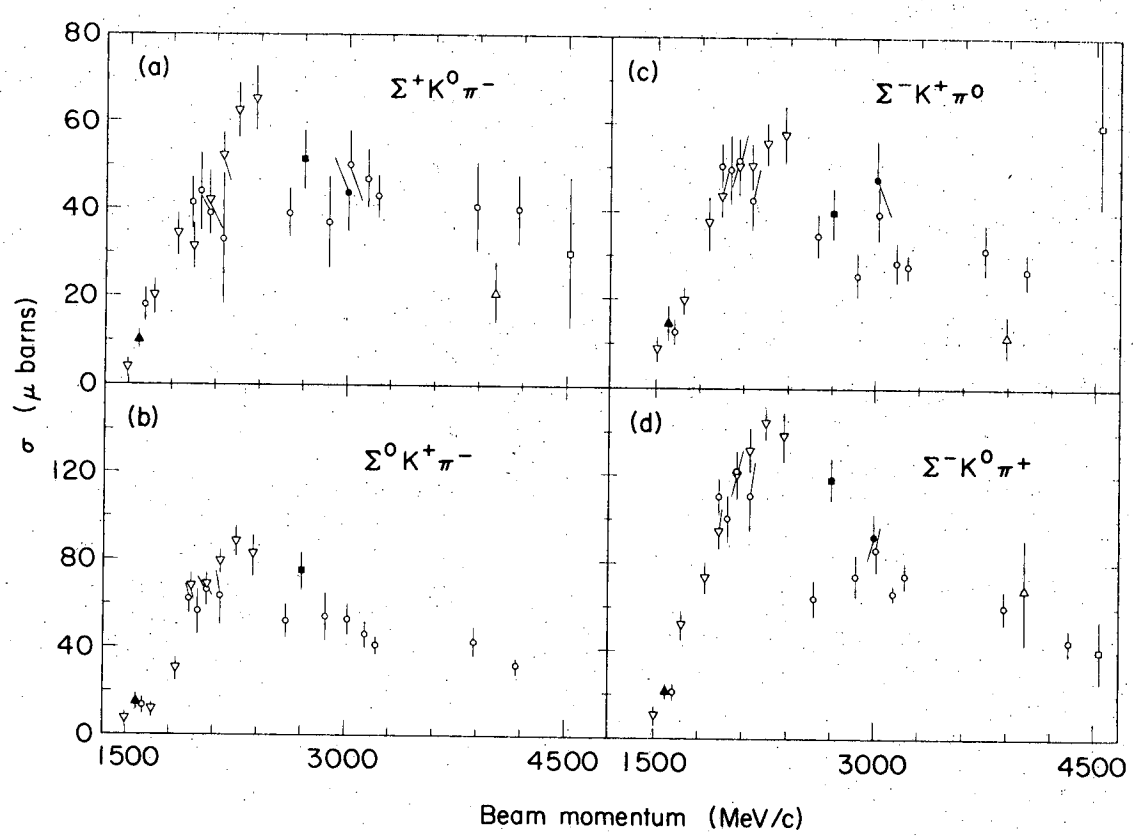

Fig. 8. Total cross sections as a function of incident momentum for $\Sigma K\pi$ final states.

- O This experiment
- ▲ European collaboration, Ref. 1
- ■ Purdue, Ref. 5
- ● Wisconsin, Ref. 6
- △ European collaboration, Ref. 7
- □ BNL, Ref. 8
- ▽ Berkeley, Ref. 20

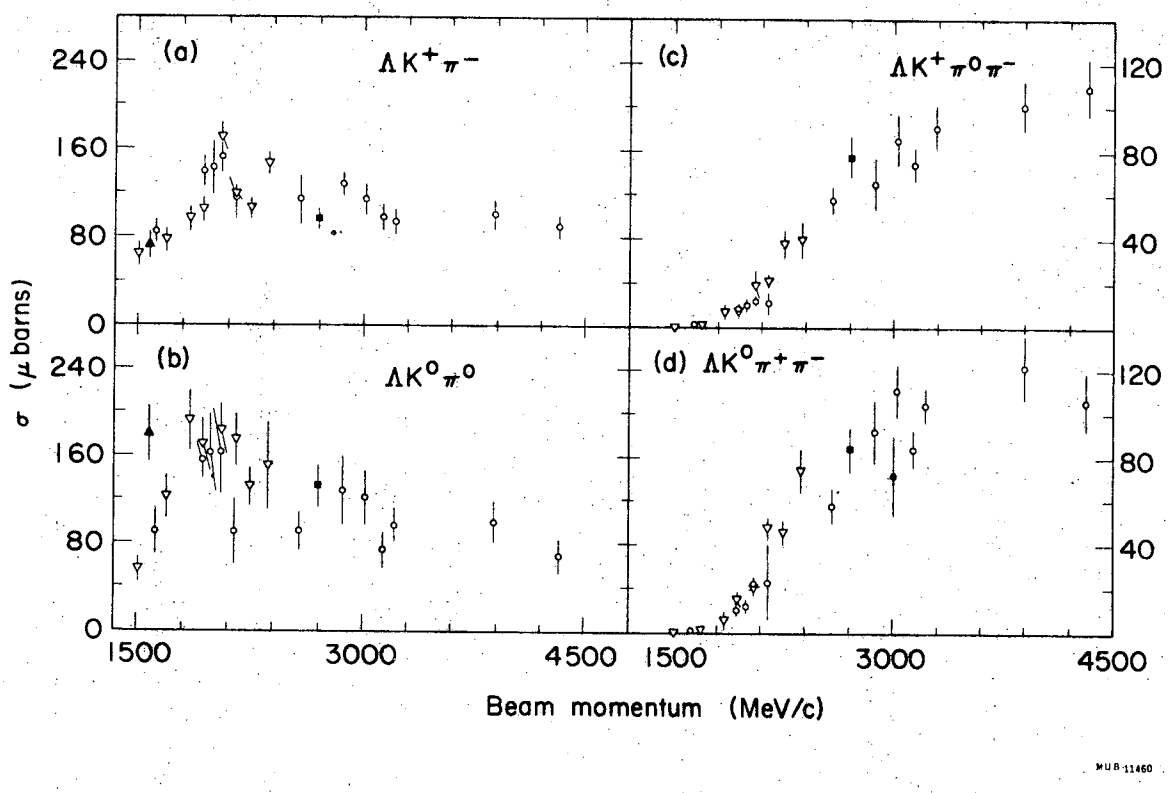

Fig. 9. Total cross sections as a function of incident momentum for $\Lambda K\pi$ and $\Lambda K\pi\pi$ final states.

- ○ This experiment
- ▲ European collaboration, Ref. 1
- ■ Purdue, Ref. 5
- ● Wisconsin, Ref. 7
- △ European collaboration, Ref. 7
- □ BNL, Ref. 8
- ▽ Berkeley, Ref. 20

IV. PROPERTIES OF RESONANT-STATE PRODUCTION

Strange-particle final states are dominated by resonance production in the momentum range covered by this experiment. Analysis of the effective-mass distributions for the existence of new states is complicated by the presence of well-established resonances which distort the predictions of unmodified phase space. To facilitate the analysis of the data, we investigated to what extent a simple phenomenological description of well-known resonance states could provide a satisfactory explanation for the distributions we observed.

We assumed that resonant processes could be represented by simple s-wave Breit-Wigner matrix elements, that all processes add incoherently, and that all resonant decays are isotropic in their respective centers of mass. Three ranges of incident pion momentum were selected for the analysis--1.8 to 2.2, 2.9 to 3.3, and 3.8 to 4.2 BeV/c; the relative strengths of each process were assumed constant over each of these intervals. These intervals will hereafter be referred to as I, II, and III, respectively.

Statistics in interval I were improved by the addition of events from an earlier $\pi^- p$ bubble chamber experiment colloquially called $\pi 72$. Several features of $\pi 72$ have been investigated and published earlier,[3,4] but the three- and four-body strange-particle final states have not been exhaustively examined. For the present analysis, events from the $\pi 72$ experiment were assigned to different final states on the basis of the same criteria as in the present experiment, as discussed in Sec. II. All subsequent analysis of interval I will include these events.

The values for the mass and width of each resonance, as well as the relative amounts, were fit by a maximum-likelihood program, SUPERFIT.[21] The variation in c.m. energy over each interval was taken into account by the program. Values for the mass and width for a given resonance, obtained from different final states and at different momenta, were consistent with one another. These values were averaged and the program rerun with only the relative amounts of processes allowed to vary. The averaged values for masses and widths used in the final runs are shown in Table IX, along with the fractional amounts of each process obtained. The experimental width of the K^{*+} is wider

than that of the K^{*0} because of the poorer resolution in $\Sigma^-(K\pi)^+$ final states. The difference in mass between charge states of the $Y^*(1385)$ and the $K^*(890)$ in the table are not to be interpreted as the results of a serious attempt to measure these quantities. No effort was made to carefully investigate systematic differences among the various channels producing these states. Such investigations are more fruitfully carried out in final states from other reactions. The data should be viewed rather as empirical values that best describe the presence of resonant processes in our data.

The values obtained for cross sections of resonant processes are shown in Table X.

Using the relative amounts for each process determined from the fit, we calculated the effective-mass distributions expected from these effects. The variation in incident momentum was taken into account by dividing each interval into eight subintervals, computing the distributions for each, and summing them properly weighted by the numbers of events in the subintervals. Effective-mass projections of the data and the calculated distributions are shown in Figs. 10 through 15 and 26 through 29. In some distributions, reflections of resonant processes produce considerable deviations of the curves from nonresonant phase space. Also shown in Figs. 10 through 15 are the Dalitz plots for each of the six three-body final states, with the effective mass squared of the $K\pi$ plotted as ordinate and the effective mass squared of the $Y\pi$ as abscissa, Columns I, II, and III are for events in intervals I, II, and III, respectively. Effective-mass distributions for ΛK, $\Lambda K\pi$, and $\pi\pi$ from four-body lambda final states are not presented, as no deviations from the calculated distributions were found for these projections. The masses, widths, and percentages of resonances for $\Sigma K\pi\pi$ final states were not fit because of the small number of events in each channel.

The following conventions are used for the presentation of all angular distributions. We define the four vectors $\underset{\sim}{P}_1$, $\underset{\sim}{P}_2$, $\underset{\sim}{P}_3$, and $\underset{\sim}{P}_4$ as the momenta of the beam, target, meson resonance (meson), and baryon (baryon resonance), respectively. The production normal is given by $\underset{\sim}{n} = (\underset{\sim}{P}_1 \times \underset{\sim}{P}_3) = (\underset{\sim}{P}_2 \times \underset{\sim}{P}_4)$ evaluated in the overall center of mass.

Table IX. Properties of resonance production.

(a) Averaged values for masses and widths of resonances.

Resonance	Mass (MeV)	Width (MeV)
$Y^*(1405)$	1386 ± 2.4	53 ± 4.4
$Y^*(1520)$	1517 ± 1.6	18 ± 2.9
$Y^{*0}(1385)$	1380 ± 2.6	43 ± 5.0
$Y^*(1385)$	1385 ± 1.6	41 ± 4.3
$K^{*+}(890)$	885 ± 2.1	51 ± 5.5
$K^{*0}(890)$	891 ± 0.9	44 ± 2.1
$K^{*0}(1440)$	1446 ± 7.9	61 ± 24

(b) Relative strengths of resonant processes from maximum-likelihood fit for three-body final states.

Final state	Momentum interval	Resonance				
		$Y^*(1405)$	$Y^*(1520)$	$Y^*(1385)$	$K^*(890)$	$K^{*0}(1440)$
$\Sigma^+K^0\pi^-$	I	0.42 ± 0.04	0.17 ± 0.03			
	II	0.29 ± 0.03	0.14 ± 0.03			
	III	0.28 ± 0.06	0.11 ± 0.04			
$\Sigma^0K^+\pi^-$	I				0.56 ± 0.03	
	II				0.54 ± 0.04	
	III				0.42 ± 0.06	
$\Sigma^-K^+\pi^0$	I				0.29 ± 0.03	
	II				0.24 ± 0.04	
	III				0.08 ± 0.04	
$\Sigma^-K^0\pi^+$	I	0.19 ± 0.02	0.08 ± 0.01		0.29 ± 0.03	
	II	0.13 ± 0.02	0.05 ± 0.02		0.21 ± 0.03	
	III	0.18 ± 0.03	0.09 ± 0.03		0.12 ± 0.03	
$\Lambda K^+\pi^-$	I			0.31 ± 0.02	0.49 ± 0.02	
	II			0.05 ± 0.01	0.43 ± 0.03	
	III			0.02 ± 0.02	0.48 ± 0.04	0.17 ± 0.04
$\Lambda K^0\pi^0$	I			0.41 ± 0.04	0.17 ± 0.04	
	II			0.29 ± 0.06	0.20 ± 0.04	
	III			0.16 ± 0.06	0.19 ± 0.06	

(c) Relative strengths of resonant processes from maximum-likelihood fit for $\Lambda K\pi\pi$ final states.

Final state	Momentum interval	Resonance							
		$Y^{*+}(1385)$	$Y^{*0}(1385)$	$Y^{*-}(1385)$	$K^{*0}(890)$	$K^{*+}(890)$	$Y^{*0}K^{*0}$	$Y^{*-}K^{*+}$	$Y^*(1520)$
$\Lambda K^+\pi^0\pi^-$	II		0.12 ± 0.03	0.06 ± 0.03	0.16 ± 0.03	0.11 ± 0.03	0.18 ± 0.03	0.06 ± 0.02	
	III		0.08 ± 0.03	0.12 ± 0.03	0.17 ± 0.04	0.08 ± 0.03	0.14 ± 0.03		
$\Lambda K^0\pi^+\pi^-$	II	0.15 ± 0.02		0.16 ± 0.03		0.11 ± 0.03		0.10 ± 0.03	0.03 ± 0.01
	III	0.11 ± 0.03		0.10 ± 0.03		0.11 ± 0.04			0.02 ± 0.01

Table X. Resonant-state cross sections (μb).

Final state	Momentum interval (BeV/c)		
	1.8 - 2.2	2.9 - 3.3	3.8 - 4.2
$Y^{*0}(1405)K^0$	51.0 ± 4.7	37.4 ± 3.7	30.3 ± 4.6
$Y^{*0}(1520)K^0(\Sigma\pi)$	23.7 ± 2.7	18.7 ± 2.1	14.0 ± 3.6
$Y^{*0}(1520)K^0(\Lambda\pi\pi)$	2.8 ± 1.0	4.4 ± 1.5	2.9 ± 1.6
$\Sigma^0K^{*0}(890)$	49.4 ± 4.4	36.4 ± 3.8	23.1 ± 4.3
$\Sigma^-K^{*+}(890)$	45.3 ± 3.2	23.1 ± 2.7	8.8 ± 2.1
$\Lambda K^{*0}(890)$	98.4 ± 7.4	63.0 ± 5.6	63.1 ± 7.7
$Y^{*-}(1385)K^+$	42.8 ± 4.0	5.0 ± 1.0	0 ± 1.9
$Y^{*0}(1385)K^0$	61.6 ± 10.0	28.9 ± 7.0	13.0 ± 5.4
$\Lambda K^{*0}(1440)$			23.9 ± 6.0
$Y^{*+}(1385)K^0\pi^-$	2.9 ± 1.1	15.1 ± 2.2	11.9 ± 3.4
$Y^{*-}(1385)K^0\pi^+$	0 ± 1.1	16.1 ± 3.2	10.8 ± 3.4
$Y^{*-}(1385)K^{*+}(890)$	11.9 ± 2.0	15.0 ± 4.5	0 ± 1.1
$Y^{*-}(1385)K^+\pi^0$	0 ± 1.1	5.5 ± 2.8	13.5 ± 3.6
$K^{*+}(890)\Lambda\pi^-$	0 ± 1.1	19.8 ± 4.0	20.4 ± 5.6
$Y^{*0}(1385)K^+\pi^-$	1.3 ± 1.5	11.0 ± 2.9	9.0 ± 3.5
$Y^{*0}(1385)K^{*0}(890)$	6.8 ± 2.4	24.8 ± 4.5	23.6 ± 5.6
$K^{*0}(890)\Lambda\pi^0$	0 ± 1.6	22.0 ± 4.4	28.6 ± 7.3
$Y^{*0}(1405)K^{*0}(890)$		13 ± 2	16 ± 3
$Y^{*0}(1520)K^{*0}(890)$		7 ± 1	6 ± 1
$Y^{*0}(1660)K^{*0}(890)$		3 ± 1	3 ± 1

In the rest frame of a meson resonance (meson), we use the coordinate system defined by $(\hat{X}, \hat{Y}, \hat{Z}) = (\widehat{n \times P_1}, \hat{n}, \hat{P}_1)$, and in the rest frame of a baryon (baryon resonance) the coordinate system defined by $(\hat{X}, \hat{Y}, \hat{Z}) = (\widehat{n \times P_2}, \hat{n}, \hat{P}_2)$. The angles θ and ϕ are the usual spherical coordinates with $\phi = 0$ along the x axis. Defined in this way, ϕ is the usual Treiman-Yang angle. For baryon decays we measure the angles for the final-state nucleon relative to the coordinate system we have defined. For weak decays we choose our conventions so that the decay of a spin projection $m_z = +1/2$ would yield for the decay distribution for the nucleon of $1 + \alpha \cos\theta$, where α is the decay asymmetry parameter. With these conventions, $\alpha = +0.66$ for lambda decay. Production angular distributions are calculated in the overall center of mass with $\cos\alpha \equiv \hat{P}_1 \cdot \hat{P}_3$ for meson resonances (mesons) and $\cos\alpha \equiv \hat{P}_2 \cdot \hat{P}_4$ for baryons (baryon resonances). Defined in this way, both peripherially produced meson and baryon states will have $\cos\alpha = +1$. Weighted events are used for all angular distributions. Where specified, angular distributions for events in some resonance interval of effective mass were modified to compensate for the presence of nonresonant background effects. We assume that nonresonant processes contribute incoherently and that their characteristics change slowly over the spectrum of effective mass of interest. Distributions from "control" regions of effective mass to either side of a resonance properly normalized to the number of background events estimated to be present in the resonant region, were subtracted from the distributions in the resonant regions to obtain the plots shown in Figs. 17 and 19 through 21. The unweighted number of events in each final state in each interval are shown in Figs. 10 through 15.

A. Three-Body Final States

1. $Y^*(1405)$

For the three-body final states in general, the fits are good and the data are quite well explained by the resonant states obviously present. The poorest fits are to the $Y_0^*(1405)$ in both the $\Sigma^+\pi^-$ and $\Sigma^-\pi^+$ channels. The asymmetric nature of the peak with the rapid falloff of events on the high side is not well fitted by the Breit-Wigner shape. (The best fit gives

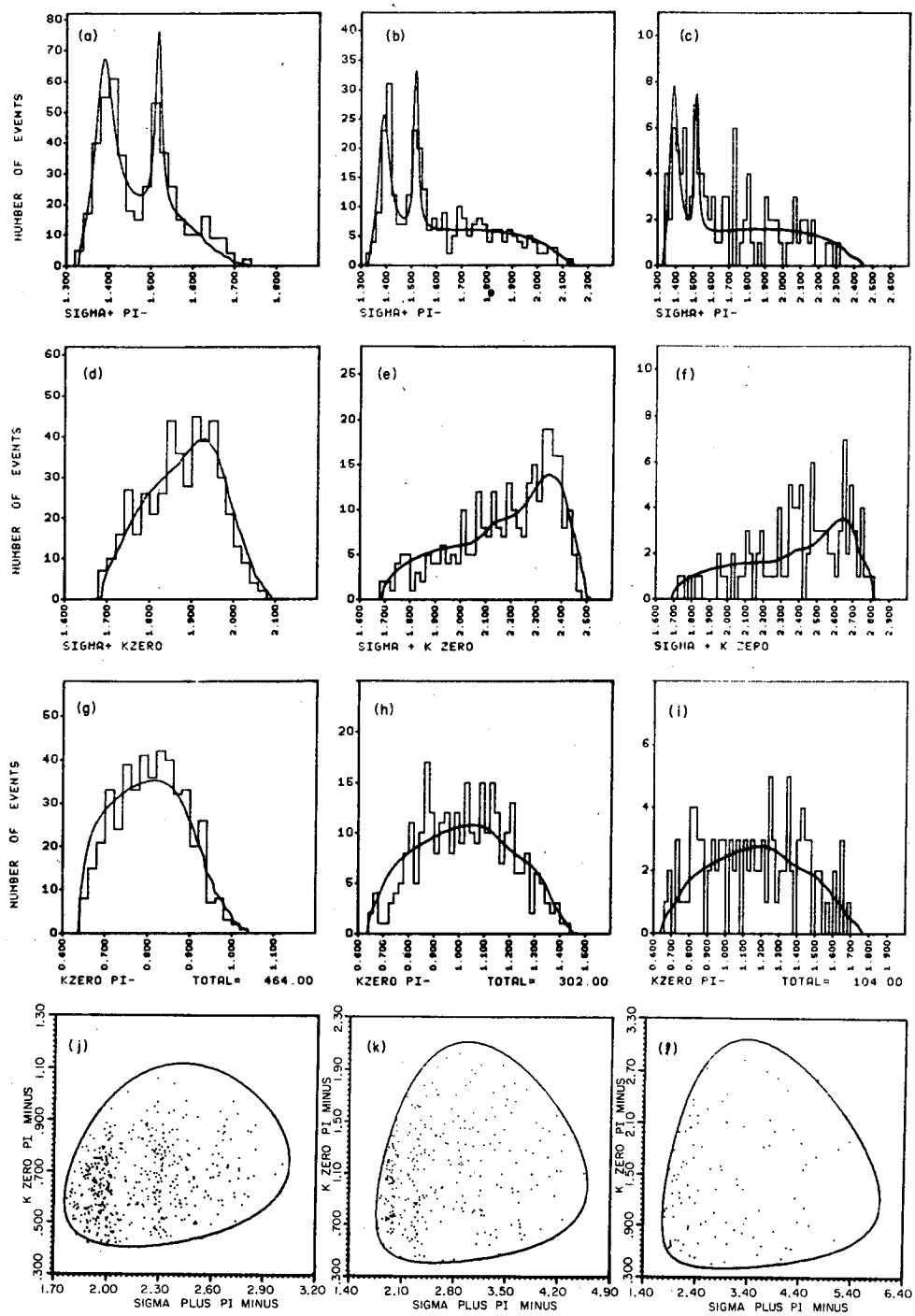
(a)
(b)
(c)
NUMBER OF EVENTS
SIGMA+ PI-
(d)
(e)
(f)
SIGMA+ KZERO
SIGMA + K ZERO
(g)
(h)
(i)
KZERO PI-
TOTAL= 464.00
TOTAL= 302.00
TOTAL= 104.00
(j)
(k)
(l)
K ZERO PI MINUS
SIGMA PLUS PI MINUS

Fig. 10

Fig. 10. Effective-mass projections and Dalitz plots for the final state $\Sigma^+ K^0 \pi^-$. The abscissa for the projections is in units of BeV, and the coordinates for the Dalitz plots in $(\mathrm{BeV})^2$. The curves were calculated with the fraction of resonant processes shown in Table IX.

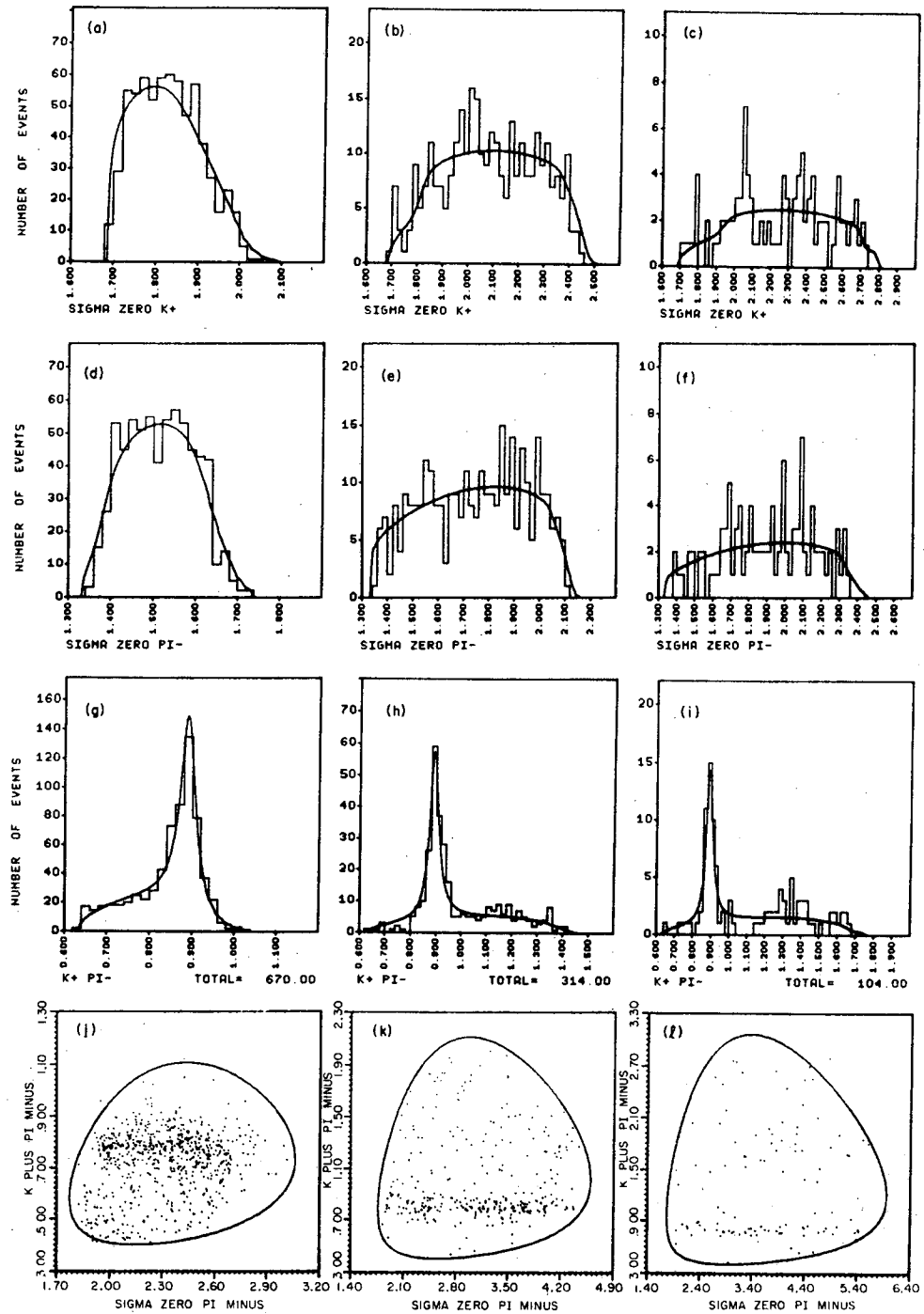

Fig. 11. Effective-mass projections and Dalitz plots for the final state $\Sigma^0 K^+ \pi^-$. The abscissa for the projections is in units of BeV, and the coordinates for the Dalitz plots in $(\mathrm{BeV})^2$. The curves were calculated with the fraction of resonant processes shown in Table IX.

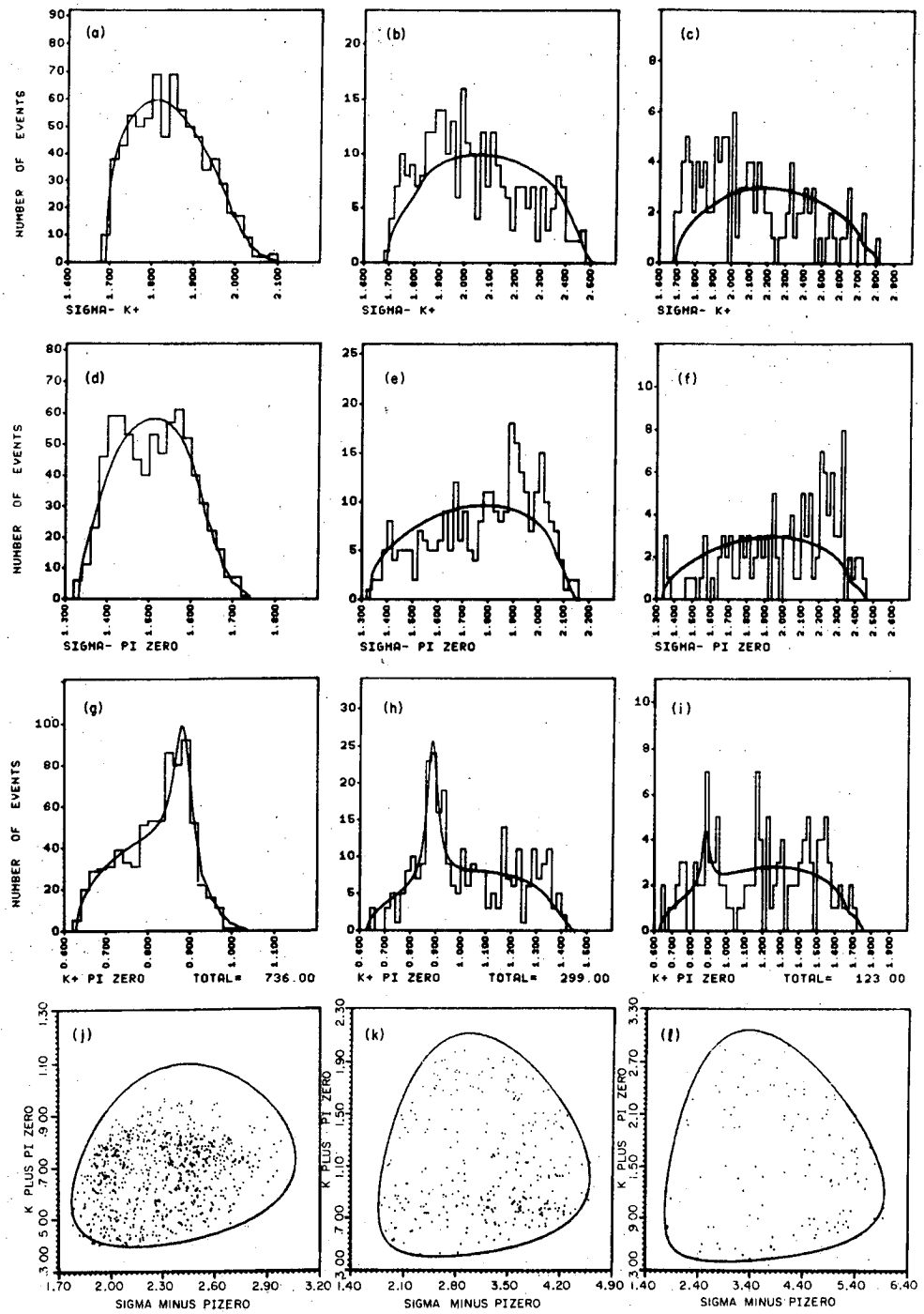

Fig. 12. Effective-mass projections and Dalitz plots for the final state $\Sigma^- K^+ \pi^0$. The abscissa for the projections is in units of BeV, and the coordinates for the Dalitz plots in $(\mathrm{BeV})^2$. The curves were calculated with the fraction of resonant processes shown in Table IX.

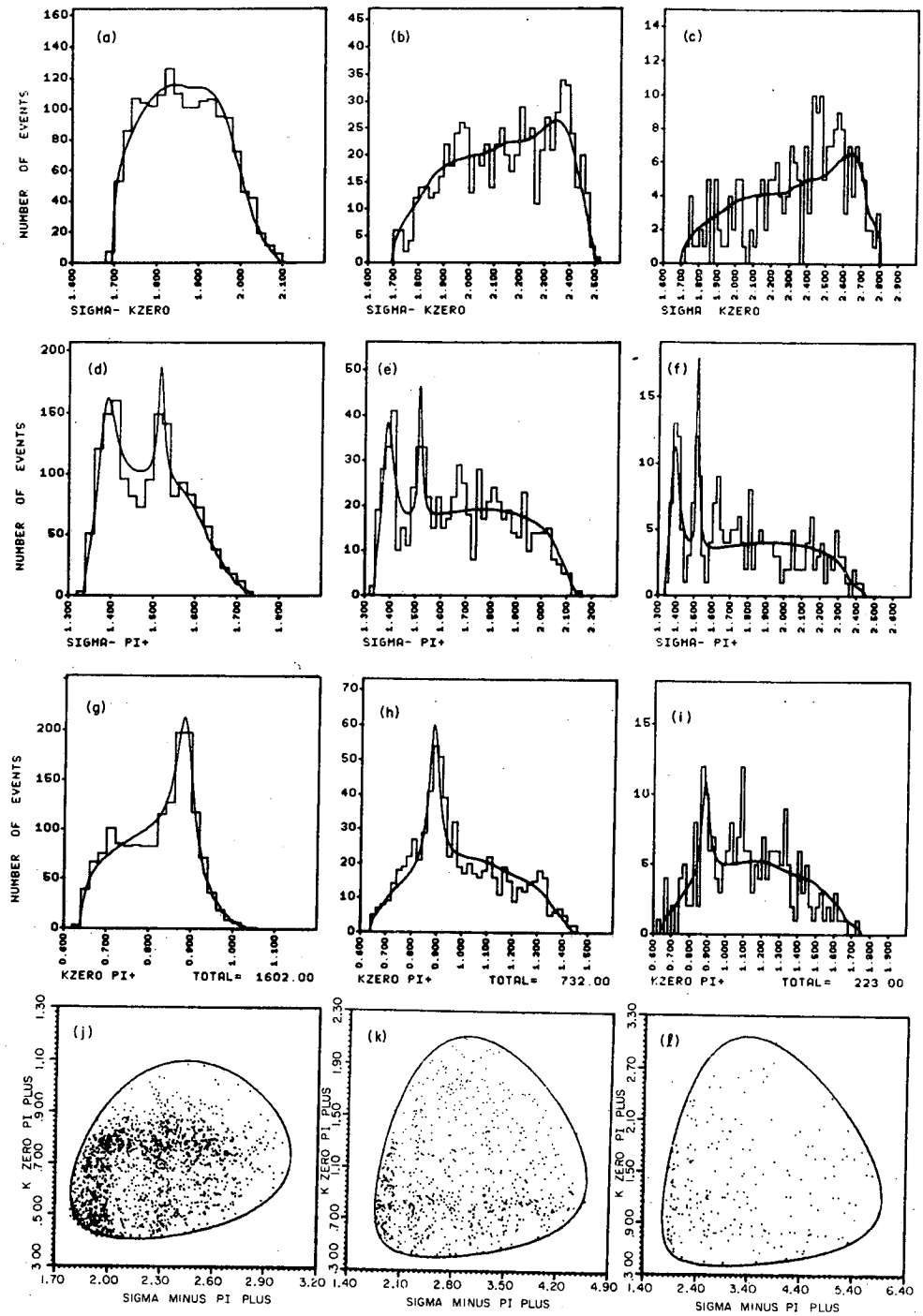

Fig. 13. Effective-mass projections and Dalitz plots for the final state $\Sigma^- K^0 \pi^+$. The abscissa for the projections is in units of BeV, and the coordinates for the Dalitz plots in $(\mathrm{BeV})^2$. The curves were calculated with the fraction of resonant processes shown in Table IX.

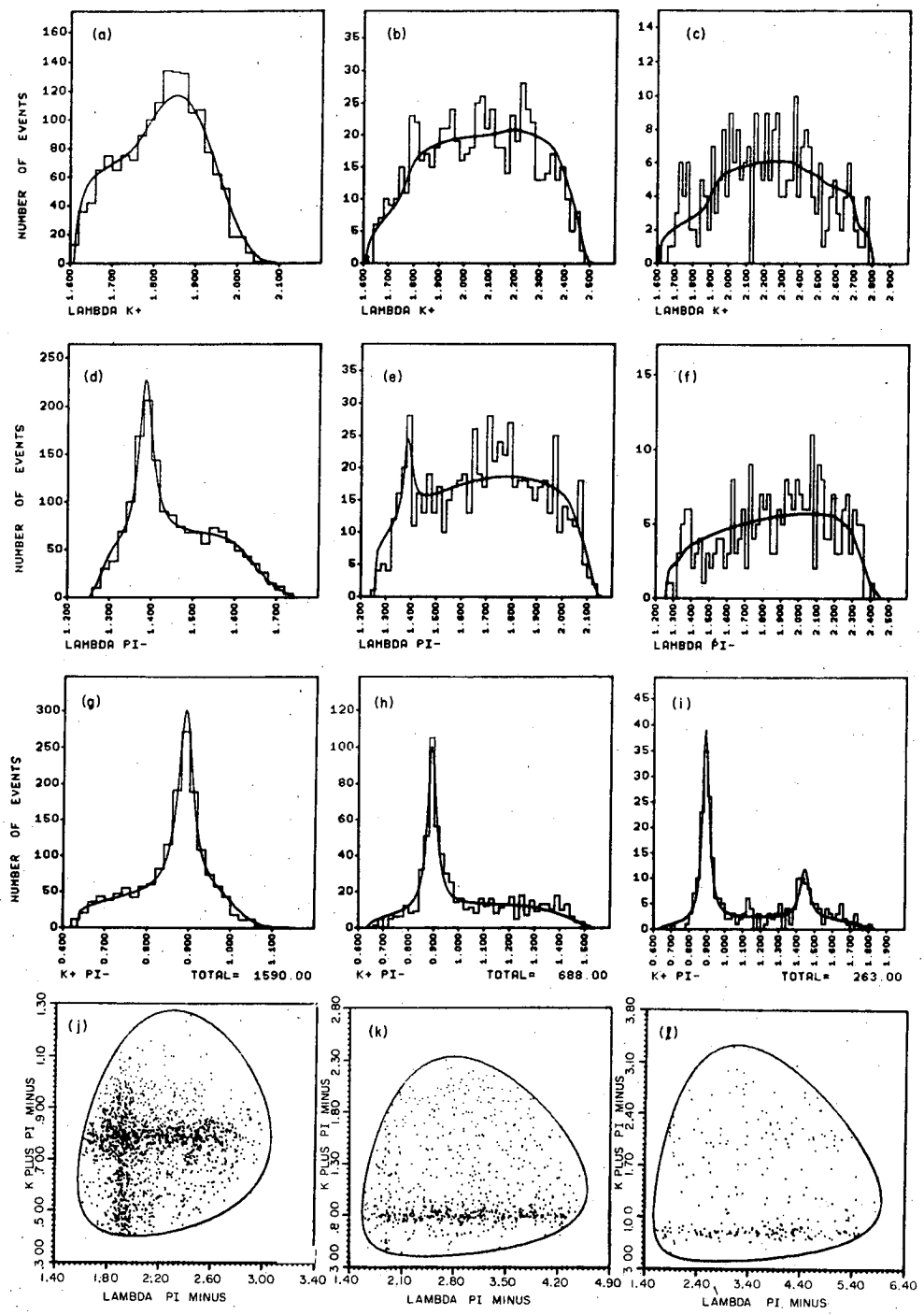

Fig. 14. Effective-mass projections and Dalitz plots for the final state $\Lambda K^+\pi^-$. The abscissa for the projections is in units of BeV, and the coordinates for the Dalitz plots in $(\mathrm{BeV})^2$. The curves were calculated with the fraction of resonant processes shown in Table IX.

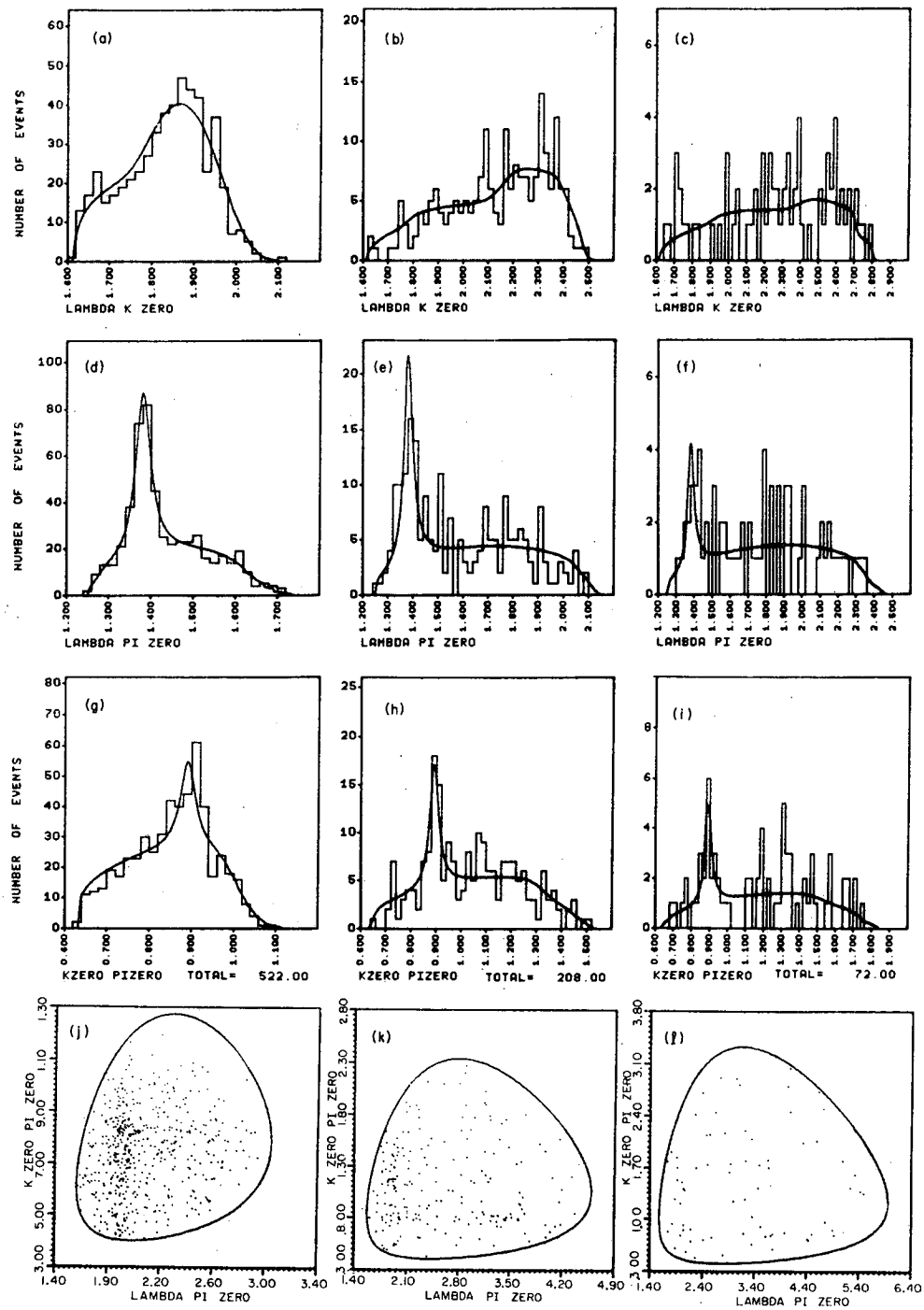

Fig. 15. Effective-mass projections and Dalitz plots for the final state $\Lambda K^0 \pi^0$. The abscissa for the projections is in units of BeV, and the coordinates for the Dalitz plots in $(\mathrm{BeV})^2$. The curves were calculated with the fraction of resonant processes shown in Table IX.

a central value of 1.387 for the resonance since the s-wave Breit-Wigner is a symmetric form about the central value.) These distributions are much better explained by the interpretation of the $Y_0^*(1405)$ as a $\bar{K}$-n s-wave bound state. The K-matrix formalism of Dalitz and Tuan,[22] as applied by Alexander et al.,[3] adequately describes the behavior of the data with a three-parameter fit. The decay distribution of the Σ^+ from $Y_0^*(1405)$ in the final states $\Sigma^+K^0\pi^-$ and $\Sigma^-K^0\pi^+$ in interval I is shown in Fig. 16. The distributions are consistent with the s-wave bound-state interpretation for this effect. Although interval I is not far from threshold for the reaction $\pi^-p \rightarrow Y^*K$, the differential cross section for $Y_0^*(1405)$ production is very peripheral. Corresponding plots for $Y_0^*(1520)$ and $Y^{*0}(1385)$ in Fig. 17 also show forward peaking but it is not nearly so severe as for the $Y_0^*(1405)$. If one accepts the view that absorptive effects are primarily responsible for the observed differential cross-section distributions, then these data imply that final-state Y^*K inelastic scattering is stronger for the $Y^*(1405)$ than for the other two states.

Rather than use the Breit-Wigner fitted values for the cross sections for $Y^*(1405)K^0$, we estimated the number of events above smooth backgrounds and used them in the calculations. The branching ratio into the states $\Sigma^+\pi^-$ and $\Sigma^-\pi^+$ is consistent with unity. The exact form of this resonant peak has little effect on the other projections for the final states $\Sigma^+K^0\pi^-$ and $\Sigma^-K^0\pi^+$.

2. $Y^*(1520)$

Besides decaying into $\Sigma^+\pi^-$ and $\Sigma^-\pi^+$, the state $Y_0^*(1520)$ also decays into $\Lambda\pi^+\pi^-$ and NK^*.[13] The number of events above background in each channel was estimated and branching ratios were computed. The results are shown in Table XI. The values we obtain are not consistent with those that Watson et al.[23] obtained from the reaction $K^-p \rightarrow Y^*(1520) \rightarrow$ decay products. Tripp[24] reports, however, that more data are being collected for this process and that his values will probably be more consistent with ours.

The production and decay angular distributions for the $Y^*(1520)$ from the final state $\Sigma^+K^0\pi^-$ are presented in Fig. 17. Events from

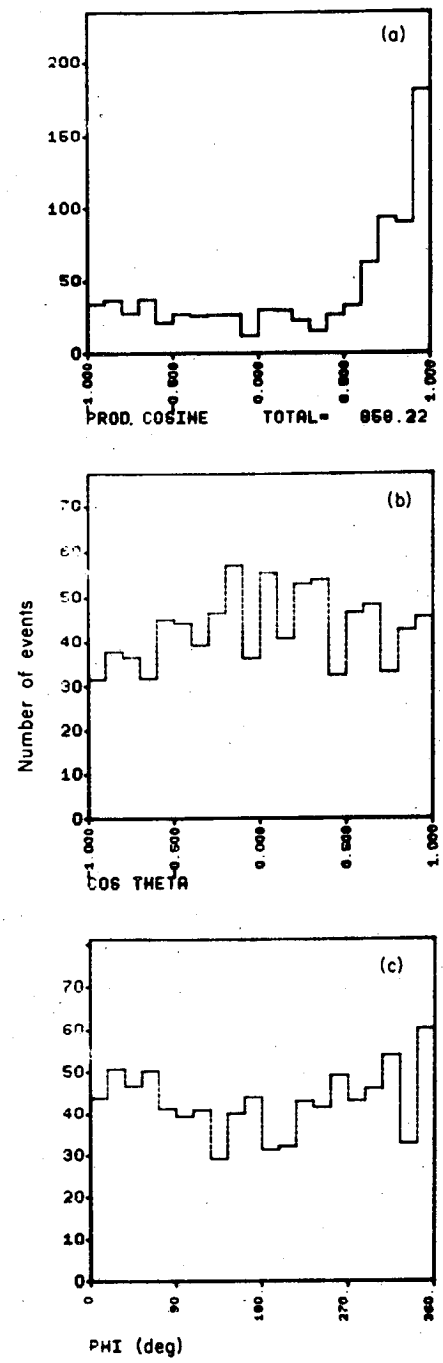

Fig. 16. Angular distributions for the $Y^*(1405)$ from $\Sigma^+K^0\pi^-$ and $\Sigma^-K^0\pi^+$ in interval I. $\cos\theta$ and ϕ are defined on page 43.

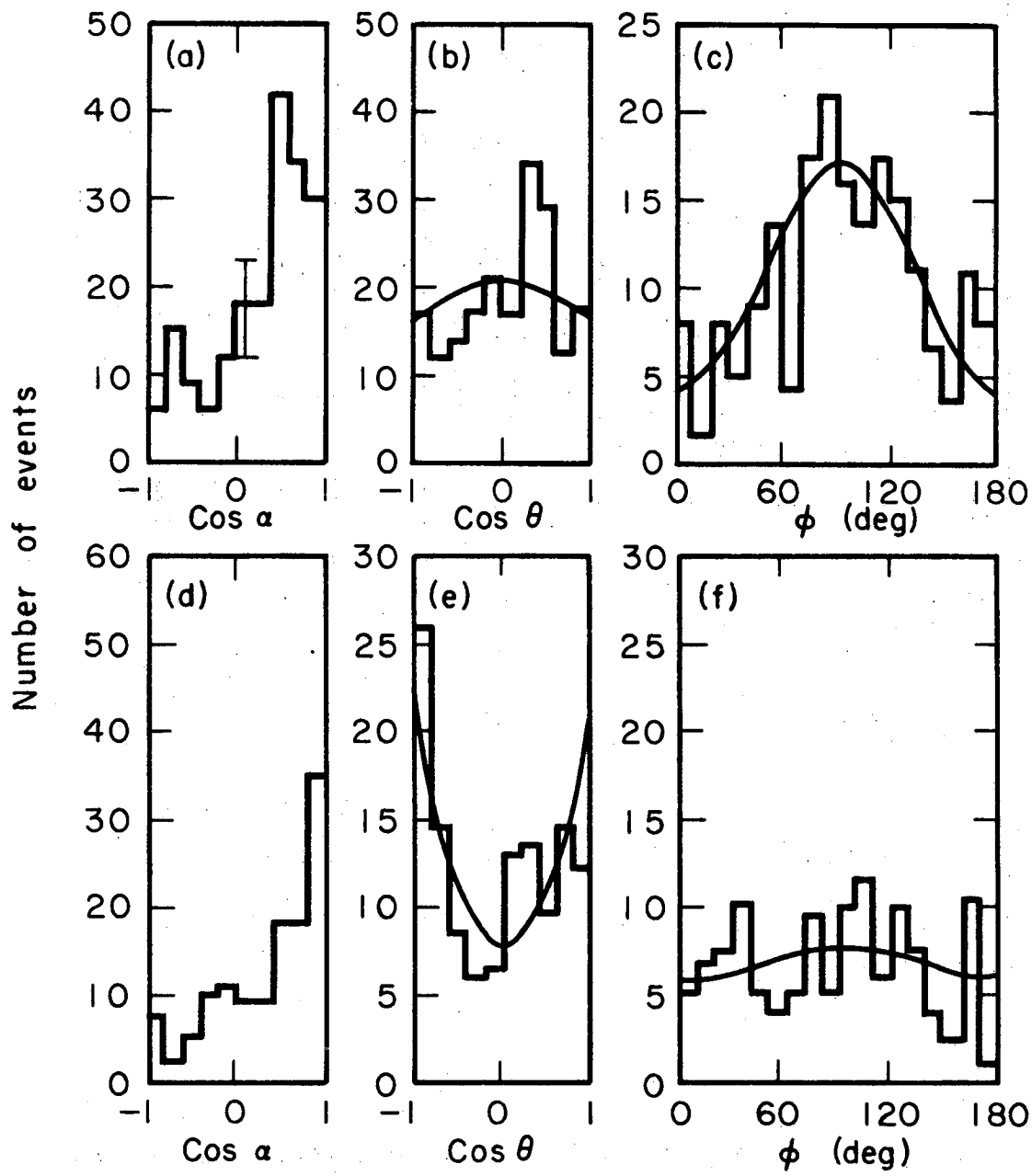

Fig. 17. Angular distributions (a), (b), and (c) for $Y^{*0}(1385)$ from $\Lambda K^0\pi^0$ in interval I, (d), (e), and (f) for $Y^{*0}(1520)$ from $\Sigma^+K^0\pi$ in interval I. $\cos\alpha$, $\cos\theta$, ϕ are defined on page 43.

Table XI. Branching ratios for $Y_0^*(1520)$.

Mode	Fraction
$\Sigma\pi$	0.45 ± 0.04
$\Lambda\pi^+\pi^-$	0.08 ± 0.02
NK^*	0.47 ± 0.09

Total cross section for $\pi^- p \rightarrow Y_0^*(1520) K^0$

Incident momentum	1.8 - 2.2	2.9 - 3.3	3.8 - 4.2
Cross section	49 ± 6	47 ± 7	28 ± 7

$\Sigma^- K^0 \pi^+$ were not used because of the K^* formation in that final state. No background subtraction was done because the entire $\Sigma\pi$ spectrum is blanketed with resonant-state formation and we could not choose a statistically significant selection of events that represent the nonresonant background. The background events constitute about 30% of the sample.

The decay distribution in θ and ϕ have been fit with weighted events and a maximum-likelihood method to the density matrix parameters appropriate for the strong decay of a 3/2 state. (The density matrix formalism is discussed in Appendix A.) The values obtained and the selection criteria for the events are presented in Table XII. Fitted angular distributions are shown in Fig. 17. The correlation with the beam direction exhibits a $\cos^2\theta$ character, with possibly some s-wave interference, and the ϕ distribution is reasonably flat.

Because the process $\pi^- p \rightarrow Y^* K$ cannot proceed through single-K exchange, the lowest mass assignment for the exchange particle is the K^*. For such a process the pK^*Y^* vertex is characterized by three independent coupling constants. Stodolsky and Sakurai[25-26] reduce this freedom to one parameter by proposing the "ρ-photon" analogy, which in essence is that the vector-exchange particle couples to the baryon vertex in much the same way as does a photon in reactions such as $\gamma + N \rightarrow N^*$. If one assumes further that a single multipole transition

Table XII. Selection criteria and density matrix parameters for $\pi p \rightarrow Y^{*}K$.

Final state	Mass interval (BeV)	Production angle	Incident momentum (BeV/c)	ρ_{33}		$\mathrm{Re}\,\rho_{31}$		$\mathrm{Re}\,\rho_{3-1}$	
$Y^{*0}(1520)K^0 \rightarrow \Sigma^+\pi^-$	1.493 - 1.537	-1.0 - 1.0	1.8 - 2.2	0.073	0.052	0.057	0.043	0.039	0.050
$Y^{*0}(1385)K^0 \rightarrow \Lambda\pi^0$	1.350 - 1.410	-1.0 - 1.0	1.8 - 2.2	0.285	0.048	-0.104	0.043	0.262	0.041

dominates the process, one can predict specific decay distributions for the baryon resonance. The predictions for $3/2^+$ and $3/2^-$ states expressed in terms of density matrix parameters are shown in Table XIII. Our data favor the longitudinal dipole transition for $Y^*(1520)$ production.

Table XIII. Predictions for density matrix parameters of $3/2^+$ and $3/2^-$ states for various multipole interactions.

Resonant state	J^P	Interaction	ρ_{33}	Re ρ_{3-1}	Re ρ_{31}
$Y^{*0}(1385)$	$3/2^+$	M_1	3/8	$\sqrt{3}/8 = 0.216$	0
		E_2	1/8	$-\sqrt{3}/8$	0
		L_2	0	0	0
$Y^{*0}(1520)$	$3/2^-$	M_2	1/8	$\sqrt{3}/8$	0
		E_1	3/8	$-\sqrt{3}/8$	0
		L_1	0	0	0

The production angular distribution for this state shows the characteristics of peripheral production.

3. $Y_1^*(1660)$

The high-mass end of interval I is just at threshold for the production of $Y^*(1660)$, and there is no strong evidence for its production in the final states $\Sigma^+\pi^-$ and $\Sigma^-\pi^+$. The likelihood-function fit to these final states was insensitive to the amount of this resonance present, however, and no quantitative value was obtained. Examination of data from the $\pi 72$ experiment with incident momentum between 2.2 and 2.4 BeV/c showed a peak at 1660 MeV. The cross section for $\pi^- p \rightarrow Y_0^*(1660)K^0$ at 2.3 BeV/c was estimated to be $\approx 12\ \mu b$ from that experiment. No strong evidence exists for the production of $Y^*(1660)$ in intervals II and III in three-body final states.

4. $Y^*(1385)$

Both the Y^{*0} and Y^{*-} are strongly produced in three-body final states in interval I. At higher momenta the production of Y^{*0} falls off significantly and the Y^{*-} is virtually nonexistent.

Production and decay angular distributions for the Y^{*0} are presented in Fig. 17. A background subtraction was performed on the data.

The model of the ρ-photon analogy is also applicable to $Y^*(1385)$ production. For this case the model, in addition to prescribing the form of the decay angular distribution for the three possible dominant multipoles, selects the magnetic dipole transition in particular. The process $\gamma + N \rightarrow N^*(1238)$ seems to proceed via this process, and the analogy predicts the same for ρ exchange in $\pi^- p \rightarrow N^* \pi$. Since the ρ and K^* are in the same SU_3 multiplet, one expects K^* exchange to behave in the same way also. Our experimental determination of density matrix parameters from subtracted weighted events are presented in Table XII and the theoretical predictions in Table XIII. The agreement is best for the magnetic dipole transition but the fit could be much better.

For the magnetic dipole transition, the production differential cross section should vanish in both the forward and backward directions. Our data instead show the characteristic forward-peaked distribution.

Analysis of the Y^{*-} state is extremely difficult in this experiment. The rapid decrease in cross section limits investigation to interval I. Here we are faced with untangling the effects of the Y^* and the strongly produced $K^{*0}(890)$. Decay angular distributions are critically influenced by the presence of the other resonance. In the case of the Y^{*0}, we were able to make subtractions that yielded physically tenable distributions. But for the Y^{*-} and K^{*0} we were unable to do so.

5. $Y_0^*(1660)$

Production of I = 0 resonant hyperon states could well be obscured in this experiment by the presence of I = 1 amplitudes in the channels $\Sigma^+\pi^-$ and $\Sigma^-\pi^+$. To investigate the possible existence of these states, we have plotted the effective mass of lambda and missing mass from the ΛK^0mm final state. The events are predominately from the reactions

$\pi^- p \to \Sigma^0 K^0 \pi^0$ and $\pi^- p \to \Lambda K^0 \pi^0 \pi^0$. In each instance, the isotopic spin of the lambda and missing mass ($\Sigma^0 \pi^0$ or $\Lambda \pi^0 \pi^0$) must be equal to zero or two. In Fig. 18 where we have combined the data from all momenta, we see clear evidence for the production of the I = 0 states $Y^*(1405)$ and $Y^*(1520)$, but no strong indication of any other resonant phenomena. In particular, we see no evidence for the proposed $Y_0^*(1660)$ to complete the hypothesized octet of $3/2^-$ particles to be composed also of $N_{1/2}^*(1518)$, $\Xi^*(1816)$, and $Y_1^*(1660)$.

6. $K^*(890)$

Both the K^{*+} and the K^{*0} are produced in three-body final states. The K^{*+} production falls rapidly with increasing incident momentum, whereas the K^{*0} production remains relatively high. Branching ratios of K^{*+} into $K^0\pi^+$ and $K^+\pi^0$, and K^{*0} into $K^+\pi^-$ and $K^0\pi^0$ obtained from the fitting program are consistent with the expectations from isotopic-spin conservation.

The production of K^* states has been extensively analyzed in $K^\pm p$ reactions.[27-29] The experimental quantities that can be determined from these analyses are the production differential cross sections and three density matrix parameters that characterize the decay of the K^*. In our experiment, we are fortunate to be able to observe also the decay of the final-state fermion and deduce the parameters for the joint density matrix of the hyperon and K^*. Instead of three parameters, the most general decay is characterized by eleven independent terms. The details of the formulation are discussed in Appendix A, and the most general decay distribution is given by (A12).

Events from the reaction $\pi^- p \to \Sigma^0 K^{*0}$ in intervals I and II and from $\pi^- p \to \Lambda K^{*0} \to \Lambda K^+ \pi^-$ in intervals II and III were fit to this general decay distribution by means of weighted events and a maximum-likelihood method; these results along with selection criteria are presented in Table XIV. In interval I the $\Sigma^0 K^{*0}$ events, although they show a peripheral character, are distributed over all production angles, and the statistics allow us to determine density matrix parameters in three intervals or production angles. We made background subtractions for these

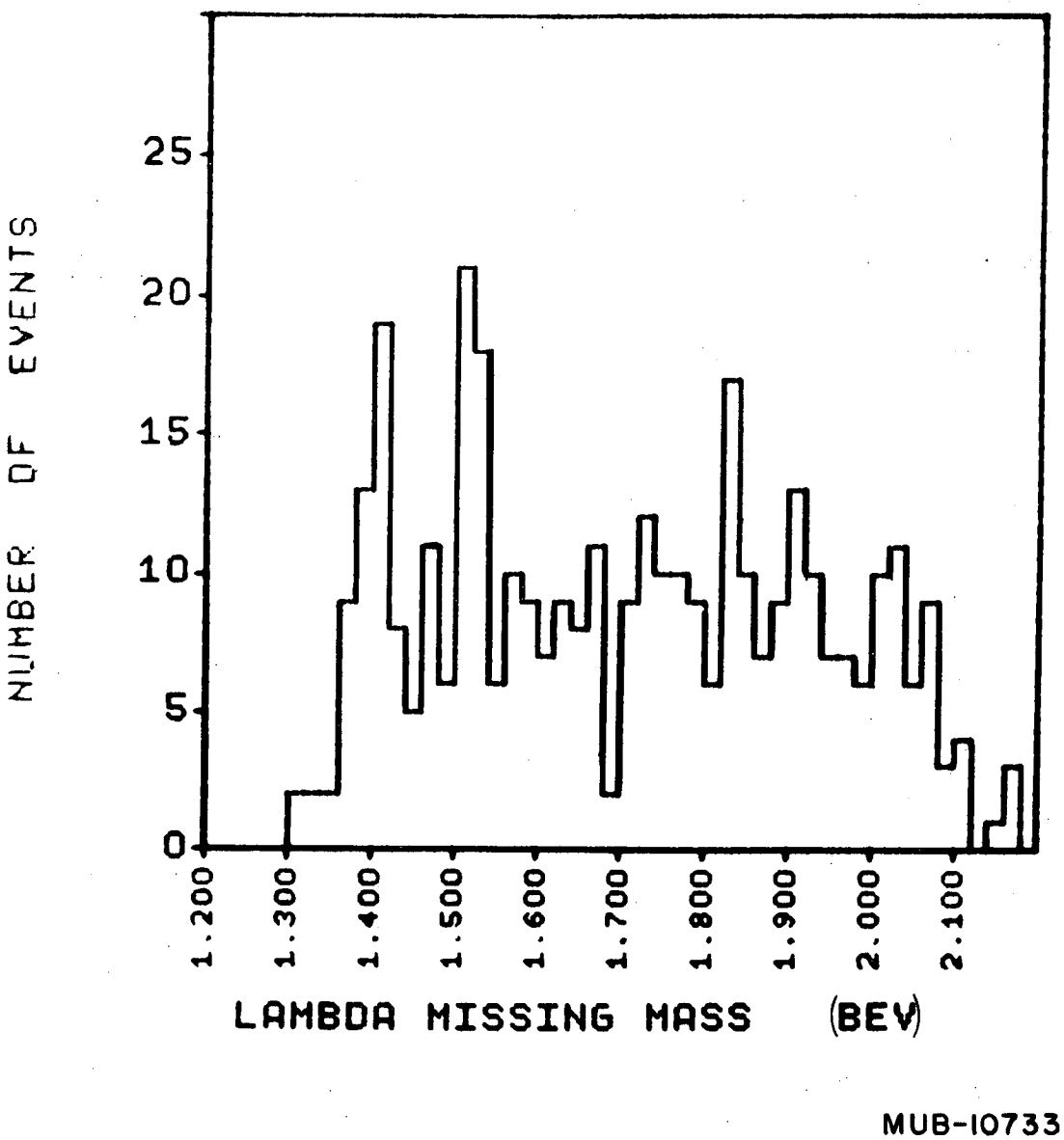

Fig. 18. Effective-mass distribution of the lambda and missing mass from the final state ΛK^0mm. $\Lambda\pi^0\pi^0$ and $\Sigma^0\pi^0$ are the most likely contributors to this histogram.

Table XIV. The YK^* selection criteria and density matrix elements.

Final state	Mass (BeV)	Production angle	Incident momentum (BeV/c)	(1) $\rho_{++++} + \rho_{+-+-}$	(2) $\mathrm{Re}(\rho_{++0+} - \rho_{+0+-})$	(3) $\mathrm{Im}(\rho_{++0+} - \rho_{+0+-})$	(4) $\mathrm{Re}\,\rho_{+++-}$	(5) $\mathrm{Im}\,\rho_{+++-}$	(6) $\mathrm{Im}\,\rho_{++-+}$	(7) $\mathrm{Im}\,\rho_{++-0}$	(8) $\mathrm{Im}\,\rho_{+0-+}$	(9) ρ_{++--}	(10) ρ_{+0-0}	(11) ρ_{+--+}
$\Sigma^- K^{*+}$ $\hookrightarrow K^+\pi^0$	0.850 - 0.920	-1.0 - 1.0	1.8 - 2.2	0.310 ± 0.034	-0.084 ± 0.044		-0.068 ± 0.028							
$\Sigma^0 K^{*0}$	0.861 - 0.921	-1.0 - 0.0	1.8 - 2.2	0.336 ± 0.043	0.064 ± 0.046	-0.111 ± 0.461	0.094 ± 0.038	-0.344 ± 0.278	-0.156 ± 0.247	-0.021 ± 0.348	0.353 ± 0.308	-1.24 ± 0.486	0.639 ± 0.330	-0.563 ± 0.415
$\Sigma^0 K^{*0}$	0.861 - 0.921	0.0 - 0.5	1.8 - 2.2	0.438 ± 0.036	0.021 ± 0.043	1.21 ± 0.313	0.149 ± 0.030	0.228 ± 0.360	-0.077 ± 0.250	0.067 ± 0.274	-0.116 ± 0.259	-0.045 ± 0.461	0.170 ± 0.314	-0.062 ± 0.423
$\Sigma^0 K^{*0}$	0.861 - 0.921	0.5 - 1.0	1.8 - 2.2	0.368 ± 0.052	-0.076 ± 0.065	0.333 ± 0.519	0.080 ± 0.046	0.495 ± 0.417	-0.122 ± 0.345	-0.309 ± 0.409	-0.933 ± 0.406	-0.816 ± 0.580	-0.223 ± 0.529	-0.686 ± 0.607
$\Sigma^0 K^{*0}$	0.861 - 0.921	0.5 - 1.0	2.9 - 3.3	0.477 ± 0.055	0.009 ± 0.031	0.215 ± 0.379	0.149 ± 0.039	-0.578 ± 0.356	0.785 ± 0.273	0.048 ± 0.235	-0.771 ± 0.277	-0.291 ± 0.487	-1.81 ± 0.570	-0.131 ± 0.497
ΛK^{*0} $\hookrightarrow K^+\pi^-$	0.861 - 0.921	0.5 - 1.0	2.9 - 3.3	0.372 ± 0.035	0.052 ± 0.036	-0.339 ± 0.100	0.075 ± 0.027	-0.028 ± 0.075	0.151 ± 0.053	0.034 ± 0.061	-0.042 ± 0.061	0.430 ± 0.082	-0.072 ± 0.097	0.039 ± 0.086
ΛK^{*0} $\hookrightarrow K^+\pi^-$	0.861 - 0.921	0.5 - 1.0	3.8 - 4.2	0.367 ± 0.055	0.046 ± 0.082	-0.701 ± 0.198	0.082 ± 0.040	0.203 ± 0.114	0.050 ± 0.075	-0.110 ± 0.078	0.124 ± 0.086	0.377 ± 0.123	0.002 ± 0.108	0.078 ± 0.130

parameters in all three intervals of production angle, and the corrections were less than the statistical errors; there are no competing processes in this final state. In interval II, we found parameters for events in the forward direction ($0.5 \leq \cos\alpha \leq 1.0$). In interval III, data were insufficient to determine fitted distributions.

Although data are plentiful in interval I for the process $\pi^- p \rightarrow \Lambda K^{*0}$, we were unable to satisfactorily compensate for the presence of the competing process $\pi^- p \rightarrow Y^{*-} K^+$ and have thus not presented results here. The Y^{*-} production is negligible in intervals II and III, so data are presented for events in the forward direction ($0.5 \leq \cos\alpha \leq 1.0$) since K^* production is extremely forward peaked at these momenta. When background subtractions for the density matrix parameters were made, the convections were less than the statistical errors.

The subtracted angular distributions for production and decay of the K^* for the selections discussed above are presented in Figs. 19 through 21, along with the curves obtained from the maximum-likelihood fits to the density matrix parameters.

The predictions of simple one-particle exchange for the decay density matrix of the fermion and K^* final state are well known. The K exchange predicts a $\cos^2\theta$ decay with respect to the beam in the K^* rest frame and no other correlations. All of the 11 parameters should be identically zero at all production angles. For K^* exchange or any other member of the "normal" spin-parity series 1^-, 2^+, $3^- \cdots$, term one ($\rho_{++++} + \rho_{+-+-}$) should equal 0.5 and only term four (Re ρ_{+++-}) of the rest is allowed to be nonzero. The K^* decay distribution is of the form $\sin^2\theta(1 + \alpha\cos 2\phi)$. Combined K and K^* exchange yield no new nonzero terms; the quantity $1 - 2(\rho_{++++} + \rho_{+-+-})$ measures the fractional amount of K exchange present.

Taken at face value, terms one and four for this experiment indicate that K^* exchange dominates the production of both $\Sigma^0 K^{*0}$ and ΛK^{*0}. For each set of density matrix parameters, we formed a chi square for the hypothesis that the nine unallowed parameters are consistent with zero. For forward, intermediate, and backward production angles for

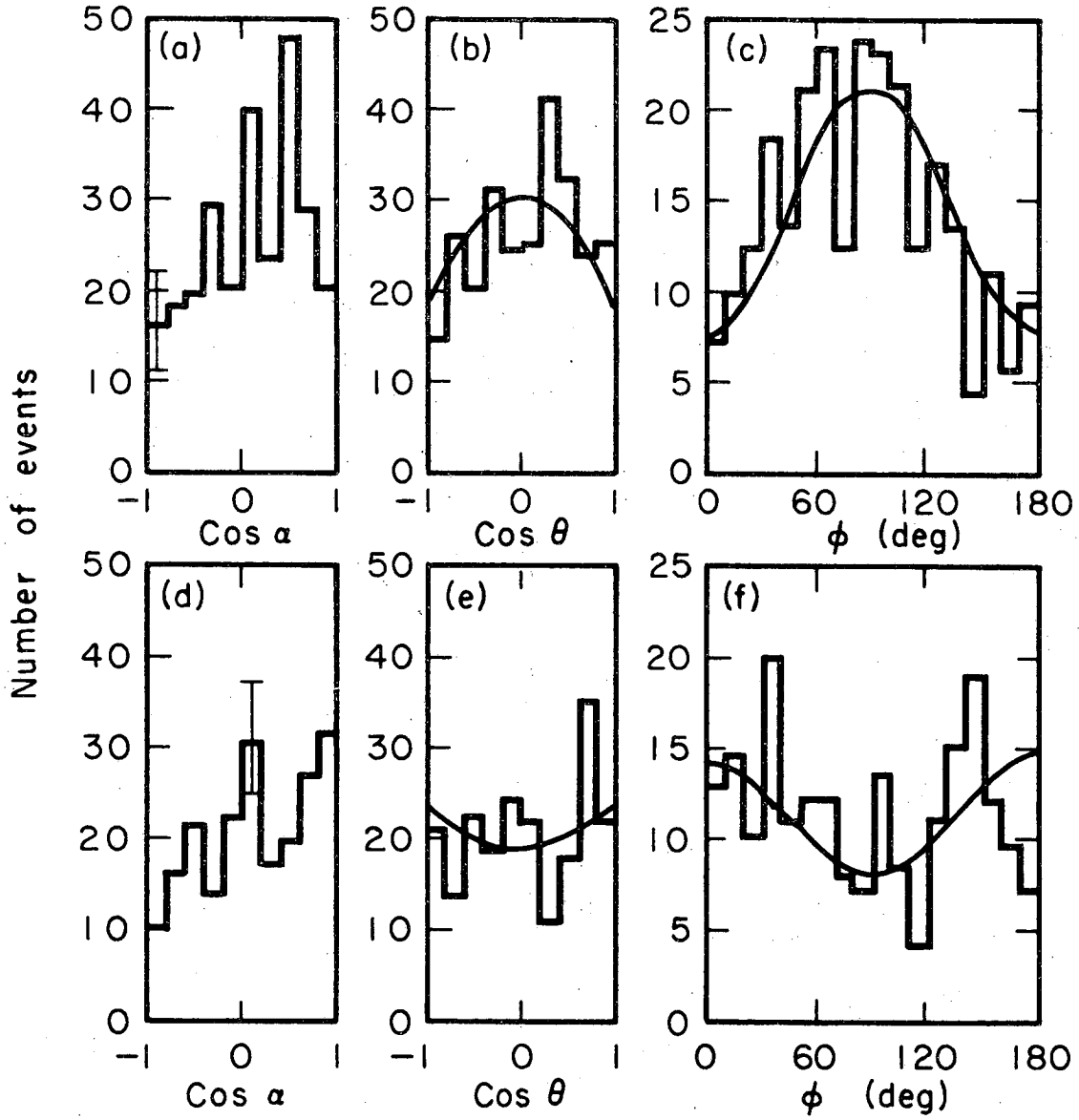

MUB 11461

Fig. 19. Angular distributions (a), (b), (c) for K^{*0} from $\Sigma^0 K^{*0}$ in interval I; (d), (e), and (f), K^{*+} from $\Sigma^- K^{*+}$ in interval I. $\cos\alpha$, $\cos\theta, \phi$ are defined on page 43. $\hookrightarrow K^+\pi^0$

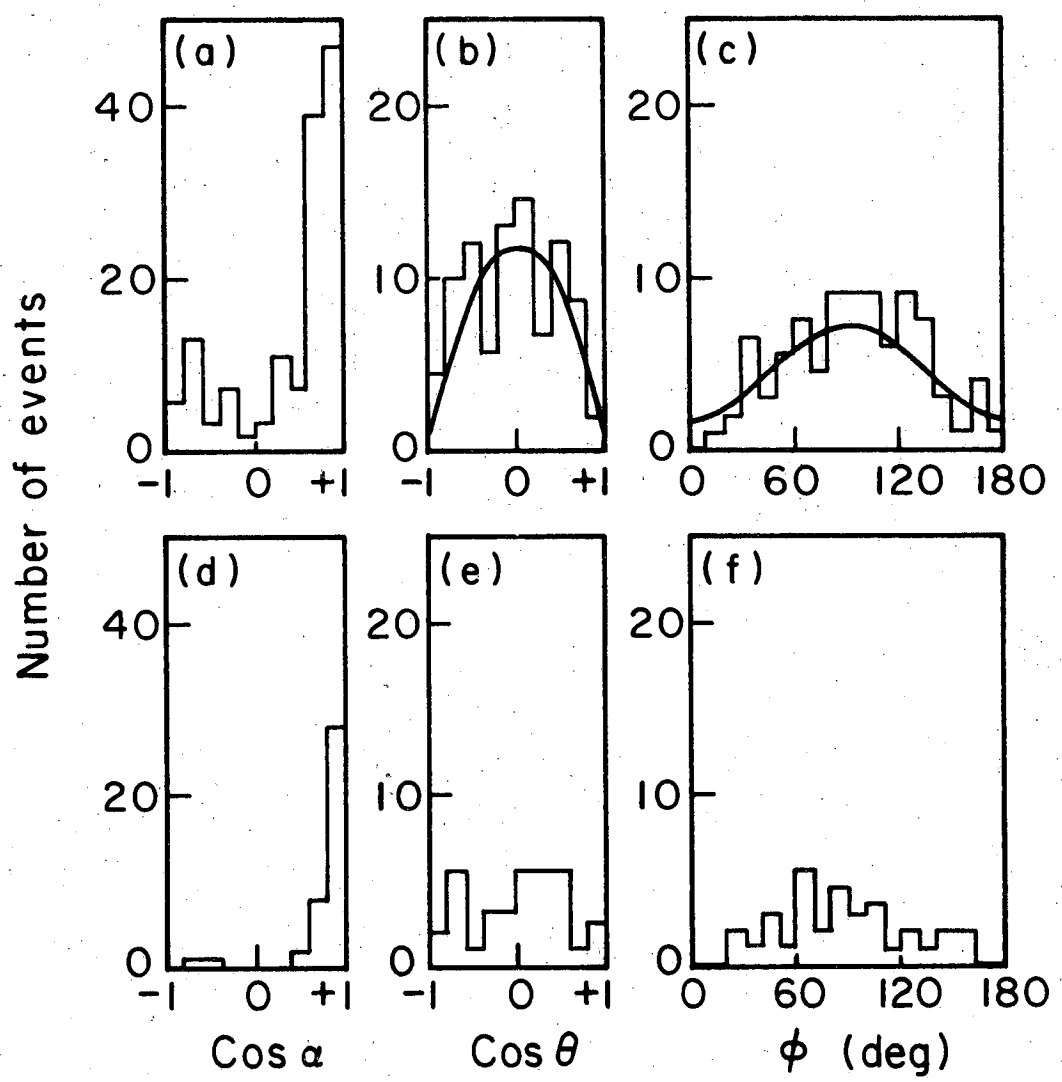

MUB-11787

Fig. 20. Angular distributions for K^{*0} from $\Sigma^0 K^{*0}$. (a), (b), (c), in interval II; (d), (e), (f) in interval III. Histograms of $\cos\theta$ and ϕ are for events with $0.5 \leq \cos\alpha \leq 1.0$. $\cos\alpha$, $\cos\theta$, ϕ are defined on page 43.

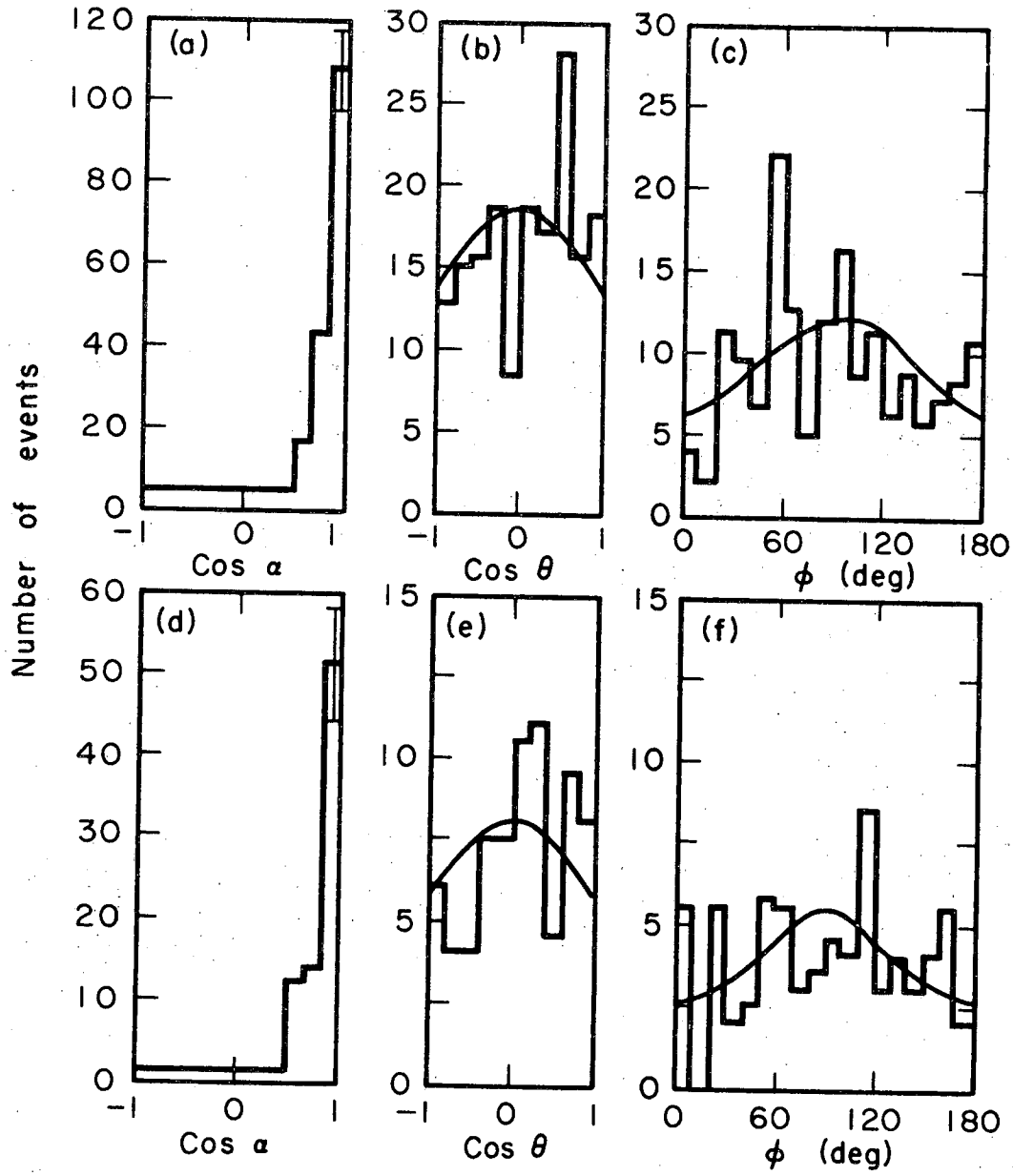

MUB-11458

Fig. 21. Angular distributions for K^{*0} from ΛK^{*0} (a), (b), and (c) in interval II, (d), (e), and (f) in interval III. Histograms of $\cos\theta$ and ϕ are for events with $0.5 \leq \cos\alpha \leq 1.0$. $\cos\alpha$, $\cos\theta$, ϕ are defined on page 43.

$\Sigma^0 K^{*0}$, we obtained chi square values of 12.9, 17.1, and 19.3 for nine degrees of freedom. For interval II in the forward direction, we obtained a chi square of 18.1. For ΛK^{*0} production in intervals II and III, we obtained 64.3 and 38.2. The correlations between the parameters were properly taken into account. We conclude that on the basis of decay correlations alone, simple one-particle exchange is not definitely ruled out for $\Sigma^0 K^{*0}$ but is certainly inconsistent for ΛK^{*0}.

The differential cross sections predicted for either K or K^* exchange are in gross disagreement with the experimental distributions presented in Figs. 19 through 21. Simple one-particle exchange does not satisfactorily explain the data for the processes $\pi^- p \rightarrow \Sigma^0 K^{*0}$ and $\pi^- p \rightarrow \Lambda K^{*0}$.

The failure of the unmodified one-particle-exchange model here is, of course, not a unique occurrence. Many reactions have deviated significantly from the model's predictions, in particular in the production angular distribution. To overcome this deficiency, several authors[30] have proposed an approach that leads to the absorption model. The ideas that they present seem intuitively plausible, but the formulation in a quantitative fashion requires many brutal approximations. For an experiment with low statistics, the theory is flexible enough that reasonable fits can be obtained to all aspects of the data. For experiments with sufficient statistical accuracy to test the validity of the model in detail, one must decide to what extent a bad fit is due to the approximations and to what extent to the inaccuracies of the theory. Detailed analyses of the absorption model have been discussed elsewhere;[29, 31-33] such an undertaking is too ambitious for the data available here.

Rather we shall ask the question: Given the absorption model, to what extent is our conclusion about the dominance of vector exchange modified for $\pi^- p \rightarrow YK^{*0}$? We use a formulation of Huff's absorption model,[34] which is outlined in Appendix B. The production angular distribution and density matrices appropriate to a given reaction and momentum interval were fit to the theory, and the values of the unknown parameters that minimized chi square determined. In general, there was more than one minimum corresponding to different choices of

relative sign between the fitted coupling constants. For all three data sets fitted, however, the characteristics of all minima were the same. The pKY coupling constant was small; $g_p^2/4\pi \approx 1$ for ΛK^{*0} in intervals II and III; g_p^2 was of necessity set equal to zero to get convergence for $\Sigma^0 K^{*0}$ in interval I. The vector coupling g_v and tensor coupling g_t were large and of the same order of magnitude for all cases $|g_v| \approx |g_t| \approx 10$. The parameters characterizing (a) the final state YK^* interaction, (b) σ_f, the total cross section, and (c) A_f, the slope of the differential elastic cross section, were not determined with any sensitivity by the fitting procedure. The angle χ was small in all cases. (For precise definitions of these quantities, see Appendix B). As an example, the best fit for ΛK^{*0} in interval II is shown in Fig. 22. Also shown in Fig. 22(a) is the prediction for the variation of term one with the best fit coupling constants but with no absorption. Except in the extreme forward direction (the vector particle-exchange contribution decreases near $\theta = 0$), g_v and g_t on the order of 10 and $g_p^2/4\pi$ on the order of 1 corresponds to dominance of vector exchange over pseudo-scalar exchange. [$1 - 2(\rho_{++++} + \rho_{+-+-})$ is small.] We conclude, therefore, that even when we allow for the presence of absorptive effects, vector-exchange processes are strongly present. Such an observation is somewhat surprising, since we expect that the $K^*K^*\pi$ coupling constant is suppressed because the vertex does not conserve A parity.[35]

Density matrix parameters were also obtained for the processes $\pi p \to \Sigma^- K^{*+}$ from the final state $\Sigma^- K^+ \pi^0$. Here $\Sigma^- K^0 \pi^+$ events were not used because of the presence of the several Y^* states in that channel. Only the terms that remain after integrating over the decay of the Σ^- are presented, since strong scanning biases are associated with that distribution. Background for K^{*+} events is rather significant, but the decay distribution does not possess features very different from those of the background control region. Consequently the subtraction changed parameters slightly for this state. Angular distributions are presented in Fig. 19.

The production distribution is not backwards peaked as one would expect from a baryon-exchange model; absorptive effects would serve

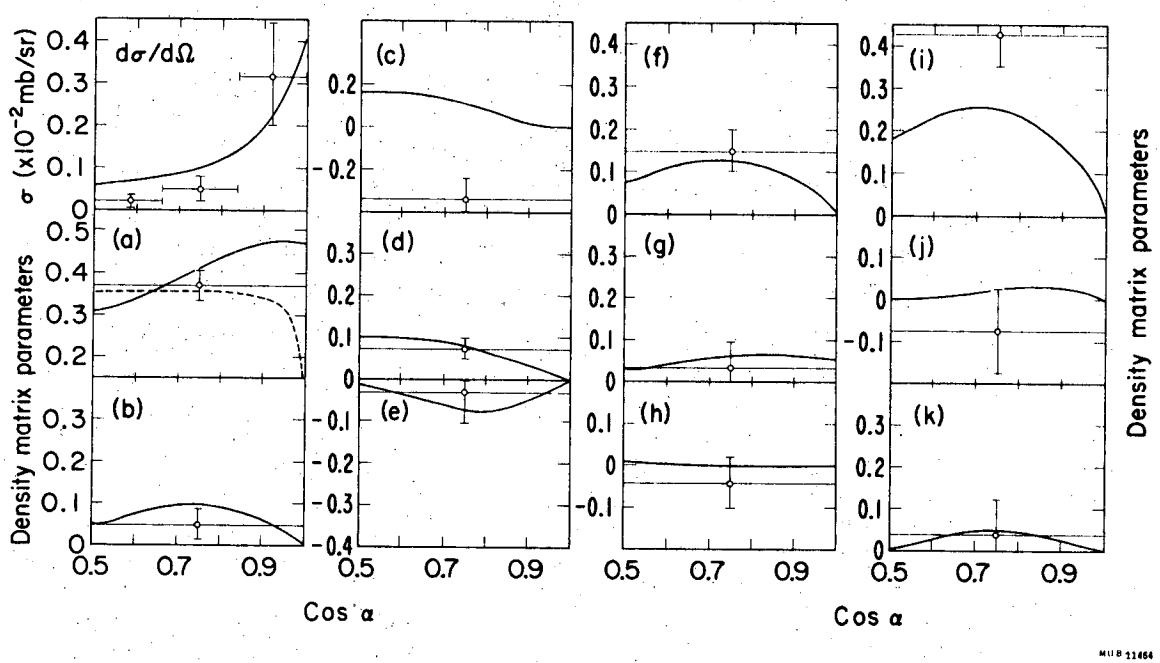

Fig. 22. Differential cross section for $0.5 \leq \cos\alpha$, (a) through (k) density matrix parameters in the forward direction for $\pi^- p \rightarrow \Lambda K^{*0}$ in interval II with the theoretical curves from the absorption model with the best fit parameters $g_p^2 = 1.14$ $g_v = 11.7$, $g_T = -23.3$, $\sigma_f = 58.1$ μb, $A_f = 7.8$ (BeV)$^{-1}$, $\chi = 0.16$.

only to increase this peaking. Some more complicated mechanism therefore is responsible for the production of this state.

7. $K^*(1440)$

This state is definitely present only in the interval III and in the final state $\Lambda K^+\pi^-$. The best fit to the mass and width, given in Table IX, are in disagreement with the values obtained for K^-p experiments.[36, 37] Fits were attempted with Breit-Wigner matrix elements of higher-momentum states, but the results were within errors of the quoted values. Although the discrepancy is probably the result of a statistical fluctuation in our sample of events, an examination of possible biases that might produce a shift in the mass of $K\pi$ systems was undertaken.

The effective-mass distribution for the $K\pi$ projection calculated with measured (unfitted) values for the momenta was examined, but no significant shift was noted in either the $K^*(890)$ or $K^*(1440)$ regions. The fact that the fit to the mass of the $K^*(890)$ gives a value of 892 ± 3 MeV indicates that there is no overall displacement in the $K\pi$ spectrum. The unfitted values of the momenta of the incident pion and the outgoing K and π were used to calculate the mass of the "missing" Λ. The distributions in Λ mass for $K\pi$ effective mass higher and lower than 1 BeV were examined separately, but no significant shifts were found between the two plots. Since our measurements give correct values for the $K\pi$ mass in the vicinity of the $K^*(890)$ and we detect no systematic variations with increasing $K\pi$ effective mass, we conclude that if we are observing the same state as in the K^-p experiments, then increased statistics would yield consistent values for the resonance mass.

The production and decay angular distribution for the $K^*(1440)$ are shown in Fig. 23. The production is peripheral but not so much so as that of the $K^*(890)$ at this momentum. The decay distribution in $\cos\theta$ was fit by distribution $a + b\cos^2\theta$ and distribution $a + b\cos^4\theta$. (No $\cos^2\theta$ term was needed for the second distribution.) Using weighted events, we see that the ratio of likelihoods for these two distributions is $L_1/L_2 = 1/6.3$. The expected distributions for various exchanged particles and spin-parity assignments are discussed in more detail in

Ref. 38. As reported there, the assignment 2^+ is favored by our data but the assignment 1^- is not excluded.

Several experimenters report the possible existence of other decay modes for the $K^*(1440)$.[36,37] Figures 24(a) through (d) show the effective-mass plots for $K\pi\pi$ combinations from the final states $\Lambda K^+\pi^0\pi^-$ and $\Lambda K^0\pi^+\pi^-$; here we have selected the mass of either the appropriate $K\pi$ combinations to be in the K^* interval or $\pi\pi$ combinations in the ρ interval. Also shown are K mm from the final state ΛK^0 mm with the missing mass in the η region, $K^0\pi^+\pi^-\pi^0$ from the final state $\Lambda K^0\pi^+\pi^-\pi^0$ with the three-pion mass in the ω region. We see no definite evidence for $K^*(1440)$ decay into any of these modes. Upper limits for the branching ratios of $K^*(1440)$ into these channels are presented in Ref. 39.

8. Kappa

Evidence for this state was first reported by Alexander et al.[3] in the final state $\Sigma^-K^+\pi^0$ from the $\pi 72$ experiment. Those data have been combined with the events from the present experiment in Fig. 12(g). The combined data are not conclusive evidence for the existence of this state. After removal of events with the $\Sigma^-\pi^+$ effective mass in the regions of $Y^*(1405)$, $Y^*(1520)$, and $Y^*(1660)$, the final state $\Sigma^-K^0\pi^+$ shows no evidence for this enhancement. No effect is observed at other momenta or in the neutral $K\pi$ charge state. We must therefore conclude that the data from π^-p interactions do not in themselves constitute independent evidence for the existence of the kappa.

The deviations from the calculated distributions in the $\Sigma^-\pi^0$ spectrum are entirely associated with the $K^*(890)$ and are a reflection of its nonisotropic ($\approx \cos^2\theta$ along K^* direction) decay distribution.

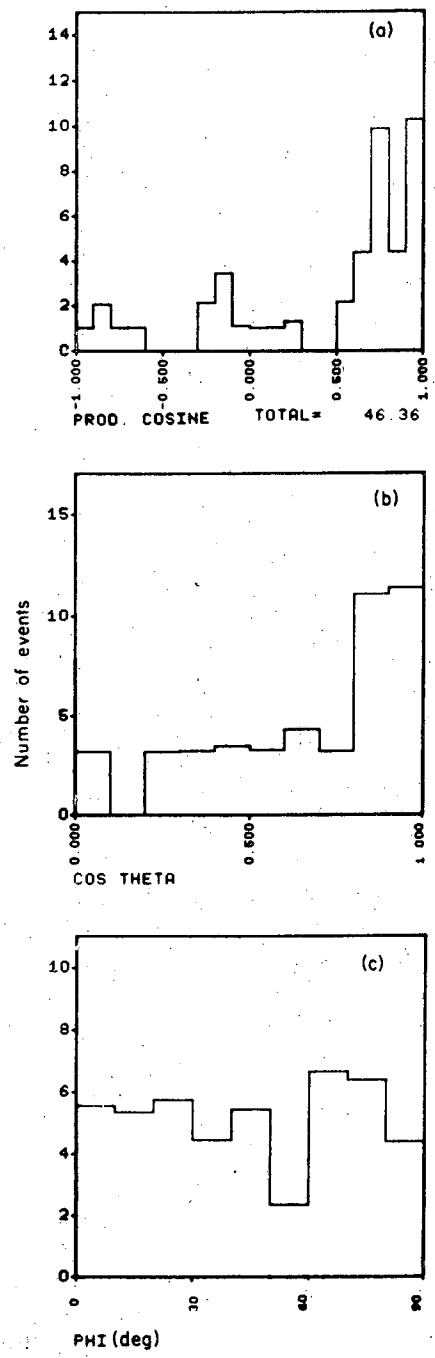

Fig. 23. Angular distributions for the $K^*(1440)$. $\cos\alpha$, $\cos\theta$, ϕ are defined on page 43.

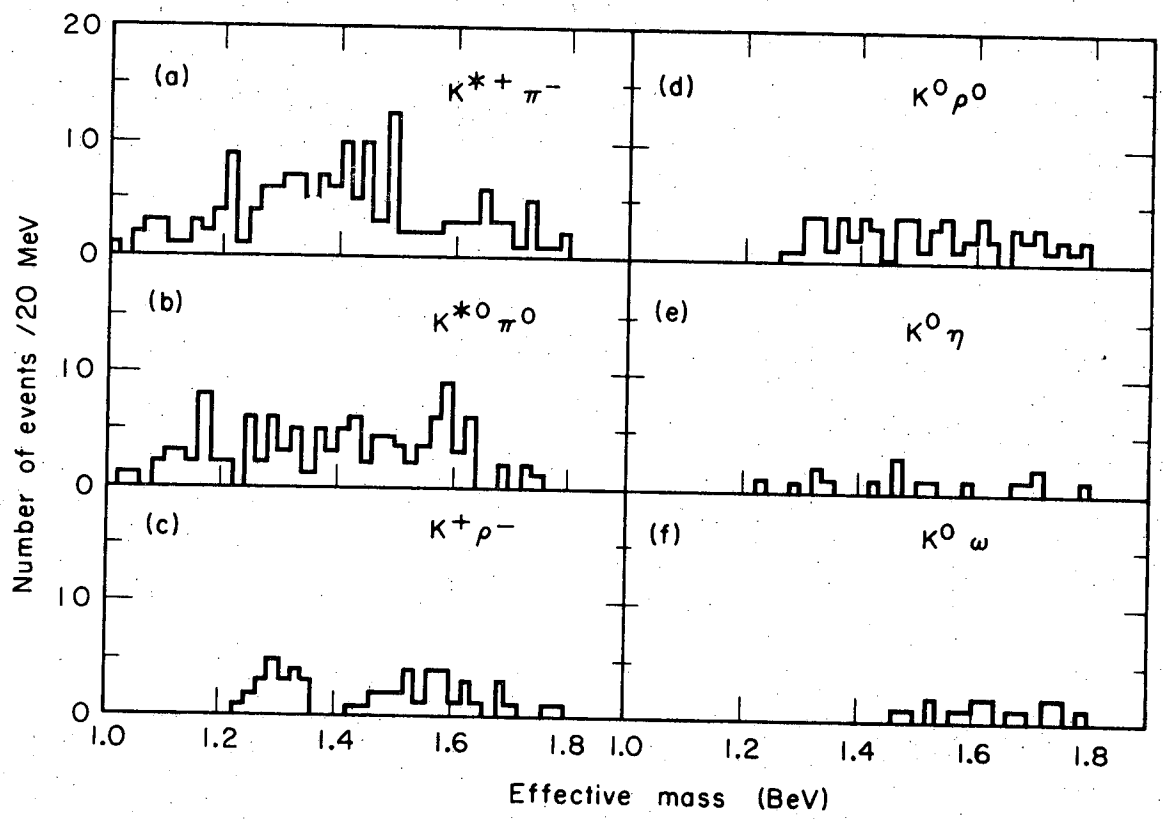

MUB-11462

Fig. 24. Effective-mass distributions for various particle combinations.

B. Four-Body Final States

1. $\Sigma K\pi\pi$

The dominant features of these final states in intervals II and III are shown in Fig. 25, where the effective mass of $(\Sigma\pi)^0$ is plotted against the effective mass of $(K\pi)^0$. Here many of the events have proceeded through $Y^* K^*$ intermediate states. The $Y^*(1405)$, $Y^*(1520)$, and $Y^*(1660)$ are all definitely present and were produced in association with $K^*(890)$. Our estimates for the cross sections of these processes are shown in Table X. No enhancements are noticed in the $(K\pi\pi)^\pm$ distributions.

2. $\Lambda K\pi\pi$

In interval I, the final states $\Lambda K^+\pi^0\pi^-$ and $\Lambda K^0\pi^+\pi^-$ are dominated by double-resonance production of $Y^*(1385)$ $K^*(890)$. In intervals II and III, the cross sections for Y^*K^* and nonresonant $\Lambda K\pi\pi$ have both risen; the resonant states no longer play such an important part in these final states. Figures 26 through 29 show projections of interest and distributions calculated for these final states with the fitted values of each resonant state present. The fits are in general good.

The spectra from both $\Lambda K^0\pi^+\pi^-$ and $\Lambda K^+\pi^0\pi^-$ in interval III, in addition to showing the expected peak at 1385 MeV, also have narrow enhancements in the vicinity of 1520 MeV. The events in these bins from the two plots have different characteristics, however. They are not in the same mass interval but in adjacent bins. The ratio of signal to background for $\Lambda K^+\pi^0\pi^-$ events improves with the delection of $Y^{*0}(1385)$ events, whereas events from $\Lambda K^0\pi^+\pi^-$ are correlated with the presence of $Y^{*+}(1385)$. If this is a legitimate effect it is $I = 1$, and we would expect to see production of the states Y^{*0} and Y^{*-} but we do not. A statistical fluctuation more plausible than any existing model would have to be devised to explain these phenomena.

The effective-mass distribution for $K^+\pi^-$ in interval III [Figure 28(d)] shows deviations from the calculated distribution at low values for the $K\pi$ mass. This enhancement is entirely associated with events for which the mass of $\Lambda\pi^-$ falls in a band about 1385 MeV. Although such an enhancement might also be explained by a triangle diagram,[40] we believe this effect to be statistical.

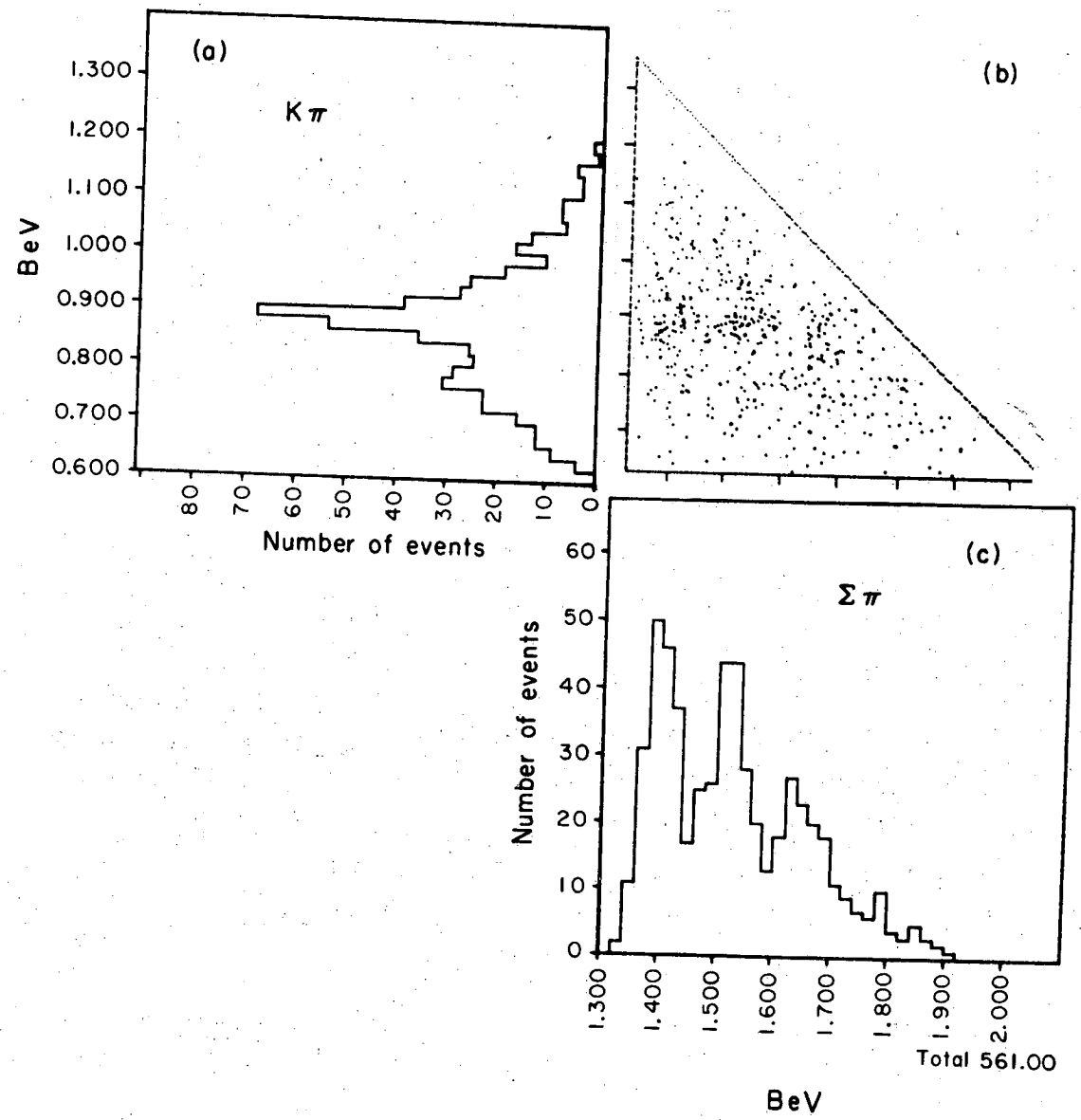

Fig. 25. Effective-mass projections and scatter plot for $(\Sigma\pi)^0$ and $(K\pi)^0$ systems.

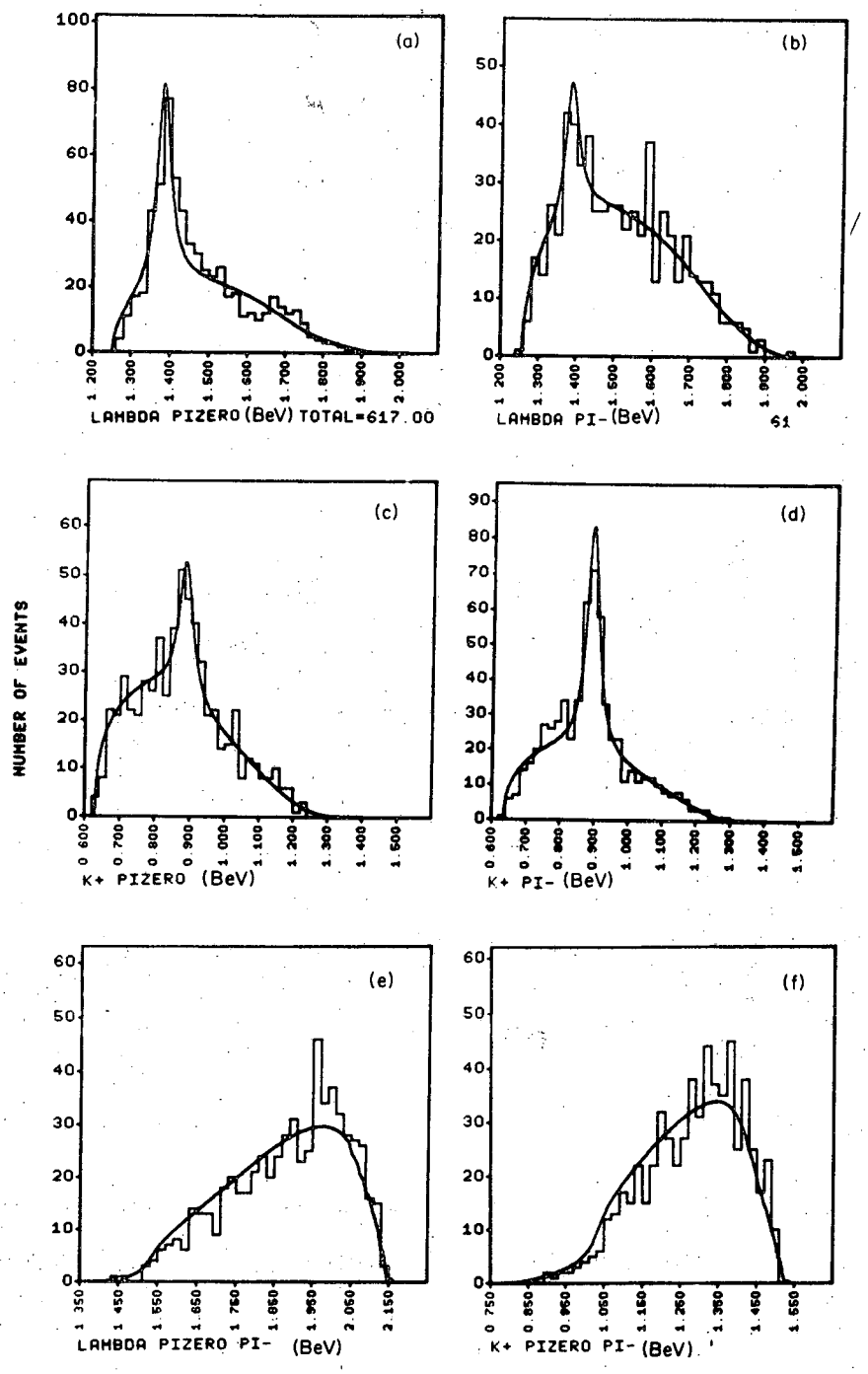

Fig. 26. Effective-mass projections for the final state $\Lambda K^{+}\pi^{0}\pi^{-}$ in interval II.

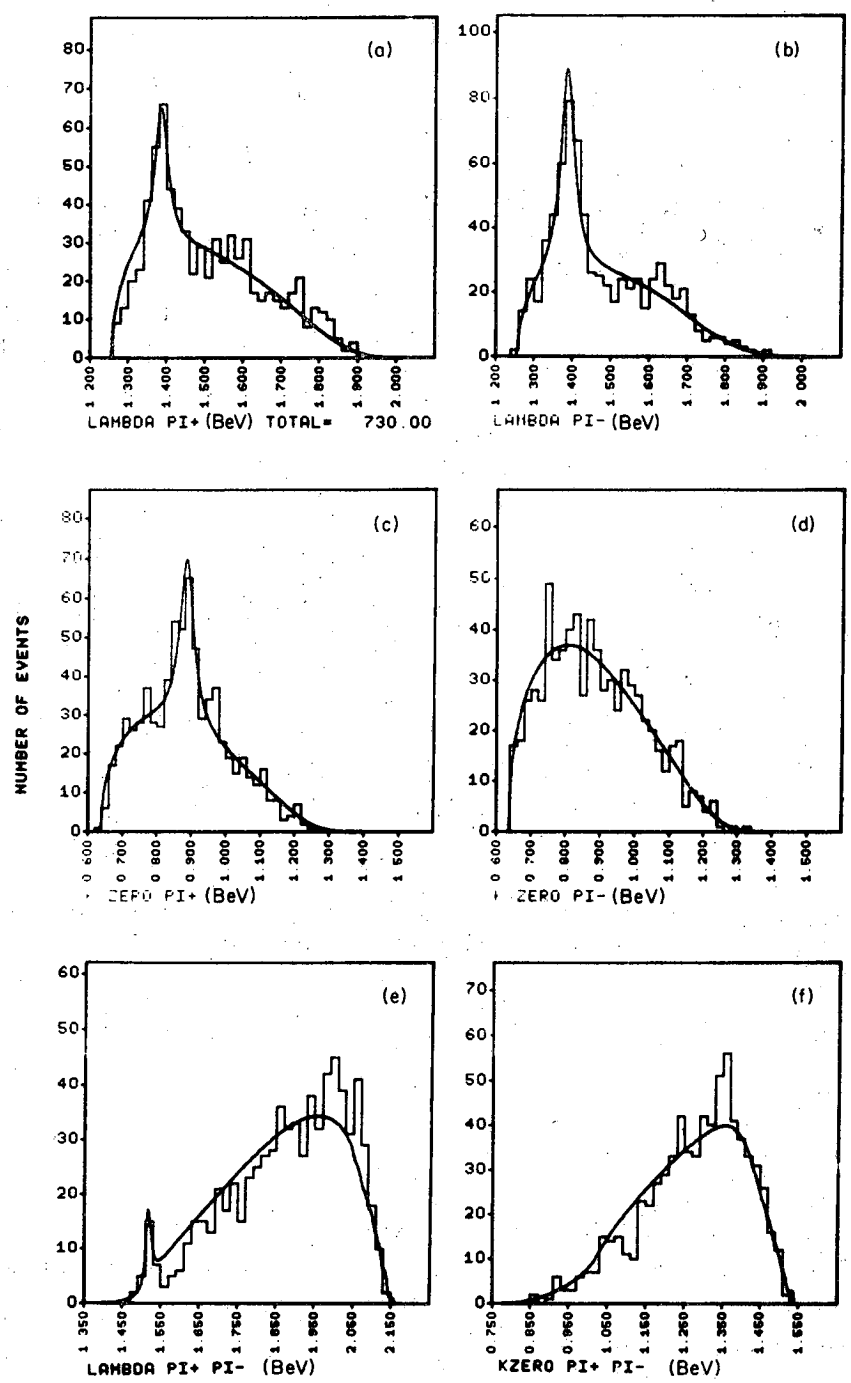

Fig. 27. Effective-mass projections for the final state $\Lambda K^0\pi^+\pi^-$ in interval II.

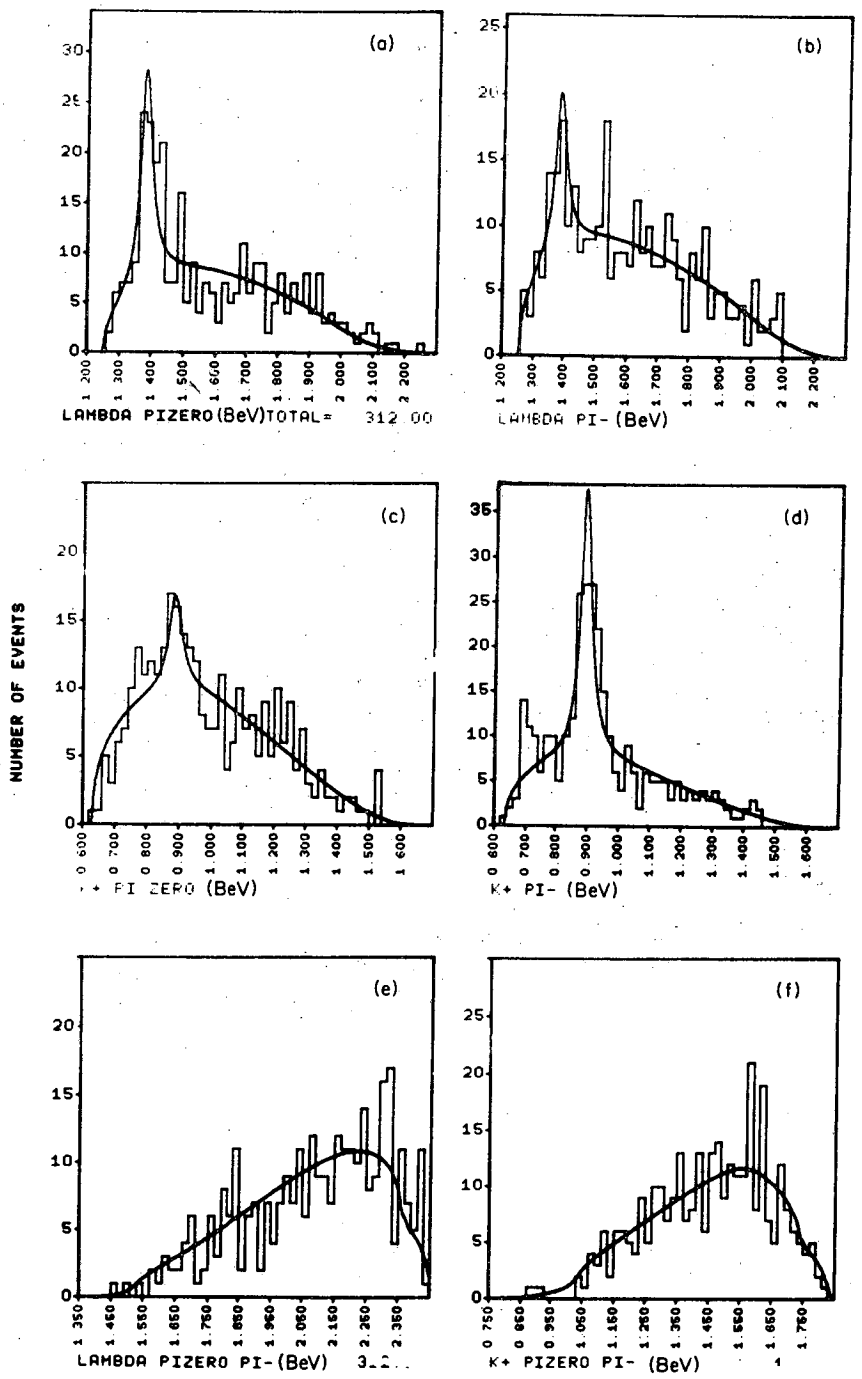

Fig. 28. Effective-mass projections for the final state $\Lambda K^+\pi^0\pi^-$ in interval III.

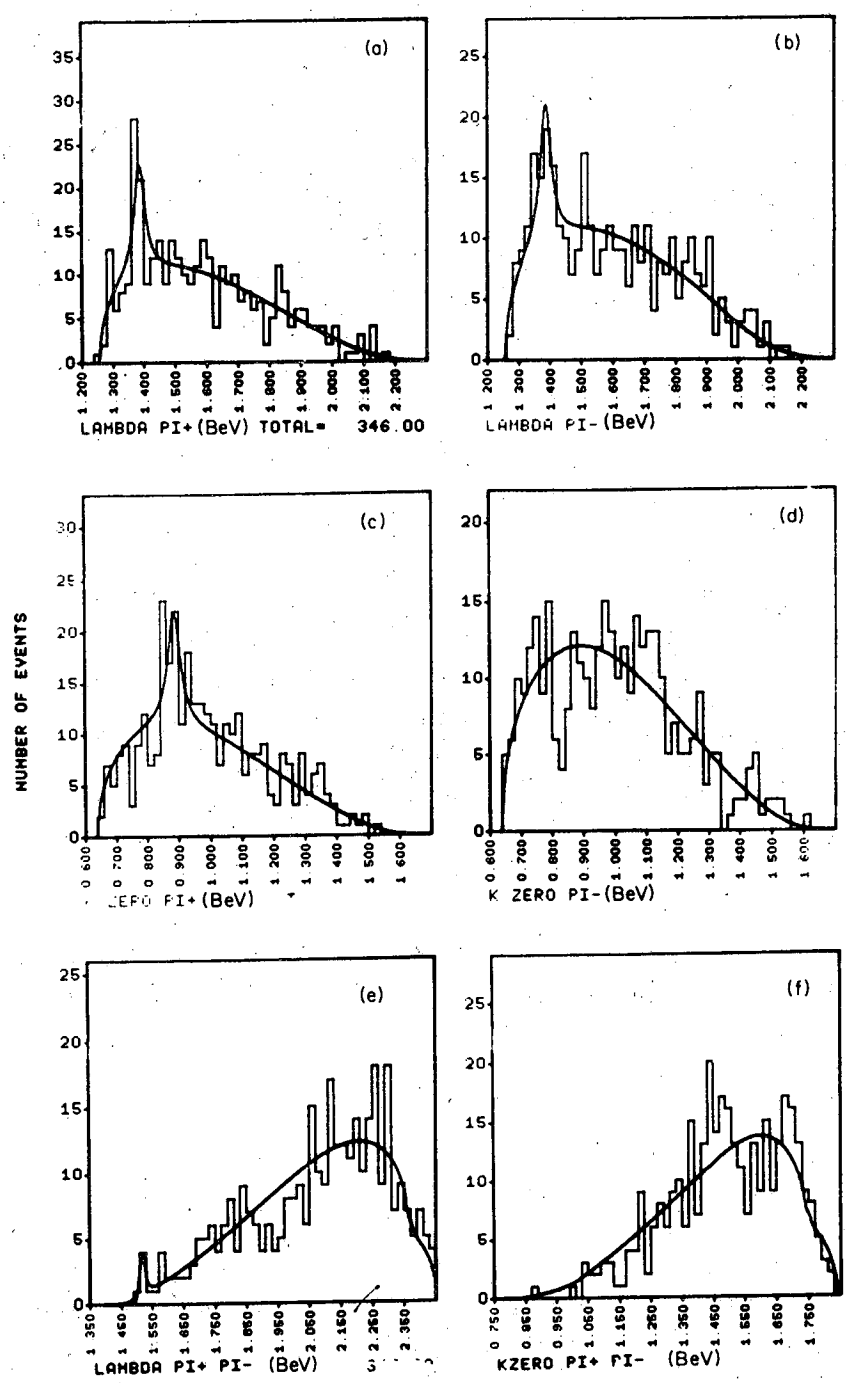

Fig. 29. Effective-mass projections for the final state $\Lambda K^0 \pi^+ \pi^-$ in interval III.

The $K\pi\pi$ spectra were carefully examined for evidence of new resonant states that are not yet firmly established.[41-46] The distributions with no selections are well explained by the fitted curves with the possible exception of an excess of events in the vicinity of 1350 MeV in $K^0\pi^+\pi^-$ in interval II. In Fig. 30 are mass plots for $K\pi\pi$ from interval II with $Y^*(1385)$ events removed, and either (a) $K^+\pi^-$ or $K^+\pi^0$ from $\Lambda K^+\pi^0\pi^-$ or (b) $K^0\pi^+$ from $\Lambda K^0\pi^+\pi^-$ in the $K^*(890)$ region. (There is no evidence for ρ production in $\Lambda K\pi\pi$ final states.) No significant increase in deviation from calculated distributions is observed. In particular, we see no evidence for a resonance at 1175, 1215, or 1275 MeV. Our data at 2.6 and 2.8 BeV and in interval II divided into smaller divisions were separately examined, and no enhancement was observed whose cross section varied rapidly with momentum.

In Fig. 31 are plotted effective-mass distributions for $Y^*(1385)\pi$ in interval II with K^* events excluded. We see no evidence for new resonance states.

C. Five-Body Final States

The five-body final states are produced with small cross sections at the momenta accessible here. In this experiment, there is some evidence for the production of strongly resonating states $Y^*(1405)$, $Y^*(1520)$, $Y^*(1385)$, and $K^*(890)$. In addition, we observe in the final state $\Lambda K^0\pi^+\pi^-\pi^0$ the production of ω, as shown in Fig. 32(a). The effective-mass plots for $\Lambda\omega$ and $K^0\omega$ are shown in Figs. 32(b) and (c). The curves in these plots are for an incident pion momentum of 3.2 BeV/c, but the data is from events at all momenta. Statistics are quite limited; no striking effects are seen.

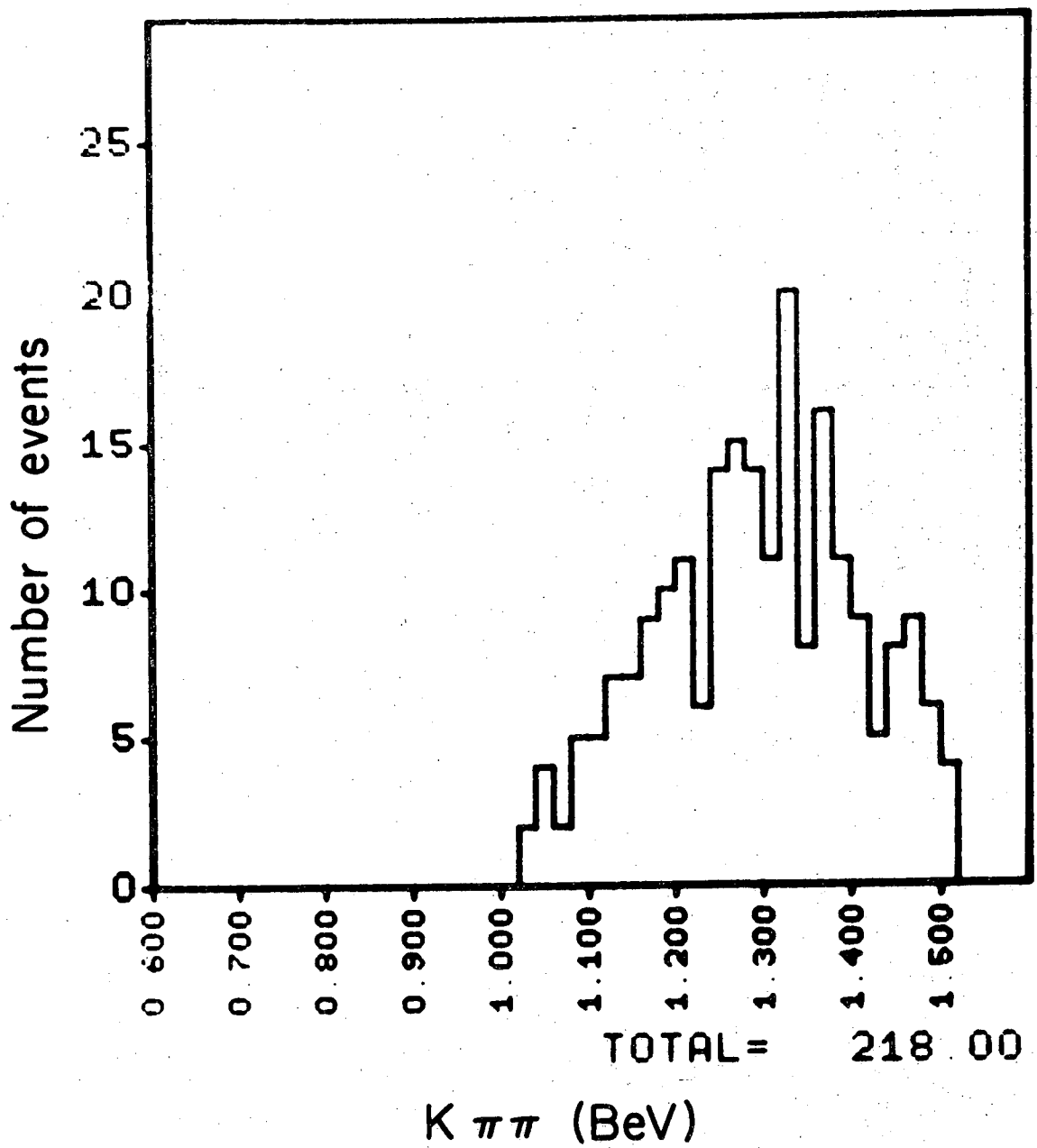

Fig. 30. Effective-mass of $(K\pi\pi)^0$ with selections described in text.

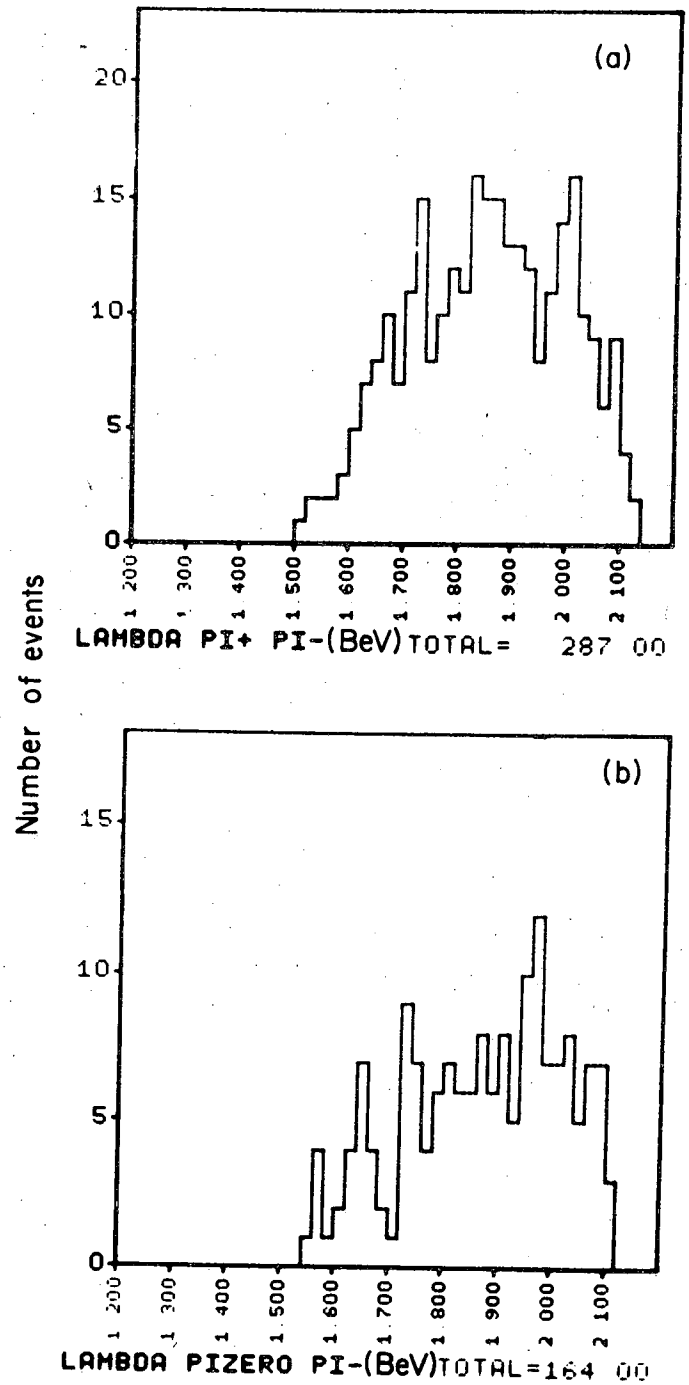

Fig. 31. Effective-mass of $(\Lambda\pi\pi)^0$ and $(\Lambda\pi\pi)^-$ with selections described in text.

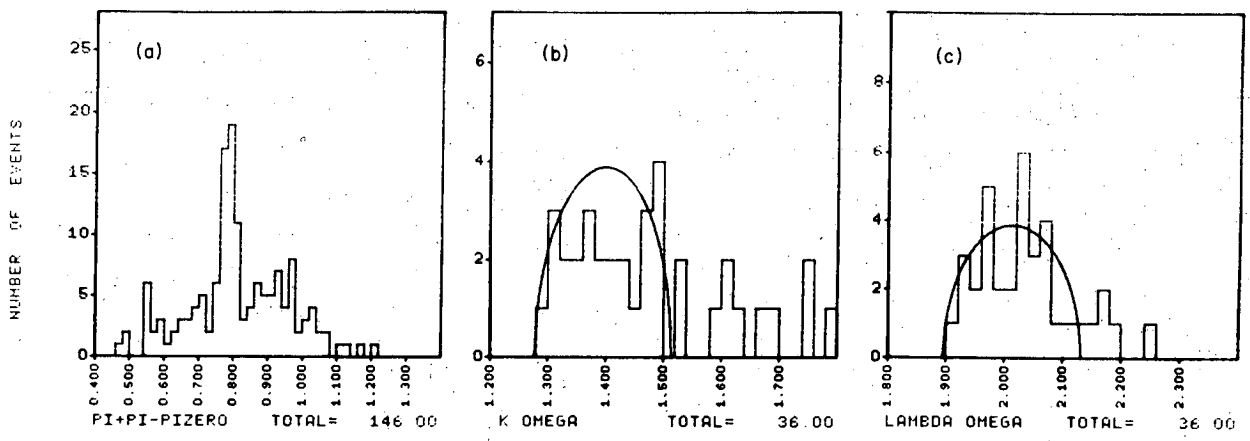

MUB-10725

Fig. 32. Effective-mass distributions from the final state $\Lambda K^0\pi^+\pi^-\pi^0$. (a) $\pi^+\pi^-\pi^0$ (b) $K^0\pi^+\pi^-\pi^0$ with the effective mass of $\pi^+\pi^-\pi^0$ in the ω region and (c) $\Lambda\pi^+\pi^-\pi^0$ with the effective mass of $\pi^+\pi^-\pi^0$ in the ω region. The curves are the phase-space distributions calculated for a beam momentum of 3.2 BeV/c.

V. SUMMARY AND CONCLUSIONS

In conclusion, we find that the principal features of the data are well explained by simple models describing the presence of well-established resonant states. "Peripheral" phase space necessary at higher energies[47] or new resonant phenomena are not needed for a complete description. We find that in general the lower lying states are more copiously produced than higher mass states in the same channels. Production of $Y^*(1405)$ and $Y^*(1520)$ is greater than that of $Y^*(1660)$, and the states $Y^*(1765)$ and $Y^*(1815)$ are not definitely observed. The $K^*(890)$ is more strongly produced in interval III than is $K^*(1440)$. The cross sections for resonant-state production in general decrease with increasing beam momentum. From these observations, we draw the tentative conclusion that resonance production will not play such a central part in characterizing strange-particle final states from $\pi^- p$ interactions at higher energies.

Simple one-particle-exchange models are fairly successful in describing the decay distributions of $Y^{*-}(1385)K^+$, $Y^{*0}(1520)K^0$, and $\Sigma^0 K^{*0}(890)$, but fail for $\Lambda K^{*0}(890)$. The absorption model is able to fit the production angular distributions for ΛK^{*0} and $\Sigma^0 K^{*0}$ states, and in a qualitative fashion to explain all the decay correlations. The K^* exchange appears to dominate K exchange in the processes $\pi^- p \rightarrow YK^{*0}$.

ACKNOWLEDGMENTS

It is a pleasure to acknowledge the support and encouragement of Professor Luis Alvarez and the members of his group without whose efforts this work would not have been possible.

I sincerely appreciate the diligent and untiring effort of the staff of the library, and scanning and measuring groups, and especially the efforts of Werner Koellner, the experiment coordinator.

I would like to thank Drs. Janos Kirz, Suh Urk Chung, Orin Dahl, Stanley Flatté, and Richard Hess for many enlightening discussions and criticisms.

I gratefully appreciate the discussions and guidance of Professor Gerald Smith in the preparation of this work.

Finally, I am especially grateful for the enthusiasm and encouragement provided by Professor Donald Miller throughout my graduate career.

This work was done under the auspices of the U. S. Atomic Energy Commission.

APPENDICES

A. The Density Matrix Formalism

In the study of the production of strange-particle resonant states, there are many features of the data that one can examine in hopes of gaining insight about the mechanisms involved. Different theories highlight different aspects as being important, and the experimentalist is always faced with the task of presenting his data in a form that can easily be compared with theoretical predictions. Rather than adapting an *a priori* attitude that certain features of the data are "important" and concentrating only upon those aspects, we have selected a formalism that exhaustively presents all of the data obtainable from the experiment, and have cast theoretical predictions in that formalism whenever necessary.

The interaction of spinless particles can be characterized completely by a presentation of the differential cross section as a function of the c.m. energy or incident momentum. When we consider particles with nonzero spin, our characterization is modified only slightly. Again we specify the differential cross section, but for each set of possible spin states for the particles involved. Here resonant and strange particles are particularly useful. Not only can we directly measure the differential cross section, but by observing the decay of the short-lived final-state particles, we can infer information about their spin orientations, also.

The decay distribution from a pure state of low spin is relatively easy to obtain, but because of statistical limitations we group our data over a rather large range of production angle. In addition, the $\pi^- p$ initial state is mixture of proton spin-up and spin-down states. Rather than observing a pure final state, then, we see an incoherent mixture of states. Hence, the density matrix formalism, which straightforwardly handles incoherent sums of states when the algebra associated with each pure state is known, is useful to us. The general formalism of the density matrix is discussed in several places,[48-49] so I will present here only those formulae pertinent to our analysis.

For a set of n pure states, ψ_n is expressed in some basis as

$$\psi_n = \sum_m a_{nm} \phi_m . \tag{A1}$$

If we observe an incoherent mixture of these states each with a weight w_n, we have

$$|\psi|^2 = \sum_n \omega_n \; |\psi_n|^2 , \tag{A2}$$

and the density matrix is defined as

$$\rho_{m\ell} \equiv \sum_n a_{nm} \, a_{n\ell}^* \, \omega_n . \tag{A3}$$

If we are interested in some process which transforms our state ψ into another state, we can characterize the transition operator M as a matrix in the usual way by recording how it operates on the basis states ϕ_m, and transforming them into the new basis states Ψ_p.

$$M_{pm} \equiv \langle \Psi_p \, |M| \, \phi_m \rangle \tag{A4}$$

The density matrix for the initial incoherent set of states then transforms into a density matrix for the final states by

$$\rho_2 = M \rho_1 \, M^+ . \tag{A5}$$

For a particle spin density matrix, it is desirable to normalize our states in such a way that

$$\mathrm{Tr}\, \rho = 1. \tag{A6}$$

If we are interested in a two-body decay distribution, our final density matrix is also normalized to unity if we remember to integrate over the infinite set of spatial states as well as sum over the discrete spin states of the final particles.

$$\int \mathrm{Tr}\, \rho_2 \; d\Omega = 1 \tag{A7}$$

From this we see that the decay angular distribution is given by

$$I(\theta, \phi) = M \rho_1 M^+. \tag{A8}$$

For example, let us consider the decay of a particle with integer spin J into two spinless particles. Here ρ is a $(2J+1)\times(2J+1)$ matrix with indices referring to the magnetic quantum number running from J to -J. The pure state m gives rise to an angular distribution $Y_J^m(\theta, \phi)$, and M is a $1\times(2J+1)$ matrix $(Y_J^J, Y_J^{J-1} \ldots, Y_J^{-J})$. The decay distribution is then

$$I(\theta, \phi) = \sum_{mn} \rho_{mn} Y_J^{m*}(\theta, \phi) Y_J^n(\theta, \phi). \tag{A9}$$

In a strong interaction parity conservation relates the amplitudes for the production of particles in certain spin states to the amplitudes for other states. Since these amplitudes determine the state vectors for our final-state particles, the density matrix elements constructed from these state vectors are also related (in addition to the constraint that ρ be Harmitian). The form the state vectors take, and hence the form of the density matrix relations, depends upon what we take for our axis of quantization. Quantizing along the production normal leads to the checkerboard structure of the density matrix of Capps[50]. If instead we quantize along the beam direction, the relation becomes

$$\rho_{mn} = (-1)^{2j+m+n} \rho_{-m-n}. \tag{A10}$$

We see that we can write the most general form for the decay of an arbitrarily constructed collection of particles without reference to how the set was formed. We can, therefore, do no more experimentally than record values for density matrix elements that we observe. In a two-body final state containing particles with spin, our task is one of specifying the differential cross section and the density matrices of the final-state particles as a function of the production angle. (It is tacitly assumed here that we observe no further decays as we might in the production of a state such as the Ξ^*. Situations of this kind have been treated by Byers and Fenster[51], and by others[52].) If some theory

provides us with a set of production amplitudes for the various spin states, we can then apply the appropriate matrix to the density matrix for the initial proton-pion system and look at the predictions for the observed differential cross section and final-state density matrix elements. In our present experiment the proton targets are unpolarized and the initial density matrix takes the simple form

$$\rho_1 = \frac{1}{2}\begin{pmatrix} 1 & 0 \\ 0 & 1 \end{pmatrix} . \tag{A11}$$

For the process $\pi^- p \to Y K^*$, we have in the final state a spin-$\frac{1}{2}$ and a spin-1 particle. Quantizing along the beam direction yields the 6×6 matrix shown in Table XV, where the first and third indices refer to the fermion spin states and the second and fourth indices refer to the vector particle. Using θ and ϕ for the K^* rest frame and θ' and ϕ' for the baryon, we find for the most-general joint decay distribution

$$\begin{aligned} I(\theta,\phi,\theta',\phi') = \frac{3}{16\pi^2} \quad & (\rho_{++++} + \rho_{+-+-}) \sin^2\theta \\ & + (1-2(\rho_{++++} + \rho_{+-+-})) \cos^2\theta \\ & - \sqrt{2}\,\mathrm{Re}(\rho_{+++0} - \rho_{+0+-}) \sin 2\theta \cos\phi \\ & + \sqrt{2}\,\mathrm{Im}(\rho_{+++}) - \rho_{+0+-}) \sin 2\theta \sin\phi\, a \cos\theta' \\ & - 2\,\mathrm{Re}\,\rho_{+++-} \sin^2\theta \cos 2\phi \\ & + 2\mathrm{Im}\,\rho_{+++-} \sin^2\theta \sin 2\phi\, a \cos\theta' \\ & - 2\,\mathrm{Im}\,\rho_{++-+} \sin^2\theta a \sin\theta' \sin\phi' \\ & + \sqrt{2}\,\mathrm{Im}\,\rho_{++-0} \sin 2\theta a (\sin\phi' \cos\phi' + \cos\phi' \sin\phi) \sin\theta' \\ & + \sqrt{2}\,\mathrm{Im}\,\rho_{+0-+} \sin 2\theta a (\sin\phi' \cos\phi - \cos\phi' \sin\phi) \sin\theta' \\ & + \rho_{++--} \sin^2\theta\, a \sin\theta' (\sin\phi' \cos 2\phi + \cos\phi' \sin 2\phi) \\ & - 2\rho_{+0-0} \cos^2\theta\, a \sin\theta' \sin\phi' \\ & + \rho_{+--+} \sin^2\theta a \sin\theta' (\sin\phi' \cos 2\phi - \cos\phi' \sin 2\phi) \quad , \end{aligned} \tag{A12}$$

where a is the fermion decay asymmetry parameter.

Table XV. Density matrix for 1^- and $1/2^+$ particles.

Polarization states	Polarization states					
	++	+0	+-	-+	-0	--
++	ρ_{++++}	ρ_{+++0}	ρ_{+++-}	ρ_{++-+}	ρ_{++-0}	$i\rho_{++--}$
+0	ρ^*_{+++0}	$\frac{1}{2}-\rho_{++++}$ $-\rho_{+-+-}$	ρ_{+0+-}	ρ_{+0-+}	$i\rho_{+0-0}$	ρ^*_{++-0}
+-	ρ^*_{+++-}	ρ^*_{+0+-}	ρ_{+-+-}	$i\rho_{+--+}$	ρ^*_{+0-+}	$-\rho^*_{++-+}$
-+	ρ^*_{++-+}	ρ^*_{+0-+}	$-i\rho_{+--+}$	ρ_{+-+-}	$-\rho^*_{+0+-}$	ρ^*_{+++-}
-0	ρ^*_{++-0}	$-i\rho_{+0-0}$	ρ_{+0-+}	$-\rho_{+0+-}$	$\frac{1}{2}-\rho_{++++}$ $-\rho_{+-+-}$	$-\rho^*_{+++0}$
--	$-i\rho_{++--}$	ρ_{++-0}	$-\rho_{++-+}$	ρ_{+++-}	$-\rho_{+++0}$	ρ_{++++}

This distribution is characterized by 11 parameters that we can experimentally determine -- $\rho_{++++} + \rho_{+-+-}$, $\mathrm{Re}(\rho_{+++0} - \rho_{+0+-})$, $\mathrm{Im}(\rho_{+++0} - \rho_{+0+-})$, $\mathrm{Re}\,\rho_{+++-}$, $\mathrm{Im}\,\rho_{+++-}$, $\mathrm{Im}\,\rho_{++-+}$, $\mathrm{Im}\,\rho_{++-0}$, $\mathrm{Im}(\rho_{+0-+})$, ρ_{++--}, ρ_{+0-0}, ρ_{+--+}--which are related by a linear transformation to the 11 correlation coefficients of Berman and Oakes[53]. These 11 quantities are referred to as terms 1 through 11, respectifully, for convenience.

If we choose to ignore the information from the fermion decay and integrate over θ' and ϕ', we are left with three variables describing the decay of the K^*. These are the parameters used in the literature for the analysis of $K^- p \to K^* N$ --

$$\begin{aligned} \rho_{11} &= \rho_{++++} + \rho_{+-+-} && \text{(term 1)} \\ \rho_{1-1} &= 2\,\mathrm{Re}\,\rho_{+++-} && \text{(term 4)} \\ \mathrm{Re}\,\rho_{10} &= \mathrm{Re}(\rho_{+++0} - \rho_{+0+-}) && \text{(term 2)} \\ \rho_{00} &= 1 - 2\,\rho_{11}. \end{aligned} \tag{A13}$$

For electromagnetic Σ^0 decay, no polarization information can be obtained from observation of the isotropic γ-ray decay. It can be shown, however, that the subsequent Λ-decay average polarization is equal to -1/3 that of the Σ^0 [54], if we average over all Λ decay angles in the Σ^0 rest frame. We can use the formalism developed here, therefore, if we evaluate θ' and ϕ' from the proton decay of the Λ in the Λ rest frame and use a value of $\alpha = -0.22$. Here we must be careful to transform pertinent vectors from the center-of-mass to the sigma rest frame and then to the lambda rest frame to avoid complications from Stapp rotation effects.

For the reaction $\pi p \to Y^* K$, we consider only the states $Y^*(1520)$ and $Y^*(1385)$ and the initial strong decay of these states. For particles of spin 3/2, the decay distribution is given by

$$\begin{aligned} I(\theta,\phi) = \frac{3}{4\pi} \{ & \rho_{33} \sin^2\theta + (\tfrac{1}{2} - \rho_{33})(\tfrac{1}{3} + \cos^2\theta), \\ & - \frac{2}{\sqrt{3}} \mathrm{Re}\,\rho_{3-1} \sin^2\theta \cos 2\phi - \frac{2}{\sqrt{3}} \mathrm{Re}\,\rho_{31} \sin 2\theta \cos\phi \}, \end{aligned} \tag{A14}$$

where m and m' refer to twice the magnetic quantum numbers of Y^* states.

B. The Absorption Model

The predictions of one-particle-exchange models in describing the decay angular distributions in resonant production processes have been more or less successful. Experimental production angular distributions did not even closely follow theoretical calculations, however. The one-particle-exchange model allowed the presence of form factors, and by picking a form that guaranteed success, we were able to fit production angular distributions well. The character of these functions are such that the dependence of the differential cross section on production angle predicted by the unmodified model is completely masked, and analysis of distributions in no sense test the validity of the model.

The absorption model also was successful in predicting decay distributions while providing a description of the production angular distribution that agrees with experiment. In this case, however, the corrections to the one-particle exchange model have physical motivation rather than an ad hoc character. Whether any particular formulation of the absorption model currently in use survives, it seems plausible that the basic concepts are indeed responsible for the effects that we see.

In the traditional calculation of Feynman-diagram matrix elements, it is assumed that the incoming and outgoing particle states are represented by plane waves and that one particular diagram dominates the interaction. It is clear that this is not a valid assumption since a given reaction is just one of a number of competing inelastic processes that can occur. Jackson and others[31] suggested approximating the presence of these competing channels by calculating their effect on the incoming and outgoing waves in our basic one-particle-exchange diagram.

We can think of these other reactions as absorbing part of each angular momentum component of the plane waves and distorting the character of our initial and final states. We model the inelastic processes as a grey disk which preferentially absorbs low angular momentum states, then the process of interest will proceed through states of high angular momentum and produce the strong forward peaking that is

observed. If we model elastic scattering of the initial and final states as entirely the shadow of the inelastic processes, then we can parameterize the inelastic effects from a study of elastic-scattering characteristics.

The basic formula from which absorbing calculations proceed comes from a nonrelativistic approach to the problem. The validity of extending the formalism to processes at high energy is not certain, but the fact that it works is motivation enough to investigate its consequences. The basic statement is that the matrix element for a process between given initial and final spin states is shown by

$$M = S_f^{1/2} F S_j^{1/2} \quad , \tag{B1}$$

where $S_i(S_f)$ is the elastic-scattering matrix element for the initial (final) state, B is the "raw" Feynman diagram matrix element, and M is the final absorbed element. Jackson[31] has outlined the decomposition of B into angular momentum components, and the calculation of M. In this report we used instead Huff's formulation,[35] which casts the matrix elements in a linear momentum representation. This approach is computationally convenient since the usual calculation of B is in this representation. We need not decompose B into partial waves, perform the absorption calculation in each angular momentum state, and then convert back to the linear representation.

Properly stated, Eq. (B1) is

$$\begin{aligned} &\langle f\Omega\, \lambda_1\lambda_2 \,|M|\, i\,O\lambda_3\lambda_4\rangle \\ &= \sum_{\lambda_i'} \int d\Omega_f\, d\Omega_i \langle f\Omega\, \lambda_1\lambda_2 \,|S_f^{1/2}|\, f\Omega_f\, \lambda_1'\lambda_2'\rangle \langle f\Omega_f\, \lambda'_1\lambda_2' \,|B|\, i\Omega_i\, \lambda_3'\lambda_4'\rangle \\ &\quad \times \langle i\Omega_i\, \lambda'_3\lambda_4' \,|S_i^{1/2}|\, i\,O\,\lambda_3\lambda_4\rangle \, , \end{aligned} \tag{B2}$$

where i and f indicate the initial and final states, λ_i the helicity states of the particles involved, Ω the production angle of the final state, and $\lambda_i', \Omega_f, \Omega_i$ the helicities and angular distribution variables of the intermediate states that are to be summed and integrated over. Expressions are cast in a helicity representation because manipulative

formulae are particularly easy to express. By means of these formulae, expression (B2) is converted to

$$\langle f\theta\,\lambda_1\lambda_2\,|M|\,iO\,\lambda_3\lambda_4\rangle = \int d\Omega_f\, d\Omega_i \sum \langle f\theta\lambda_1\lambda_2\ \ |S_f^{1/2}|\,f\Omega_f\lambda_1\lambda_2\rangle$$

$$(-1)^{\mu-\mu'}\langle f\theta_i\,\lambda_1'\lambda_2'\,|B|_i\,O\,\lambda_3'\lambda_4'\rangle\, e^{i\phi_i(\mu'-\lambda')}\langle i\Omega_i\,\lambda_3'\lambda_4'\,|S^{1/2}|\,i\Omega_f\lambda_3\lambda_4\rangle, \tag{B3}$$

where

$$\lambda = \lambda_1 - \lambda_2$$
$$\mu = \lambda_3 - \lambda_4$$
$$\lambda' = \lambda_1' - \lambda_2'$$
$$\mu' = \lambda_3' - \lambda_4' \ .$$

Here we have the quantity $\langle f\theta_i\,\lambda_1'\lambda_2'\,|B|_i\,O\,\lambda_3'\lambda_4\rangle$, which is just the unmodified one-particle-exchange matrix element for scattering into an angle θ_i.

We now expand $S^{1/2}$ as $1 - T/2$ and keep terms at most linear in T. Since elastic scattering is largely confined to the forward direction, we restrict ourselves to no helicity changes for these processes. After some manipulation and trivial integration and summation, we obtain

$$\langle f\theta\lambda_1\lambda_2\,|M|\,iO\lambda_3\lambda_4\rangle = \langle f\theta\lambda_1\lambda_2\,|B|\,iO\,\lambda_3\lambda_4\rangle$$

$$- \int_{-1}^{+1} d\cos\theta' \int_0^{\pi} d\cos\phi'\,\langle f\,\theta'\lambda_1\lambda_2\,|B|\,iO\,\lambda_3\lambda_4\rangle \tag{B4}$$

$$\times\ \{\langle\theta'\lambda_3\lambda_4\,|T_i|\,O\lambda_3\lambda_4\rangle\,\mathrm{Re}[\eta^{2\mu}e^{-i\phi'(\mu-\lambda)}]$$

$$+\ \langle\theta'\lambda_1\lambda_2\,|T_f|\,O\lambda_1\lambda_2\rangle\,\mathrm{Re}[\eta^{2\lambda}e^{i\phi'(\mu-\lambda)}]\ \}$$

where $\eta = [\cos\theta'/2\,\cos\theta/2 + \sin\theta'/2\,\sin\theta/2\,e^{i\phi''}]\,/\cos(\theta''/2)$

$$\cos\theta'' = \cos\theta'\cos\theta + \sin\theta'\sin\theta\cos\phi' \ .$$

To compare with experiment we must now, of course, rotate the final amplitudes from the helicity directions to the coordinate systems

we have selected, and form the density matrix as outlined in Appendix A.

The matrix element T is related to the elastic-scattering cross-section distribution by

$$\frac{d\sigma}{d\Omega} = \frac{2\pi}{K} \; |T|^2. \tag{B5}$$

Experimentally elastic differential cross sections can be well approximated at least in the forward direction by the expression

$$\frac{d\sigma}{d\Omega} = \sigma^2_{total} \; e^{-A\Delta^2}, \tag{B6}$$

where Δ^2 is the negative of the four-momentum transfer. This gives us the magnitude of the matrix element T but not its phase. We are forced to assume that this phase is constant over all production angles and that it is the same for the initial and final states. If we arbitrarily set this phase to zero, then our matrix element will be all real and we will have no fermion polarization. Consequently terms three and five through eleven of the density matrix must of necessity be zero. We choose to let the value of this common phase be a free parameter to be determined by the fitting program. This, of course, is only an expediency to cover our ignorance of the situation and has no direct physical significance. Although the introduction of this parameter allows for non-zero values for all density matrix parameters, large deviations from zero cannot be fit by the theory. To achieve the extreme peripheral character of production distributions, the second term in Eq. (B4) must be mostly in phase with the first. The out-of-phase component adds to the differential cross section rather than subtracts from it.

From the observed width of decay of the K^*, we know the $K^*K\pi$ coupling constant but we have no information about the $pK\Lambda$ vertex. Information at both vertices for K^* exchange is lacking. Although we know the characteristics of elastic scattering over the range of energies considered here, the quantities characterizing the final-state interactions are completely unknown. Finally, we have no value for the phase parameter which we call χ. In the fitting program, chi-square was

minimized with six parameters allowed to vary σ_f, A_f, χ, g_p^2, g_v, and g_T. The last three coupling constants are defined in terms of the coupling constants presented in Ref. 55 by the relationships:

$$
\begin{aligned}
g_p &= g(Kp\Lambda) \\
g_v &= g(K^*K^*\pi)\, g_v(pK^*\Lambda) \qquad \text{(B7)} \\
g_T &= g(K^*K^*\pi)\, g_T(pK^*\Lambda) \,.
\end{aligned}
$$

REFERENCES

1. O. Goussu, et al., Nuovo Cimento 42, 606 (1966).
2. D. Colley, et al., Phys. Rev. 128, 1930 (1962).
3. G. Alexander, G. R. Kalbfleisch, D. H. Miller, and G. A. Smith, Phys. Rev. Letters 8, 447 (1962).
4. G. Smith, et al., Phys. Rev. Letters 10, 138 (1963).
5. D. H. Miller, A. Z. Kovacs, R. McIlwain, T. R. Palfrey, and G. W. Tautfest, Phys. Rev. 140, B360 (1965).
6. T. P. Wangler, A. R. Erwin, and W. D. Walker, Phys. Rev. 137, B414 (1965).
7. J. Bartsch, et al., Aachen, Hamburg, London, Munchen Collaboration, Strange Particle Production in $\pi^- p$ and $\pi^+ p$ Collisions at 4 GeV/c. Preprint.
8. L. Bertanza et al., Phys. Rev. 130, 786 (1962).
9. V. Belyakov et al., J. Nucl. Phys. (USSR) 1, 338 (1965).
10. V. Belyakov et al., J. Nucl. Phys. (USSR) 1, 351 (1965).
11. J. Murray et al., A Separated 2.5 - to 2.8 GeV/c K^- Beam at the Bevatron, UCRL-11426, July 1964. The beam was almost monochromatic, with $\Delta p/p \approx 0.015$.
12. A. Rosenfeld and W. Humphrey, Ann. Rev. Nucl. Sci. 13, 103 (1963).
13. Richard I. Hess, Analysis of $K\bar{K}$ Pairs from πp Interactions (Ph. D. Thesis), UCRL-16832, July 1966.
14. D. H. Miller, O. I. Dahl, L. M. Hardy, R. I. Hess, and J. Kirz, Strange Particle Production in $\pi^- p$ Interactions from 1.5 to 4.2 BeV/c, UCRL-16978 (to be submitted to Phys. Rev.).
15. G. Lynch, Program FAKE: MONTE CARLO Simulation of Bubble Chamber Events, UCRL-10335, July 1962.
16. A. N. Diddens, E. W. Jenkins, T. F. Kycia, and K. F. Riley, Phys. Rev. Letters 10, 262 (1963).
17. A. Citron, et al., Phys. Rev. Letters 13, 205 (1964). See also Phys. Rev. 144, B1101 (1966).

18. L. Jacobs, A Study of Resonance Production and Decay, and Elastic Scattering in $\pi^- p$ Two Prong Interactions, 205 - 3.22 GeV/c, (Ph. D. Thesis), UCRL-16877, August 1966.
19. S. U. Chung, Multi-Pion Final States from $\pi^- p$ Reactions at 3.2 and 4.2 GeV/c, (Thesis), UCRL-16881, July 1966.
20. J. Schwartz, Strange Particle Cross Sections in $\pi 72$, Alvarez Group Physics Note No. 526. This gives the cross sections found in the $\pi 72$ experiment.
21. J. Friedman (Lawrence Radiation Laboratory), private communication. (1966).
22. R. Dalitz and S. Tuan, Phys. Rev. Letters 2, 425 (1959).
23. R. D. Tripp, M. B. Watson, and M. Ferro-Luzzi, Phys. Rev. Letters 8, 175 (1962).
24. R. D. Tripp (Lawrence Radiation Laboratory), private communication (1966).
25. L. Stodolsky and J. Sakurai, Phys. Rev. Letters 11, 90, (1963).
26. L. Stodolsky, Phys. Rev. 134, B1099 (1964).
27. G. R. Lynch, et al., Phys. Letters 9, 359 (1964).
28. R. Barloutand, et al., Phys. Letters 12, 352 (1964).
29. J. Friedman and R. Ross, Phys. Rev. Letters 16, 485 (1966).
30. See for example J. D. Jackson, Rev. Mod. Phys. 37, 484 (1965).
31. K. Gottfreid and J. D. Jackson, Nuovo Cimento 34, 735 (1964).
32. J. D. Jackson, J. T. Donahue, K. Gottfreid, R. Keyser, and B. Ey. Svensson, Phys. Rev. 139, B428 (1965).
33. S. M. Flatté, $K^- p \rightarrow \Lambda\omega$ from 1.2 to 2.7 BeV/c: The Absorption Model with Strange Meson Exchange (Ph. D. Thesis), UCRL-16648, March 1966.
34. R. Huff (Department of Physics, University of California at Los Angeles), private communication (1966).
35. J. B. Bronzan and F. E. Low, Phys. Rev. Letters 12, 522 (1964).
36. N. Hague, et al., Phys. Letters 14, 338 (1965).
37. S. Focardi et al, Phys. Letters 16, 351 (1965).
38. L. Hardy, et al., Phys. Rev. Letters 14, 401 (1965).

39. S. U. Chung, et al., Phys. Rev. Letters 15, 325 (1965).
40. M. Month, Phys. Letters 18, 357 (1965).
41. T. P. Wangler, A. R. Erwin, and W. D. Walker, Phys. Letters 9, 71 (1964).
42. D. H. Miller, et al., Phys. Letters 15, 74 (1965).
43. R. Bock, et al., Phys. Letters 12, 65 (1964).
44. S. P. Almeida, et al., Phys. Letters 16, 184 (1965).
45. B. C. Shen et al., Bull. Am. Phys. Society 11, 77 (1966).
46. M. Derrick et al., Bull. Am. Phys. Soc. 11, 76 (1966).
47. See, for example, A. H. Rosenfeld, Mesons, UCRL-16462, Proceedings of Oxford International Conference on High Energy Physics, Oxford, England, 1965 (to be published).
48. W. S. C. Williams, Introduction to Elementary Particles, (Academic Press, New York, 1961). pp. 172-175.
49. V. Fano, Rev. Mod. Phys. 89, 74 (1957).
50. R. H. Capps, Phys. Rev. 122, 929 (1961).
51. N. Byers and S. Fenster, Phys. Rev. Letters 11, 52 (1963).
52. C. Zemach, Phys. Rev. 140, B109 (1965); S. U. Chung, Phys. Rev. 138, B1941 (1965); M. Ademillo and R. Gatto, Phys. Rev. 140, B192 (1965).
53. S. M. Berman and R. J. Oakes, Phys. Rev. B1034 (1964).
54. N. Byers and H. Burkhardt, Phys. Rev. 121, 281 (1961).
55. J. D. Jackson and H. Pilkuin, Nuovo Cimento 33, 906 (1964).

This report was prepared as an account of Government sponsored work. Neither the United States, nor the Commission, nor any person acting on behalf of the Commission:

A. Makes any warranty or representation, expressed or implied, with respect to the accuracy, completeness, or usefulness of the information contained in this report, or that the use of any information, apparatus, method, or process disclosed in this report may not infringe privately owned rights; or

B. Assumes any liabilities with respect to the use of, or for damages resulting from the use of any information, apparatus, method, or process disclosed in this report.

As used in the above, "person acting on behalf of the Commission" includes any employee or contractor of the Commission, or employee of such contractor, to the extent that such employee or contractor of the Commission, or employee of such contractor prepares, disseminates, or provides access to, any information pursuant to his employment or contract with the Commission, or his employment with such contractor.